M 2021

U.PORTO
FEUP FACULDADE DE ENGENHARIA
UNIVERSIDADE DO PORTO

MODELLING OF A VACUUM PRESSURE SWING ADSORPTION UNIT FOR KINETICALLY CONTROLLED SEPARATION OF METHANE AND NITROGEN

ALEXANDRA SOFIA RAMOS DA SILVA
DISSERTAÇÃO DE MESTRADO APRESENTADA
À FACULDADE DE ENGENHARIA DA UNIVERSIDADE DO PORTO EM
CHEMICAL ENGINEERING

Master in Chemical Engineering

Modelling of a Vacuum Pressure Swing Adsorption unit for kinetically controlled separation of methane and nitrogen

Master dissertation

of

Alexandra Sofia Ramos da Silva

Developed within the course of dissertation

held in

DMT Environmental Technology

Supervisor at FEUP: **Prof. Alexandre Ferreira**

Coordinator at DMT-ET: **Eng. Jort Langerak**

U.PORTO
FEUP FACULDADE DE ENGENHARIA
UNIVERSIDADE DO PORTO

DEPARTAMENTO DE
ENGENHARIA QUÍMICA

July 2021

Acknowledgment

The process of doing this Master Thesis in a foreign country, and during a pandemic period, allowed me to live an intensive and enriching experience, both personally and professionally. Although this is an individual work, I relied on the support and expertise of people around me throughout this project's development:

First, I would like to thank DMT's Research and Development team, for the warm welcoming in the company and in The Netherlands. Also, for the constant availability and guidance.

To my academic supervisor at FEUP, Professor Alexandre Ferreira, for all the assistance provided and for the encouraging words.

For the girls that shared these 5 months with me 24/7, Carina, Francisca, Mariana, Melanie and Tânia, thank you for making this a lot easier, funnier and for keeping up with me.

To my Mom and Dad, that always supported my decisions and gave me total independence, without ever letting me down. To Pedro, for being a cheerful brother.

And finally, to my best friend and life companion Xico, for always believing in me, for his wise and optimistic advice and for being my shelter.

Abstract

A model of a single-bed for separating a 100 m^3 h^{-1} biogas stream composed of 90 % methane and 10 % nitrogen was developed in *Aspen Adsorption*. The separation simulation studied a 2-bed 5-step Vacuum Pressure Swing Adsorption unit, with feed pressurization, adsorption, co-current blowdown, countercurrent blowdown, and low-pressure purge. The system's operating pressures swung from 5 bar to 0.1 bar for regeneration purposes, and the column dimensions considered were standardized of 2 m height and 70 cm diameter.

The kinetic controlled separation with nitrogen selectivity was possible due to the structural characteristics of the chosen adsorbents, Purified Clinoptilolite, and the cation exchanged Mg-Clinoptilolite. Even though these materials present higher capacity for methane in equilibrium, i.e., are thermodynamically selective to this component, there is a considerable difference between nitrogen and methane diffusivity constants, caused by the cation arrangement on these adsorbent materials. Mass transfer resistance, mostly felt by the larger molecule in the gas mixture (methane), lead to an overall kinetic selectivity favorable to nitrogen retention in the adsorbent, hence, obtaining a high-pressure stream of the desired product at the top of the column. All these characteristics were supported by the breakthrough curve behavior, simulated for both pure component and binary mixture of methane and nitrogen.

A sensitivity study was performed with the purpose of process optimization based on the PSA performance indicators – product purity and recovery. The evaluated process parameters were the purge to feed ratio (P/F_{in}), adsorption pressure, final pressure in the co-current blowdown step, low pressure of the countercurrent blowdown, and column's height to diameter ratio (L/D) for a fixed volume. Furthermore, the cycle and steps time were also a matter of evaluation.

Cyclic steady state results obtained for both adsorbents attained the product purity target for gas grid injection of high-quality gas (≥ 97 %). Simulations for Purified Clinoptilolite reached a product purity of 97 % and 66 % recovery, whereas Mg-Clinoptilolite presented the most promising values of 98 % methane purity and product recovery of 78 %. Additionally, process productivity and energy consumption during regeneration steps for one cycle were also considered. Purified Clinoptilolite productivity was 3.37 mol_{CH4} kg_{ads}^{-1} h^{-1}, with a regeneration energy requirement of 57.36 kJ mol_{CH4}^{-1}. For Mg-Clinoptilolite, the obtained productivity was 3.78 mol_{CH4} kg_{ads}^{-1} $h^{-1,}$ and the necessary energy was 41.95 kJ mol_{CH4}^{-1}.

Keywords: Biogas upgrading; Pressure Swing Adsorption; Kinetic selectivity; Clinoptilolite; Aspen Adsorption

Resumo

Neste trabalho, foi desenvolvido um modelo para uma coluna de adsorção, no programa *Aspen Adsorption,* com o intuito de separar uma corrente de biogás composta por 90 % metano e 10 % azoto. A simulação da separação baseou-se numa unidade de Adsorção com Modulação de Pressão e Vácuo, de 2 colunas e 5 etapas, sendo elas pressurização com a corrente de alimentação, adsorção, regeneração co-currente, regeneração contra-corrente e purga a pressão baixa. As pressões de operação consideradas foi de 5 bar como pressão alta, e 0,1 bar como pressão baixa, sendo a coluna dimensionada conforme as medidas normalizadas de 2 m de altura e 70 cm de diâmetro. A separação controlada pela cinética e seletiva ao azoto foi possível devido às características estruturais dos adsorbentes selecionados para este estudo – Purified Clinoptilolite e Mg-Clinoptilolite. Apesar destes materiais apresentarem seletividade ao metano em equilíbrio, as diferenças difusionais entre as moléculas de azoto e de metano dominaram no cálculo da seletividade geral. Assim, foi possível simular o caso preferencial em que o produto desejado é recolhido a alta pressão no topo da coluna. A maior resistência à transferência de massa do metano foi comprovada pela análise da curva de rutura dos componentes puros e da mistura gasosa binária de metano e azoto. Foi realizado o estudo de sensibilidade de alguns dos parâmetros mais importantes do processo, com o objetivo de otimizar o processo em termos de pureza e recuperação de metano. Os parâmetros incluídos na análise de sensibilidade foram a razão entre o caudal de purga e o caudal de alimentação (P/F_{in}), pressão alta de adsorção, pressão final na etapa de regeneração em co corrente, pressão final na etapa de regeneração em contra corrente, e a razão entre a altura e diâmetro (L/D) mantendo o volume fixo. Para além destes parâmetros, também o tempo de ciclo e tempo de etapas foram avaliados. Os resultados obtidos em estado estacionário cíclico, atingiram o objetivo de um produto com pureza acima dos 97 %, sendo que esta composição permite a injetação desta corrente de biometano nas redes de gás. Para o material Purified Clinoptilolite, foi obtida uma pureza de 97% com recuperação de 66%, enquanto que para o adsorbente Mg-Clinoptilolite, melhores resultados foram atingidos, com 98% de pureza e 78 % de recuperação. Outros indicadores de desempenho do sistema foram analisados, como a produtividade e o consumo de energia nas etapas de regeneração de um ciclo. Estes valores foram, respetivamente, 3.37 mol_{CH4} kg_{ads}^{-1} h^{-1} e 57.36 kJ mol_{CH4}^{-1} para Purified Clinoptilolite e de 3.78 mol_{CH4} kg_{ads}^{-1} h^{-1} e 41.95 kJ mol_{CH4}^{-1} para Mg-Clinoptilolite.

Declaration

I hereby declare, under word of honour, that this work is original and that all non-original contributions is indicated and due reference is given to the author and source

Alexandra Sofia Ramos da Silva

05/07/2021

Index

List of Figures

List of Tables

Notation and Glossary

P	pressure	bar
F	molar flowrate	mol s^{-1}
L	column length/ height	m
D	column diameter	m
q	adsorption capacity	mol kg_{ads}^{-1}
b_0	Langmuir's affinity constant	bar^{-1}
R	gas constant	J mol^{-1} K^{-1}
T	temperature	K
ΔH	enthalpy	J mol^{-1}
D_c	diffusion time constant	m^2 s^{-1}
r_p	particle radius	m
D_0	diffusivity at zero adsorbate concentration	m^2 s^{-1}
E_A	activation energy	J mol^{-1}
p	partial pressure	bar
u	superficial velocity	m s^{-1}
u_i	interstitial velocity	m s^{-1}
U_{mf}	minimum fluidization velocity	m s^{-1}
D_{ax}	axial dispersion coefficient	m^2 s^{-1}
k_L	mass transfer coefficient	s^{-1}
k_g	gas thermal conductivity	W m^{-1} K^{-1}
k_s	solid thermal conductivity	W m^{-1} K^{-1}
C_{vg}	gas heat capacity	J kg^{-1} K^{-1}
C_{ps}	the solid heat capacity	J kg^{-1} K^{-1}
h_w	heat transfer coefficient	W m^{-2} K^{-1}
r_b	bed radius	m
T_g	gas temperature	K
T_s	solid temperature	K
T_W	column wall temperature	K
S	adsorbent separation factor	
K	kinetic selectivity	
y	molar fraction	
c_g	gas phase concentration	mol m^{-3}

Greek Letter

ε	porosity	
ε_p	intra-particle porosity	
ε_b	bed porosity	
ε_i	inter-particle porosity	
ρ_p	particle density	kg_p m_p^{-3}
ρ_f	density of the fluid	kg m^{-3}
ρ_g	gas density	kg m^{-3}
ρ_b	bed density	
μ_f	viscosity of the fluid	N s m^{-2}
ψ	sphericity of the particle	
α_{ideal}	ideal selectivity	
α_{eq}	equilibrium selectivity	
β	overall kinetic selectivity	

Indexes

i	component
in	inlet condition
out	outlet condition
sat	saturation
ads	adsorbent
p	particle
*	equilibrium
g	gas
w	wall
b	bed
s	solid
0	initilal

List of Acronyms

VPSA	Vacuum Pressure Swing Adsorption	
PSA	Pressure Swing Adsorption	
GHG	Green House Gas	
RNG	Renewable Natural Gas	
LCV	Lower Calorific Value	$J\ m^{-3}$
TSA	Temperature Swing Adsorption	
CMS	Carbon Molecular Sieves	
MOF	Metal-Organic Framework	
RMSD	Root Mean Square Deviation	
VSA	Vacuum Swing Adsorption	
VOC	Volatile Organic Compound	

1 Introduction

1.1 Framing and presentation of the work

The increasing restrictions regarding greenhouse gas (GHG) emissions and environmental awareness motivate several countries to adopt different strategies in the energy sector.

From 1971 to 2018, the global energy supply increased 2.6 times, according to the International Energy Agency. This led to a change in the energy sources structure, noticing a higher variation for nuclear and natural gas, with this latter growing from 16 % to 23 % of the total share. [1] The European commitment to reach an economy with net-zero greenhouse gas emissions by 2050 is an incentive to develop technologies of renewable sources of energy, such as biogas. Due to the high methane content in biogas, this can be used as a green energy source without adding to the global emission of CO_2. [2]

The process of biogas upgrading aims to produce biomethane that is indistinguishable from natural gas, which is a growing energy source. Typical pipeline specifications for high-quality natural gas injection in the grid is a stream with 2 % CO_2 and ≤ 3 % N_2 (more information in Annex A). The presence of both these components in biogas decreases its calorific value and can be corrosive to the pipeline, so their removal is essential to enhance the energy content of this renewable source. [3] By improving methane concentration in the biogas stream up to 97 % or more, this stream can be injected into the gas grid without harmful consequences, serving as a fair substitute for non-renewable natural gas.

This work is focused on removing nitrogen from a decarbonated methane stream, composed of 90 % methane and 10 % nitrogen with a 5-step Vacuum Pressure Swing Adsorption process, to inject the produced renewable natural gas in the gas grid. The modelling of a VPSA unit is developed based on a single bed approach. The scheme of the project where this separation technology will be implemented is depicted in Figure 1.

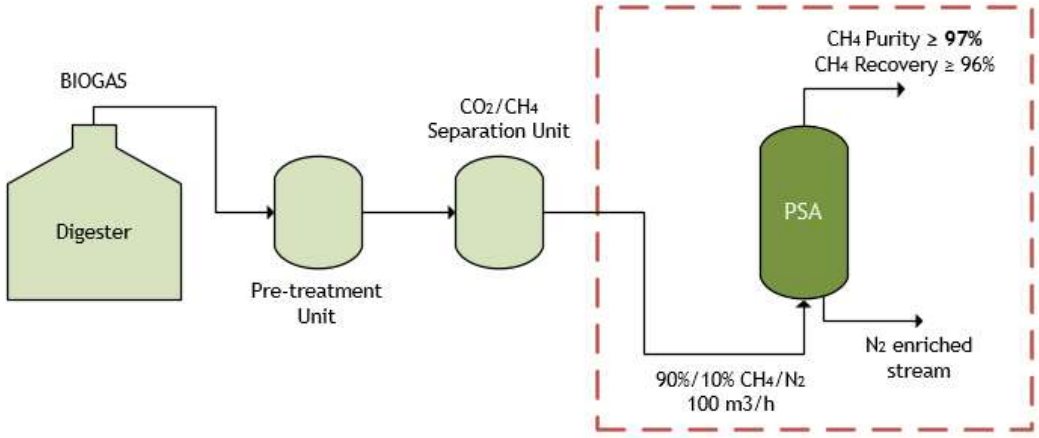

Figure 1 - Scope of the work.

1.2 Presentation of the company

DMT Environmental Technology is a Dutch company specializing in assisting other companies to contribute to the environment sustainably and profitably. The techniques developed and implemented are related to biogas upgrading and can solve environmental issues.

1.3 Contribution of the author to the work

The adsorbents' cell characterization, isotherm measurements and diffusion uptake experiments were extracted from literature. This data was essential for me to calculate the isotherm's parameters required by the programme *Aspen Adsorption*. All the breakthrough curves, sensitivity analysis and PSA configuration results shown in this work were obtained from the different simulations designed.

1.4 Organization of the dissertation

This work is organized into six main chapters. Chapter 1 describes the framework, the project presentation, as well as its main objectives. Chapter 2, Context and State of the art, presents the main challenges of the separation process of methane and nitrogen for biogas upgrading, with adsorption concepts and Pressure Swing Adsorption description, and a screening of the most widely used adsorbents in the industry. The third chapter defines the methodology applied to obtain the results, such as component isotherms and diffusivity constants, with detailed descriptions of the adsorption bed configuration and thermodynamic models and equations. Chapter 4 describes the obtained results during the process of PSA optimization. In Chapter 5, the main conclusions of this work were addressed. Finally, Chapter 6 provides a final review of the work done and improvement recommendations for future work on this topic.

2 Context and State of the art

2.1 Biogas upgrading - CH_4/N_2 separation challenges

Biogas is a valuable renewable energy produced from biodegradable organic materials by anaerobic digestion. The main constituents of biogas are methane (CH_4), known as Renewable Natural Gas (RNG), and carbon dioxide (CO_2), with various quantities of contaminants, such as nitrogen (N_2), ammonia (NH_3), water vapor (H_2O), hydrogen sulfide (H_2S), methyl siloxanes, oxygen (O_2), halogenated volatile organic compounds (VOCs), carbon monoxide (CO) and hydrocarbons. These contaminants presence and quantities depend mainly on the pH of the reactor, as well as the biogas source, which could be many substrates, sewage sludge, manure, bio-waste, or landfill decompositions (biogas composition specification in Annex B). [4]

The most valuable component of biogas is methane. Its treatment for RNG consists of a cleaning step for removing trace contaminants harmful to the natural gas grid, equipment, or final user applications. This process is known as biogas upgrading. [5] Apart from CH_4, all the other gases in biogas are undesirable and are considered biogas pollutants. The energy content of methane is described by a Lower Calorific Value (LCV) of 36 MJ/m^3 (at STP conditions). Therefore, it is well understood that the higher the CO_2 or N_2 content is, the lower the LCV in biogas. [6] Figure 2 describes the procedure that follows the biogas upgrading. [7]

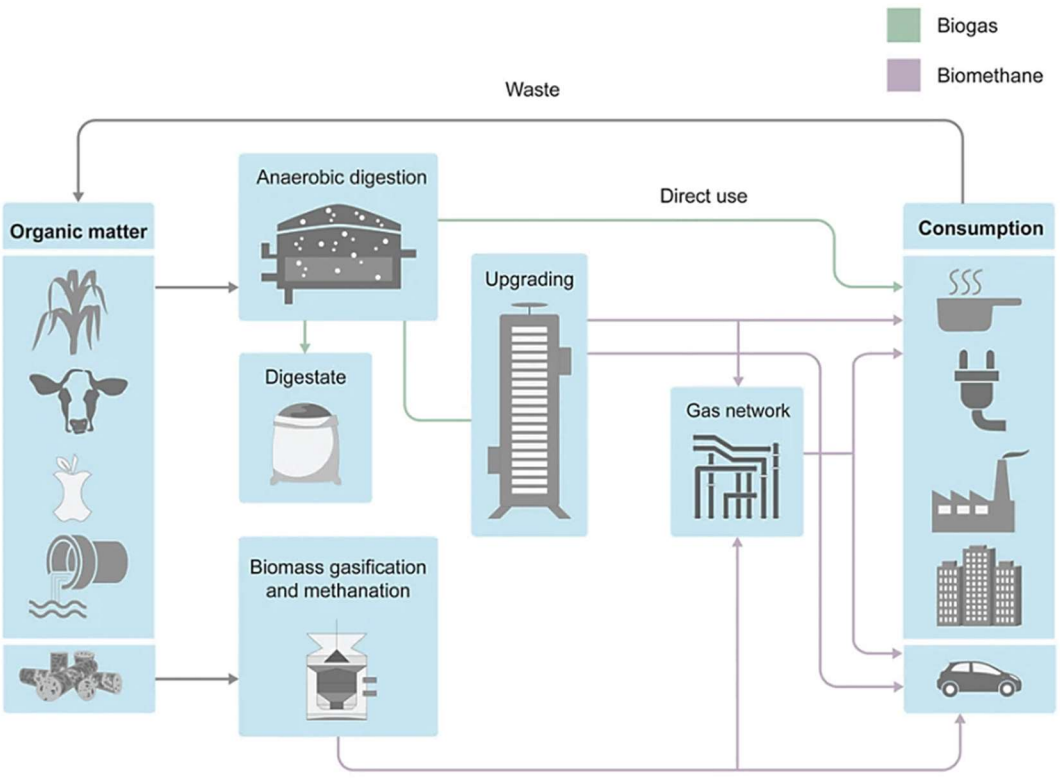

Figure 2 - Biogas upgrading and utilization. [7]

There are already several well-established separation processes to remove carbon dioxide, the second most predominant component, from the biogas stream. Technology such as acid absorption of CO_2 has been proven, and it can achieve high separation power for CO_2 removal. [3] At DMT, the used procedure for this separation is either by their mature membrane technology or by Pressure Swing Adsorption, which is still under development.

After the CO_2 removal on the biogas upgrading process, N_2 content must be reduced to the grid specifications (≤ 3 % N_2). N_2 rejection from a CH_4-rich mixture is a challenging separation, and the existing technologies used to produce methane with a residual less than 3 % nitrogen are cryogenic distillation and separation by adsorption. [5] A brief comparison between other conventional technologies used for the biogas upgrading to biomethane is depicted in Appendix A.

Nonetheless, the similar properties of methane and nitrogen turn this process a difficult procedure. Indeed, gas separation rely on differences in molecular or thermodynamic parameters of the mixture components, such as differences in the kinetic diameter, polarizability, transport properties, boiling points, diffusivity, solubility, or adsorption capacity. [3]

Cryogenic distillation exploits the different volatilities of the mixture, and it is widely used to separate N_2 from natural gas because it can achieve a high-purity CH_4 product (99.9 %). However, cryogenic processes are highly energy-intensive and require a large amount of energy and equipment. These plants must process a relatively high volume of gas before they are economical, typically in the range of 100−500 million standard cubic feet per day (MMSCFD). [8]

At modest-scale biogas resources, adsorption is an economical and efficient solution to remove N_2 from CH_4. [9] Adsorption processes depend on a material selectivity towards a component of the mixture, exploiting the differences of diffusion and/or adsorption capacity, which are inherent properties of the adsorbent material.

In Pressure Swing Adsorption (PSA) processes, the component with the lowest composition in the mixture should get retained in the solid surface of the adsorbent, to obtain CH_4 as the high-pressure raffinate product. This is beneficial since it reduces the work needed to pressurize CH_4 back to pipeline pressure. [10] Yet, most of the commercially available adsorbents traditionally used in PSA are thermodynamically selective to methane. [8] Furthermore, the similar characteristics between these two components make it challenging to find highly selective adsorbents, which compromises the efficient separation (see Annex C).

2.2 Adsorption concepts

Adsorption is the name given to the exothermic phenomenon of a fluid phase molecule retained in a solid surface, designed adsorbent. [11] This interaction frequently differs between gas molecules, inducing the separation of components in a gas mixture. It involves the diffusion of a component from the bulk fluid into the pores of a solid particle and the binding of that component to the solid surface inside the pores. The driving force for the migration of the chemical species into the pore phase is the concentration difference. [12]

Gas separation can be achieved either by a thermodynamically/equilibrium or kinetically controlled adsorption process. A thermodynamically controlled separation is performed by the preferential adsorption capacity of one of the components over the other. Conversely, in a kinetically controlled one, the difference in diffusion rates between the components is the leading cause of the separation, directly related to the mass transfer resistances present in the macro or micropores.

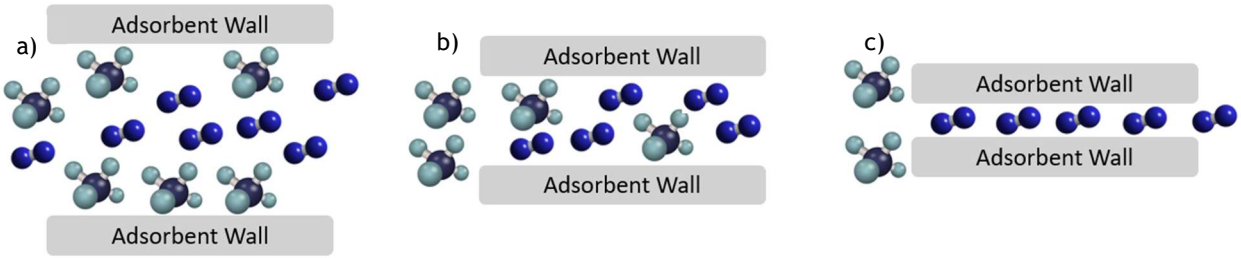

Figure 3 - Different types of separation mechanisms: a) equilibrium-based separation; b) kinetically controlled separation; c) molecular sieving effect.

The limiting case of a kinetically controlled separation is known as the molecular sieving effect, which works with the difference in kinetic sizes of the gas mixture, allowing the smaller molecules pass through the solid material's pore opening. This method needs an extremely controlled narrow pore size, so it can be adjusted for the gas components to be separated. For the case of nitrogen and methane mixture, the pore size would ideally be between the two kinetic diameters of these molecules: 3.64 Å (nitrogen) and 3.80 Å (methane). [3] Additionally, this separation based on the steric factors can only be possible for adsorbents presenting an uniform pore size distribution, such as zeolites or metal-organic frameworks. [13]

Another essential concept is the isosteric heat of adsorption which characterizes the strength of interactions between adsorbate molecules and adsorbent surface. The higher heat of adsorption, the stronger is the interaction between the component and the solid, which also indicates a more difficult regeneration process. [14]

2.3 Pressure Swing Adsorption

The performance of separation by Pressure Swing Adsorption is dependent on both adsorbent material and the cyclic process configuration.

Adsorptive separation processes can be categorized by the regeneration method, feed composition, and separation mechanism.

The adsorbent regeneration method can be performed based on temperature or pressure manipulation. In Temperature Swing Adsorption (TSA) cycles, the adsorbent is primarily regenerated by heating, whereas in the pressure swing adsorption (PSA) process, the regeneration is done by lowering the pressure. [15] PSA is, overall, more common than TSA. The significant reason for this difference is that the pressure swing can be accomplished much more quickly than the temperature swing. [12]

Based on the concentration of the strongly adsorbed component in the mixture, the separation process can be defined as bulk separation or purification. For feed mixtures where the adsorbed component is 10 wt % or more, the process is characterized as bulk separation. Purification is defined as when less than 10 wt % of the most adsorbed component is in the feed. [14,15]

PSA was first developed by Khale in 1942, Germany, and later it was patented by Skarstrom, in 1958, USA. [17] Due to the recent technology improvements and better adsorbents materials, this process has been intensively studied to serve as an industrial alternative for cryogenic distillation for gas separation purposes. PSA enables the achievement of high purity values and moderated energy consumption as it is mainly applied in small facilities, which is advantageous when compared to the intensive cost and energy required process of cryogenic distillation. [16]

In the natural gas industry, adsorption-based separations are already used to remove water, sulfur, mercury, and heavy hydrocarbons from the natural gas stream. [3] PSA technology has achieved wide acceptance for hydrogen purification, air drying, and small to medium-scale air separation applications. Other industrial applications of PSA processes are separating linear paraffins from branched hydrocarbons, solvent recovery, monomers recovery, and removing pollutants such as SO_2 and H_2S from industrial gases. [18]

The basic PSA configuration is represented by the *Skarstrom* cycle, in which a two-column arrangement follows the four steps sequence – pressurization, production/adsorption, depressurization or regeneration, and purge, as explained by the sequence in Figure 4. [12]

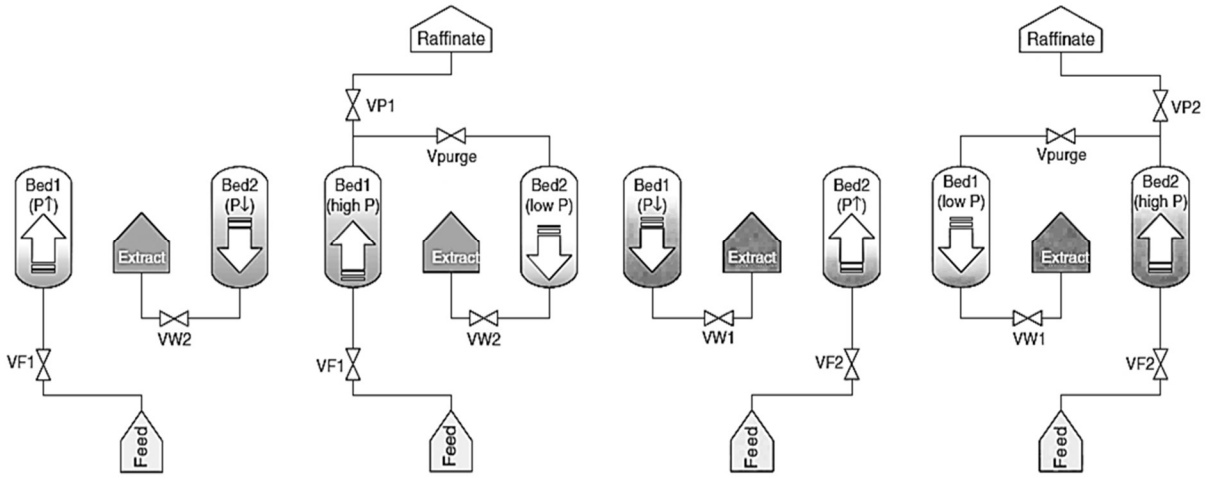

Figure 4 - PSA Skarstrom 4-step cycle configuration for 2-bed arrangement. [11]

A typical PSA process is a cyclic process where a number of connected vessels containing adsorbent/adsorbents undergo successive pressurization and depressurization steps in order to produce a continuous stream of purified product. Analyzing the overall process for one bed, the procedure can be defined as follows: [15,17]

1) Bed 1 is pressurized until the operating pressure is achieved. At the same time, bed 2 is in counter-current blowdown to low operating pressure. This pressurization can be performed with an inert gas (for example helium) or with the mixture feed.

2) When operating pressure is reached, high pressure feed flows through bed 1, where a strongly adsorbed (or faster diffusing) component is retained, designed heavy component. A product stream enriched with the less strongly adsorbed component, light component, is collected as a high-pressure raffinate product. This step is interrupted right before the breakthrough of the heavy component, to prevent it from reaching the top of the column.

3) The column is then regenerated in counter-current by pressure decreasing. The outlet gas is enriched with the most adsorbed component in the adsorbent, designed heavy product.

4) As both columns of the PSA system operate by a 180º difference, the product of one of the beds is used to perform the purging of the other.

The growth of gas separation by PSA results from a series of significant scientific and engineering developments initiated by the invention of synthetic zeolites and the pressure swing adsorption cycles. These inventions were followed by a succession of technological and theoretical advances. Among them are the developments of more efficient PSA cycles, new and improved adsorbents, adsorption theory, models for multicomponent adsorber dynamics, and computer-assisted modeling. [15]

2.3.1 Optimization of PSA arrangement

An optimization of PSA is directly connected to the enhancement of product purity, product recovery and the productivity of the process. This can be achieved with modifications of the basic *Skarstrom* cycle.

There are six basic cycle steps associated with any PSA process; these are the feed/adsorption, rinse (or heavy reflux), co-current or counter-current depressurization, purge (or light reflux), pressure equalization, and pressurization steps. However, since a typical PSA process has multiple beds operating simultaneously and every bed following the same set of cycle steps in order, these six different cycle steps can be scheduled in many ways. This gives rise to a multitude of varying cycle configurations, including cycles that have beds interacting with each other. [19]

The introduction of a co-current blowdown step preceding the counter-current blowdown in the *Skarstrom* cycle was the first modification applied to the system. This results in an enhancement of extract product purity as well as an increase of raffinate product recovery. [18]

Another cycle proposal was adding desorption in sub-atmospheric pressures, which increases both purity and recovery of the raffinate product. The loss of a slower diffusing component, in this case, is less than the traditional *Skarstrom* cycle, though the energy cost for this cycle is higher. Whenever the regeneration process occurs under this low-pressure condition, the procedure can be designed as Vacuum Pressure Swing Adsorption (VPSA), if adsorption pressure is higher than 1 bar, or Vacuum Swing Adsorption (VSA), when the working capacity is in the sub-atmospheric pressure range.

Energy conservation and product recovery can also be improved with a pressure equalization step, where the two beds are connected through their product ends to equalize pressure between the end of high-pressure adsorption step of bed 1 and the low-pressure desorption step of bed 2. [18]

There are innumerous ways of PSA arrangements. Therefore, the cycle configuration may variate based on the specific separation characteristics and operating conditions. Several reported PSA designs for the N_2-CH_4 case can be consulted in Appendix B.

2.4 Adsorbent assessment

The success or failure of the adsorption process depends on how the solid performs in both equilibria and kinetics. In the process of choosing the ideal adsorbent, there are some crucial parameters to have in consideration, such as ideal (α_{ideal}) and equilibrium selectivity (α_{eq}), adsorbent separation factor (*S*), as well as pure (*K*) and overall kinetic selectivity (β). [20]

Ideal selectivity - based upon the adsorption isotherm of the pure gas, for a certain temperature and pressure, where q_i stands for the adsorbed phase concentration of component i, and y_i is the component molar fraction.

$$\alpha_{ideal} = \frac{q_i/y_i}{q_j/y_j} \tag{2.1}$$

Equilibrium selectivity - calculated from the ratio of Henry's constants of each gas, designed by H_i and H_j

$$\alpha_{eq} = \frac{H_i}{H_j} \tag{2.2}$$

Adsorbent separation factor - one of the most important parameters to analyze for PSA purposes and equilibrium driven separations, since it embraces the working capacity for the operating pressure range.

$$S = \alpha_{eq} \frac{\Delta q_i}{\Delta q_j} \tag{2.3}$$

Pure kinetic selectivity - the diffusion of gases through the adsorbent wall is compared through this kinetic parameter, where D_{c_i} is the component *i* diffusivity constant.

$$K = \frac{D_{c_i}}{D_{c_j}} \tag{2.4}$$

Overall kinetic selectivity - for kinetically driven separations, this is the most crucial parameter to evaluate the potential separation performance, where both equilibrium and kinetic selectivity are taken into consideration.

$$\beta = \alpha_{eq}\sqrt{K} \tag{2.5}$$

Additionally, the commercial availability of the material is also an essential factor for the adsorbent selection. Overall, the requirements of a good adsorber are a combination of high capacity, high selectivity, and good durability**.** Another important adsorbent characteristic is a good interaction of the gas with the material, associated with its regeneration ability and heat of adsorption, for the implementation in a pressure swing process.

For the specific case of nitrogen and methane separation, the most used porous adsorbents in the industry are carbon-based materials, natural or synthetic zeolites, titanosilicates, and metal-organic frameworks. [8] A brief assessment of the published works for the most promising materials for these two-component separation is further presented. A screening and comparison of all adsorbents considered can be consulted in Appendix C.

2.4.1 Carbon-based materials

Carbon-based materials, such as Carbon Molecular Sieves (CMS) and Activated Carbon, present a higher surface area, lower cost, higher thermal stability, and broader availability among the usually utilized adsorbents. Due to their higher surface area, they show the greatest adsorption capacity for both nitrogen and methane compared to other adsorbent materials since their pore size distribution provides good access of sorbate molecules to the interior. [20]

a) Carbon Molecular Sieves (CMS)

CMS is a microporous material widely used in the separation of C_1 - C_5 hydrocarbons, inorganic gases, nitrogen-oxygen, formaldehyde, and H_2S. Because of the small pore size and high surface area, it has been studied in the adsorption of CH_4 and N_2. [8] This adsorbent material is equilibrium selective to methane since pure component isotherm shows higher adsorption capacity for methane than for nitrogen. [21]

However, for both gases, a surface barrier resistance at the mouth of the micropores and the micropore mass transfer resistance share the control of the diffusion process: in a study from Cavenati et al. (2005), at 308 K, a pure kinetic selectivity for nitrogen of 214.16 was obtained, since methane uptake showed a much slower diffusion. Although the overall kinetic factor was affected by the material equilibrium selectivity to methane, the sizeable kinetic ratio between both gases was dominant, resulting in an overall kinetic selectivity of 6.40. This value indicates a significant difference in adsorption kinetics appropriate to adsorb nitrogen and reject methane.

In a more recent work, Effendy et al. (2017) numerically studied the CMS 3K-172 potential to separate methane from nitrogen by a kinetically controlled process. A combined overall kinetic selectivity towards nitrogen with an optimized 9-step vacuum PSA exhibited a product of CH_4 under pipeline specifications and a methane recovery of 99 %, from a feed mixture of 80 %/20 % CH_4/N_2. [22]

b) Activated Carbon

In contrast to the other sorbents, the unique surface property of activated carbon is that the surface is nonpolar or only slightly polar as a result of the surface oxygenated groups and inorganic impurities. This confers advantages such as a large accessible internal surface, facilitating the adsorption of non-polar and weakly polar organic molecules. Besides, adsorbent

regeneration is an easier task once the heat of adsorption (bond strength) is generally lower on activated carbon than on other sorbents.

Adsorbent comparison studies, like the one from Xiao et al. (2017), have reported fast kinetics of both nitrogen and methane in activated carbons, such as Norit RB3. This, linked to the higher methane capacity on this material, results in an equilibrium selectivity towards methane. [23]

A promising study of activated carbon for nitrogen and methane separation was reported by Brandani et al. (2021); using Norit RB2 in a four-step PSA enabled the reaching of substantially high methane recovery (more than 98 %) for a methane purity higher than 96 %. [5] Still, this is not the ideal case for energy purposes since methane is obtained at the heavy end of the column.

2.4.2 Zeolites

Zeolites have a crystalline framework structure composed of silicon and aluminum oxides which are covalently interconnected to form a repeating well-structured framework of cages or channels, making them porous. The size of the window apertures, which can be controlled by fixing the type and number of cations, ranges from 3 Å to 10 Å. The sorption may occur with great selectivity because of the size of the aperture (and to a lesser extent because of the surface property in the cages). [15] Zeolites can be tailored through ion exchange to affect desired gas separations by exploiting equilibrium and/or kinetic properties. The success of such tailoring depends mainly on the interrelation between the zeolite structure and the gas adsorption and diffusion characteristics. [24]

Zeolite 13X and zeolite 4A are examples of synthetic zeolites. These zeolites have an internal pore aperture greater than the kinematic diameter of both N_2 and CH_4 gases. Therefore, separations of this kind rely on equilibrium selectivity, based on differences in adsorption affinity of the components toward the adsorbent. A comparative work performed by Xiao et al. (2017), demonstrated that zeolites have a smaller methane and nitrogen capacity. This is due to the weakly polarizable characteristic of these molecules, also confirmed by a low heat of adsorption. [23] Besides, the equilibrium-based methane ideal selectivity only showed modest values for both zeolite 4A and 13X, with values of 2 and 3. An efficient separation is normally defined by a selectivity value higher than 3.

Some zeolites have been developed specifically for inducing molecular sieve type separations targeted towards N_2 removal from CH_4 gas mixtures. Indeed, they possess excellent structural stability and can be produced easily and at low costs. By adjusting the properties of zeolites by post-modification techniques such as ion-exchange, they can present higher selectivity values, as for the example of tailored clinoptilolites. [25]

2.4.3 Clinoptilolites

Clinoptilolite is a member of the heulandite group and is the most abundant of the natural zeolites. It has a two-dimensional channel structure that is formed by alternated 10-membered (channel A) and 8-membered rings (channel B), forming two parallel channels and a perpendicular to these channels intersects a third channel composed of an 8-membered ring (channel C). The unit cell is a negatively charged framework composed of SiO_4 and AlO_4 tetrahedra and needs extra framework charge-compensating cations. Typical Si/Al ratios for clinoptilolite ranges from 4 to 5. The selectivity and rate of uptake of gases are strongly influenced by the type, number, and location of the cations in these channels, manipulating the available surface area and local acid sites on the surface of the clinoptilolite. [26]

As balancing cations for silicon-aluminate anion in the neutralized frameworks, small hydrated cations, such as Na^+, K^+, Ca^{2+}, Mg^{2+}, easily enter the channels of clinoptilolite and after that compete for the exchange sites in skeleton of M(1), M(2), and M(3), respectively, in which, M(1) and M(2) are located in channel A and channel B, while M(3) is distributed in channel C, as depicted in Figure 5. [27]

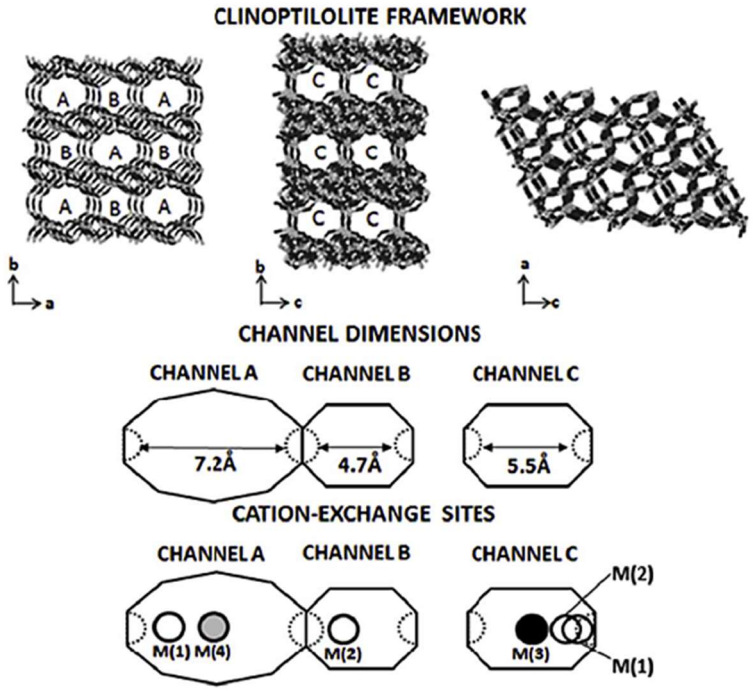

Figure 5 - Clinoptilolite channel structure and adsorption sites.[26]

In a study from Jayaraman et al., cation exchanged clinoptilolite with magnesium showed a high adsorption capacity for methane. However, a strong kinetic selectivity (diffusivity ratio) towards nitrogen value was calculated, about 300, inducing an overall kinetic separation factor of 18. This behavior is explained by the fulfillment of the M(4) sites with excess Mg^{2+}, described in Table 1.

Table 1 - Channel blockage with exchangeable cations.

Site	*Channel*	*Exchangeable cations*	*Channel A*		*Channel B*		*Channel C*	
			N_2	CH_4	N_2	CH_4	N_2	CH_4
M(1)/M(2)	A/B	Na^+, Ca^{2+}	pb	pb	cb	cb	pb	pb
M(3)	C	K^+	o	o	o	o	cb	cb
M(4)	A	Mg^{2+}	pb	pb	o	o	o	o
pb – partially blocked; cb – completely blocked; o - open								

Most of the sites M(1), M(2) and M(3) are essentially unoccupied. Hence the two-dimensional Mg-Clinoptilolite structure offers little resistance to nitrogen. This is reflected in the order of magnitude faster nitrogen uptake over Purified Clinoptilolite. [28] The use of clinoptilolite for industrial applications can suffer from variations in the composition of this mineral from different source locations. Nevertheless, with purification treatment and cation exchange, this constraint can be overcome.

2.4.4 Titanosilicates

Titanosilicate molecular sieves show uniform pore size like aluminum silicate zeolites. ETS-4, a titanium silicate first developed by Engelhard Corporation, is a small pore titanosilicate molecular sieve constituted by a mixed octahedral titania/tetrahedral silica framework structure containing 8-membered rings with a reduced pore size of 4 − 6 Å. The presence of tetravalent Ti in octahedral coordination generates a charge of −2, balanced by exchangeable Na or K cations. Its ion-exchanged derivatives have been widely studied to improve thermal stability and process performance. [29] In the cases of Sr- and Ba-exchanged ETS-4, the pore openings can be thermally controlled, in which higher dehydration temperatures lead to smaller pore dimensions. This effect is referred to as the “molecular gate effect” (MGE) and has some industrial success for methane recovery under the commercial name Molecular Gate Adsorption Technology®.

Several studies have reported outstanding characteristics for ETS-4 materials, being Ba-ETS-4 the adsorbent with the highest overall kinetic separation factor existing at this time for nitrogen and methane separation. [13] Although this material shows the best features for this specific separation, its utilization was not considered for this project, mainly since it is a material that belongs to the BASF portfolio.

2.4.5 Metal Organic Frameworks (MOFs)

Metal-organic frameworks (MOFs) adsorbents are highly crystalline materials, with robustness provided by the strong bonding of inorganic molecules and linking organic units that may allow specific tailoring according to the desired application. They are highly porous materials, with extensive surface areas (300 - 7000 $m^2 g^{-1}$), composed of micropores, showing favorable properties for separating gas molecules similar in size.

The two most promising materials for N_2-CH_4 separation are designed MIL-100 (Cr) and MIL-101 (Cr), which stands for Materials of Institute Lavoisier. Research developed in Korean Research Institute of Chemical Technology (KRICT) by Yoon et al. (2017) and Pillai et al. (2017), revealed that when MIL-100 (Cr) powder activated at 543 K, presents an equilibrium separation factor selective to nitrogen of 5, from pressures between 0.2 to 2 bar and 283 K. Analysis of the single component adsorption mechanism confirmed that the higher N_2-affinity of these materials is driven by specific interactions with coordinatively unsaturated chromium (III) sites incorporated in the MOFs architecture, leading to an electron back donation from the occupied Cr (III) d_{xz} of the cluster to the unoccupied π^*-orbital of N_2. This behavior is dependent on the activation temperature of the sorbent. [30,31]

However, the synthesis of unique MOFs at low cost and large scale remains one of the primary challenges for applying these materials in a commercial-scale process separation. [8]

3 Materials and Methods

3.1 Adsorbent selection

Based upon the comparative study performed of the suitable adsorbents for CH_4/N_2 separation, the chosen adsorbents for this project analysis were Purified Clinoptilolite, and the cation exchanged Magnesium Clinoptilolite.

The selection process held into consideration that it was preferable to obtain methane as the light product, to prevent the repressurization of CH_4 back to pipeline pressure. From the adsorbent literature review, it was possible to understand that most commercially available and industrially used adsorbents are thermodynamically selective to methane. Therefore, the only way of obtaining methane at the high-pressure stream is by choosing an adsorbent that allows a kinetically-controlled separation.

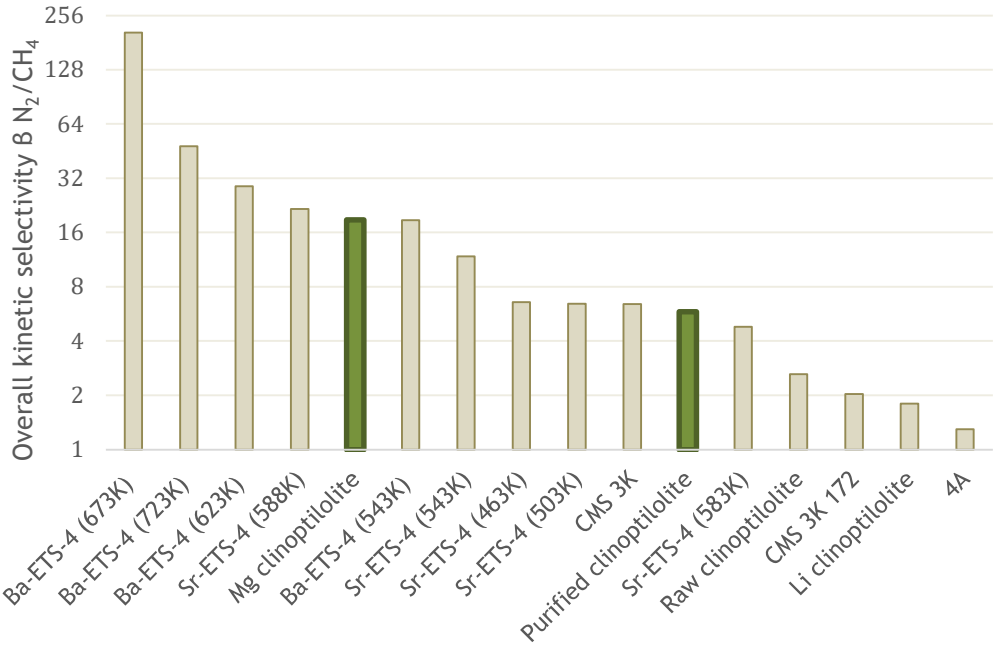

Figure 6 - Overall kinetic selectivity values for nitrogen selective adsorbents found in literature.

Discarding titanosilicates, the best results for overall kinetic selectivity to nitrogen belonged to Mg-Clinoptilolite. Even though this adsorbent has higher methane capacity at equilibrium, the differences in diffusivity of nitrogen and methane in this material overcome that aspect, since the overall kinetic selectivity towards nitrogen presents an acceptable value of 18 for separation purposes (from pure component data analysis).

Information about the unit cell composition of each of the selected clinoptilolites can be found in the Annex D.

3.1.1 Adsorbent's isotherm

The low-pressure isotherm data for the considered adsorbents were taken from Aackley and Yang (1991) work, defined below as the "experimental" values. [32] As the only available information was for the low-pressure range, the high-pressure isotherm for the pure component was predicted by extrapolation using the Langmuir Isotherm Model, expressed by:

$$q_i = \frac{q_{i,sat}\, b_{0,i} e^{-\frac{\Delta H_i}{RT}} P}{1 + b_{0,i} e^{-\frac{\Delta H_i}{RT}} P} \tag{3.1}$$

where q_i is the adsorption capacity, $q_{i,sat}$ is the maximum adsorption capacity for each component, $b_{0,i}$ is the Langmuir's adsorption affinity constant, R is the gas constant, T the temperature, P is the pressure, and ΔH_i is the Langmuir's isosteric heat of adsorption, that was computed from two isotherms at different temperatures (for 300 K and 323 K).

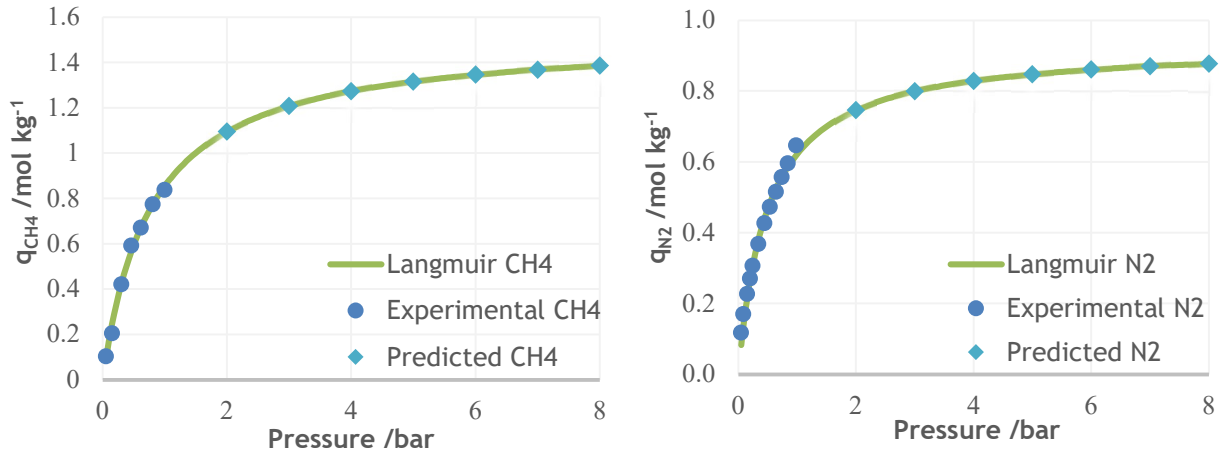

Figure 7 - Pure component adsorption isotherm of methane and nitrogen for Purified Clinoptilolite, at 300 K.

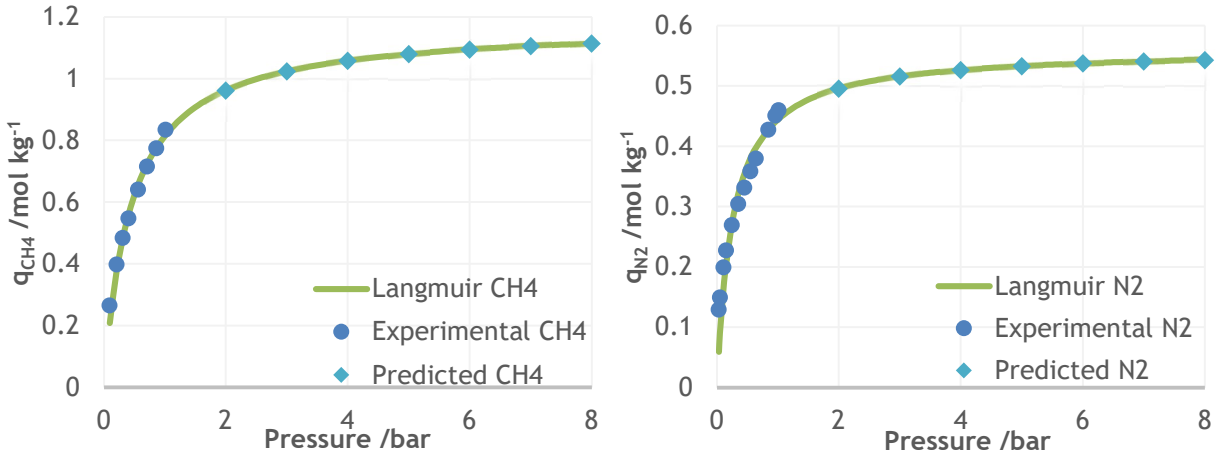

Figure 8 - Pure component adsorption isotherm of methane and nitrogen for Mg-Clinoptilolite, at 300 K.

Table 2 - Isotherm parameters obtained from the Langmuir Model and fitting error.

		q_{sat} (mol kg^{-1})	b_0 (bar^{-1})	(-ΔH) (kJ mol^{-1})	RMSD
Purified Clinoptilolite	CH_4	1.52	1.06 x 10^{-3}	-17.73	1.89 %
	N_2	0.93	1.93 x 10^{-5}	-28.82	1.74 %
Mg-Clinoptilolite	CH_4	1.18	2.60 x 10^{-5}	-28.36	1.26 %
	N_2	0.56	2.43 x 10^{-4}	-24.09	3.19 %

Concentration-dependent diffusion time constants ($D_C/{r_p}^2$) were determined from gravimetric uptake measurements, and the published results are depicted in Table 3. [28]

Table 3 – Diffusion time constants in the micropores for nitrogen and methane.

	$D_C/{r_p}^2$ (s^{-1})	
	N_2	CH_4
Purified Clinoptilolite	1.10 x 10^{-3}	2.00 x 10^{-5}
Mg-Clinoptilolite	1.80 x 10^{-2}	6.00 x 10^{-5}

The temperature dependence of diffusivity is described by the Arrhenius equation:

$$D_C = D_0 \, e^{-\frac{E_A}{R\,T}} \tag{3.2}$$

where D_C states for diffusivity, D_0 is the diffusivity at zero adsorbate concentration and E_A is the activation energy of the diffusion process.

3.2 Aspen Adsorption configuration

The programme used for the simulation of the PSA separation was *Aspen Adsorption V12*. For this work, gas Dynamic mode was chosen as the initial step for the configuration. The flowsheet is made up by the *Gas Bed*, *Gas Tank Voids*, *Gas Valves*, *Gas Feed* and *Gas Product* streams. All these blocks are connected by *Gas Material Connection Streams*. The *Gas Bed* block is used to rigorously model an adsorption bed. Since it characterizes the global adsorption process, it is the block that requires the most specification. Other relevant information about the remaining blocks constituent of the flowsheet can be consulted in Appendix D.

3.2.1 Adsorption bed configuration

The single-layer adsorption bed design was defined as a vertical bed type, 1-D spatial dimensions without any internal heat exchanger. The chosen discretization method was

Upwind Differencing Scheme 1 (USD1), since it shows one of the best standard methods in terms of accuracy, stability, and simulation time. The bed length was divided into 20 equally divided nodes, for the integration calculation within the programme.

3.2.1.1 Material balance

Material balance was based upon the assumption of mass convection with constant dispersion. Only axial dispersion was considered, neglecting the radial effects. Assuming ideal gas behavior for the gas phase, the material balance equation for each component is expressed as follows:

$$\frac{\partial \left(u\, c_{g_i}\right)}{\partial z} - D_{ax}\, \varepsilon_b \frac{\partial^2 c_{g_i}}{\partial z^2} + \left[\varepsilon_b + (1-\varepsilon_b)\, \varepsilon_p\right] \frac{\partial c_{g_i}}{\partial t} + \rho_p (1-\varepsilon_b) \frac{\partial q_i}{\partial t} = 0 \tag{3.3}$$

where c_{g_i} is the gas phase concentration of the component, u is the superficial velocity, D_{ax} is the axial dispersion coefficient, ε_b is the bulk porosity, ε_p is the intra-particle porosity, ρ_p is the particle density, and finally q_i is the adsorbed phase concentration.

3.2.1.2 Momentum balance

For the momentum balance, it was considered that the pressure drop along the column was defined by Ergun equation, which combines the description of pressure drops by the Karman-Kozeny equation for laminar flow and the Burke-Plummer equation for turbulent flow.

$$-\frac{\partial P}{\partial z} = 150\, u\, \frac{\mu_f\, (1-\varepsilon_i)^2}{\left(2\, r_p\, \psi\right)^2\, {\varepsilon_i}^3} + 1.75\, u^2\, \frac{\rho_f (1-\varepsilon_i)}{2\, r_p\, \psi\, {\varepsilon_i}^3} \tag{3.4}$$

where μ_f is the viscosity of the fluid mixture, ψ is the sphericity of the particle, and ρ_f is the fluid density.

3.2.1.3 Kinetic model

The model kinetics, such as resistances, diffusivities, and mass transfer coefficients, were specified. Typically, several mass transfer resistances occur in gas phases adsorption processes, such as the mass transfer resistance between the bulk gas phase and the gas-solid interface and the mass transfer resistance due to the porous structure of the adsorbent. For kinetics assumption, the Lumped resistance model was chosen. This model considers that the separate mass transfer resistances are lumped in a single overall factor, which for this case was only dependent on the resistance in micropores.

The migration of the adsorbate molecules from the gas phase into the adsorbent and vice-versa was assumed to be described by the linear driving force model, expressed for the solid phase loading:

$$\frac{\partial q_i}{\partial t} = k_{L,i}\, ({q_i}^* - q_i) \tag{3.5}$$

where $k_{L,i}$ is the mass transfer coefficient of the component, calculated from the component diffusivity constant $D_{C,i}$ and the particle radius r_p , and q_i^* is the adsorbed phase concentration in equilibrium with gas phase. The Glueckauf approximation of a lumped mass transfer coefficient states that

$$k_{L,i} = \frac{\Omega\, D_{C,i}}{{r_p}^2} \tag{3.6}$$

with Ω value considered to be 15. [33]

For lumped kinetics, the intra-particle porosity (ε_p) assumes a null value, and therefore the inter-particle porosity (ε_i) is the same as the bulk porosity (ε_b):

$$\varepsilon_b = \varepsilon_i + (1 - \varepsilon_i)\varepsilon_p = \varepsilon_i \tag{3.7}$$

3.2.1.4 Isotherm model

The equilibrium loading is given by the Extended Langmuir Model isotherm. This model can describe adsorption equilibrium for a multicomponent system. The assumptions made by this model are the same applied to the Langmuir (for the treatment of pure component systems), they are: each site occupying only one molecule, no mobility on the surface, and constant heat of adsorption. Furthermore, it is considered that the constants for adsorption and desorption for all species are invariant. [20]

The model expression is described as follows, for a binary mixture:

$$q_i = \frac{q_{i,sat}\, b_{0,i} e^{-\frac{\Delta H_i}{R\,T}} p_i}{1 + \sum b_{0,j} e^{-\frac{\Delta H_j}{R\,T}} p_j} \tag{3.8}$$

where $q_{i,sat}$ is the maximum adsorption capacity for each component, $b_{0,i}$ is the Langmuir's adsorption affinity constant, and ΔH_i is the Langmuir's isosteric heat of adsorption.

3.2.1.5 Energy balance

The assumed energy balance was non-isothermal and non-adiabatic, with gas and solid conduction. This option includes the thermal conduction term for both gas and solid phases, considering a constant gas thermal conductivity and constant heat transfer coefficient. Moreover, "Thin Wall" model was used, in which there are no resistances considered to the heat transfer from the column to the exterior.

$$\begin{aligned} -\varepsilon_b\, k_g \frac{\partial^2 T_g}{dz^2} + C_{vg}\, u\, \rho_g \frac{\partial T_g}{\partial z} + \frac{\partial (uP)}{\partial z} + C_{vg}\, \rho_g\, \varepsilon_b \frac{\partial T_g}{\partial t} - k_s \frac{\partial^2 T_s}{dz^2} + C_{ps}\, \rho_b \frac{\partial T_s}{\partial t} \\ + \rho_p \sum\nolimits_i \left(\Delta H_i \frac{\partial q_i}{\partial t}\right) + \frac{2\, h_w}{r_b}(T_W - T) = 0 \end{aligned} \tag{3.9}$$

where k_g is the gas thermal conductivity, C_{vg} is the gas heat capacity, ρ_g stands for the gas density, T_g and T_s are gas and solid temperature, respectively, k_s is the solid thermal conductivity, C_{ps} is the solid heat capacity, h_w is the heat transfer coefficient, r_b is the bed radius and T_W is the column wall temperature.

3.2.1.6 Bed layer specification

Clinoptilolite adsorbents were specified in the *Bed Layer Specify Table* section in the *Aspen Adsorption* programme. Input data are expressed in the Table 4, based upon the model assumptions previously described. For modified clinoptilolites, the basic framework structure remains unchanged; only the type, number, and location of the cations vary.

Table 4 – Aspen input parameters.

			Purified Clinoptilolite		***Mg-Clinoptilolite***	
			CH_4	**N_2**	**CH_4**	**N_2**
IP1	kmol kg^{-1} bar^{-1}	isotherm parameter 1	1.61×10^{-6}	1.80×10^{-8}	3.06×10^{-8}	1.36×10^{-7}
IP2	K	isotherm parameter 2	2.13×10^{3}	3.47×10^{3}	3.41×10^{3}	2.90×10^{3}
IP3	bar^{-1}	isotherm parameter 3	1.06×10^{-3}	1.93×10^{-5}	2.60×10^{-5}	2.43×10^{-4}
IP4	K	isotherm parameter 4	2.13×10^{3}	3.47×10^{3}	3.41×10^{3}	2.90×10^{3}
MTC	s^{-1}	mass transfer coefficient	3.00×10^{-4}	1.65×10^{-2}	9.00×10^{-4}	2.70×10^{-1}
E_i	-	inter-particle voidage	0.4 [28]			
RHO	kg m^{-3}	bulk density	695 [28]			
R_p	m	adsorbent particle radius	1.00×10^{-3}			
E_z	m^2 s^{-1}	constant dispersion coefficient	9.02×10^{-5}			
Cps	MJ kg^{-1} K^{-1}	adsorbent specific heat capacity	1.35×10^{-3} [34]			
HTC	MW m^{-2} K^{-1}	constant for the heat transfer coefficient	1.41×10^{-4}			
H_w	MW m^{-2} K^{-1}	heat transfer coefficient gas and wall	0.003			
K_g	MW m^{-1} K^{-1}	constant for the gas phase heat conductivity	1.41×10^{-7}			
K_s	MW m^{-1} K^{-1}	adsorbent thermal conductivity	1.50×10^{-4}			
T_{amb}	K	ambient temperature	300			

Further calculation information for the IPs and thermodynamic constants is addressed in Appendix E.

4 Results and discussion

The simulation results were obtained based on the following model assumptions: 1) ideal gas behavior; 2) axial dispersed plug flow; 3) non-isothermal non adiabatic bed with gas and solid conduction; 4) there is heat exchange between the gas in the bed and the environment; 5) negligible external film diffusional resistances compared to micropore resistances; 6) constant diffusivity model; 7) lumped resistance model with linear driving force; 8) equilibrium relations for both components are represented by the Extended Langmuir model; 9) column pressure drop expressed by Ergun equation.

4.1 Breakthrough simulation

Breakthrough curves show the concentration of an adsorbate in the fluid phase at the outlet of the adsorption column as a function of time. From breakthrough analysis, an evaluation of the mass transfer zone within the column can be done. The shape of the breakthrough curve is crucially important in the design of cyclic separation processes, and the concentration front dispersion is influenced by both mass and heat dispersions in the axial direction, as well as mass and heat transfer resistances within the particle. [15] The basic flowsheet used in *Aspen Adsorption* for the breakthrough simulation was constituted by the feed and product boundary terminators and one adsorption bed, that were linked through gas material connections.

4.1.1 Pure component breakthrough

The pure component breakthrough simulation was performed considering a binary mixture with inert gas, in this case, Helium, which does not show any interaction with the solid surface. One of the project's initial conditions is to treat a 90 %/10 % CH_4/N_2 feed flow rate of 100 $m^3 h^{-1}$. For the pure breakthrough experiments, the exact molar fraction of each component in the mixture with Helium were taken into consideration.

The obtained pure component breakthrough, at 5 bar and 300 K, for both methane and nitrogen are represented below, in each adsorbent selected. Column dimensions used for these simulations were the company's standardized ones, of 2 m height and 70 cm diameter.

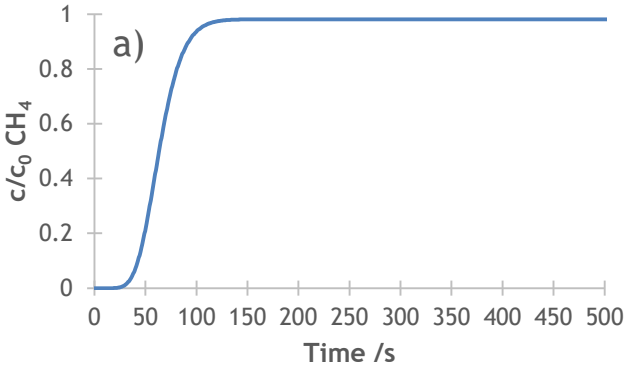

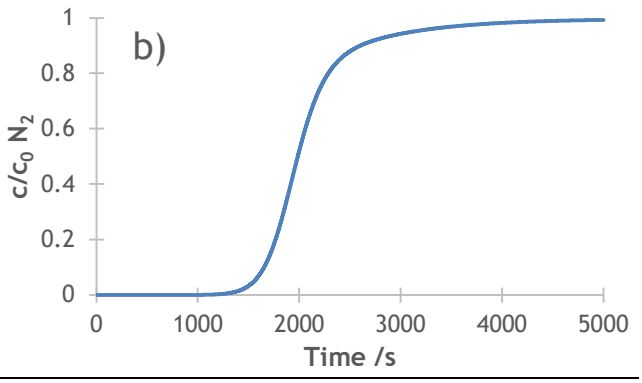

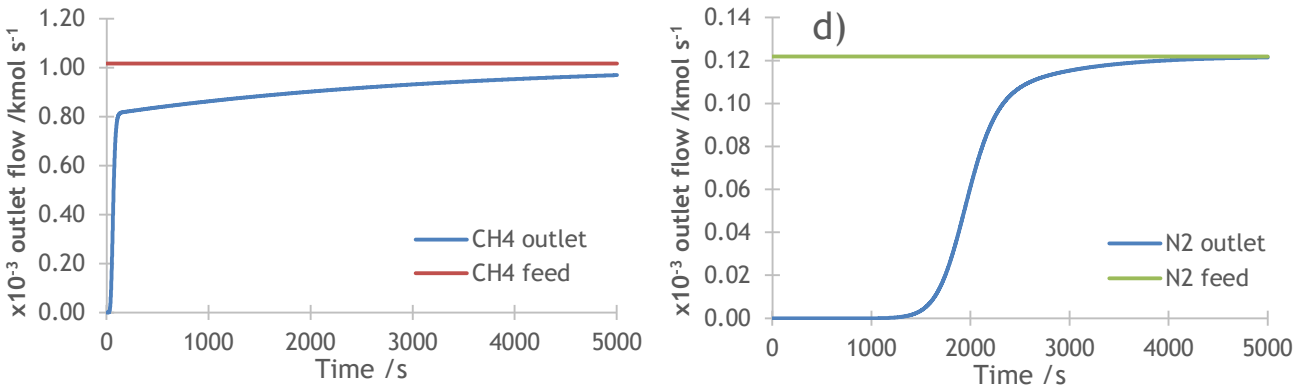

Figure 9 – Pure component breakthrough simulation results for Purified Clinoptilolite, at 300 K and 5 bar; a) and c) mixture of 90 %/10 % CH_4/He; b) and d) mixture of 10 %/90 % N_2/He.

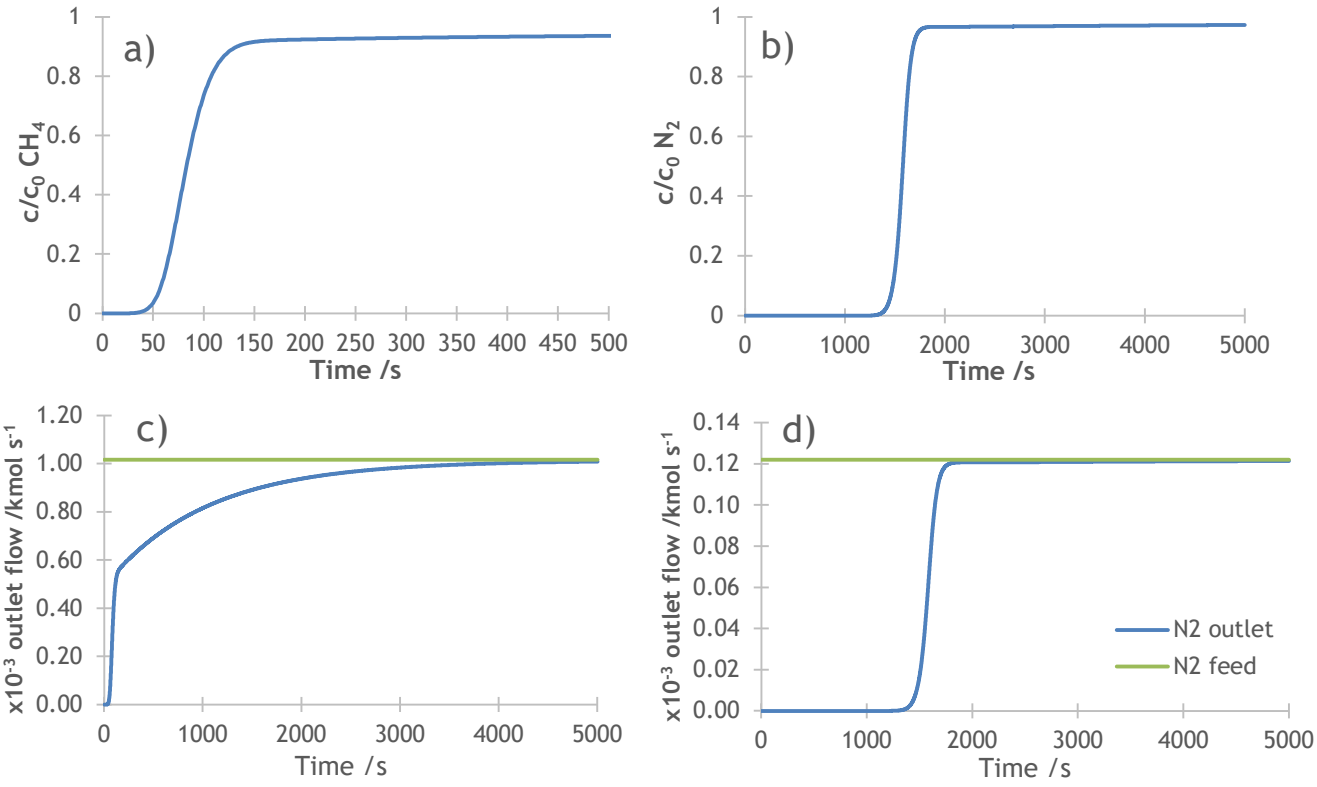

Figure 10 - Pure component breakthrough for Mg-Clinoptilolite, at 300 K and 5 bar; a) and c) mixture of 90 %/10 % CH_4/He; b) and d) mixture of 10 %/90 % N_2/He.

From these simulations, it is possible to obtain the breakthrough time for each component, which is the fundamental operating time for the adsorption step in a PSA process; it corresponds to the time at which the outlet concentration reaches a percentage of 5 % of the inlet one.

Table 5 - Breakthrough times for both adsorbents.

	CH_4	N_2
Purified Clinoptilolite	37 s	1554 s
Mg-Clinoptilolite	54 s	1443 s

Nitrogen selectivity, as demonstrated by the time lag between the breakthrough of the light and the heavy components, is used to claim process success. By the curves obtained, it is clear that the bed dynamic is being controlled by kinetics, once methane (the component for which both adsorbents have equilibrium selectivity) presents a breakthrough time far from the stoichiometric time, predicted by its adsorption isotherm. Methane mass transfer resistance is noticed in both solid materials by the rapid reaching of this component to the top of the column, as proved by the outlet stream represented in the breakthrough graphs. As methane's diffusion time constant is higher for Mg-Clinoptilolite than for the Purified Clinoptilolite, this component will be more quickly retained in Mg-Clinoptilolite, which explains the difference in the breakthrough time as well as in the outlet molar flowrate. The convective effect of the bed overcomes the diffusion rate of CH_4 to the interior of the adsorbent.

4.1.2 CH_4/N_2 mixture breakthrough

In a gas mixture, the constituent components may present some sort of competitive behavior in respect to the available adsorption sites in the solid. Multi-component breakthrough experiments can offer insight into competitive adsorption equilibrium and provide validation to the process model used in simulation studies. For the mixture breakthrough simulation, the same initial conditions than those for the pure component simulation were applied.

- **Purified Clinoptilolite**

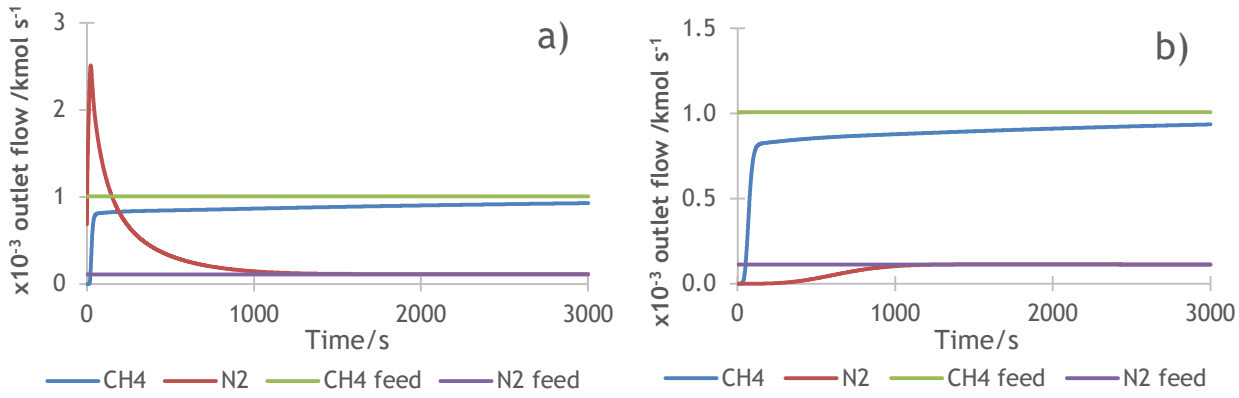

Figure 11 - Mixture breakthrough curve of 100 m^3 h^{-1} stream with 90 %/ 10 % CH_4/N_2, in Purified Clinoptilolite, at 300 K and 5 bar for: a) initial bed condition $y_{N2} = 1$; b) initial bed condition $y_{He} = 1$.

Overall kinetic selectivity was validated for this mixture case by Equation (2.5, where the mixture of 90 %/10 % CH_4/N_2, at 300 K and 5 bar, presented a satisfactory nitrogen selectivity of 7.

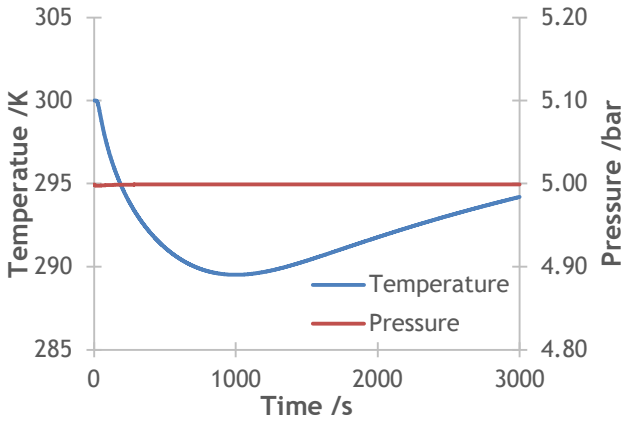

Figure 12 - Temperature and pressure history for the mixture breakthrough simulation in Purified Clinoptilolite, for initial bed condition $y_{N2} = 1$.

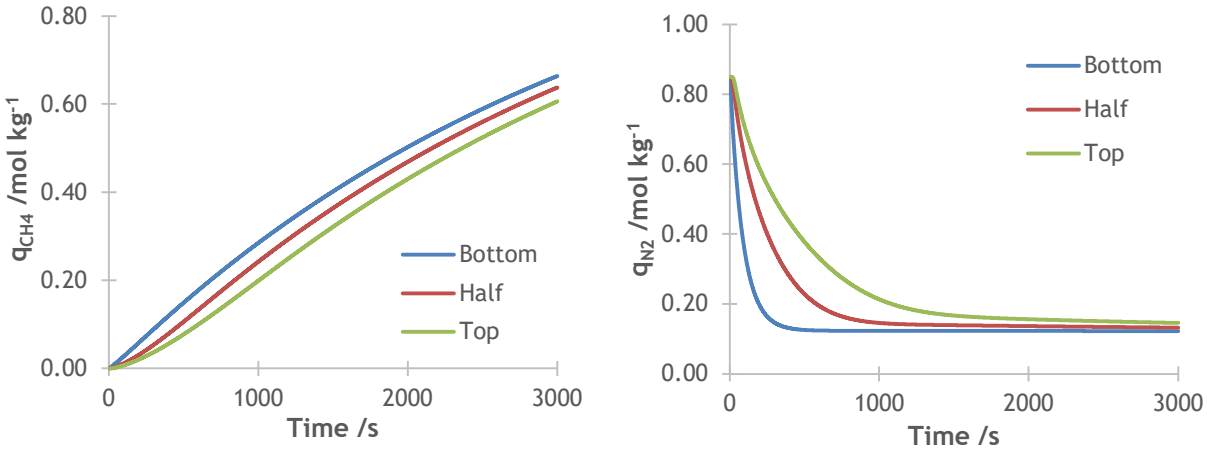

Figure 13 - Solid loading of both components in Purified Clinoptilolite, at the bottom, half, and top of the column.

Temperature decrease is consequence of the nitrogen desorption, as the bed was initially filled with this component. Equilibrium adsorption isotherms are temperature-dependent, so variations in this parameter may influence the adsorption capacity of the adsorbent since a decrease in temperature leads to an increase in adsorption capacity. In what concerns the diffusivity constant, this kinetic parameter was assumed constant at the simulation model, so the temperature variation will not interfere in this case.

- **Mg-Clinoptilolite**

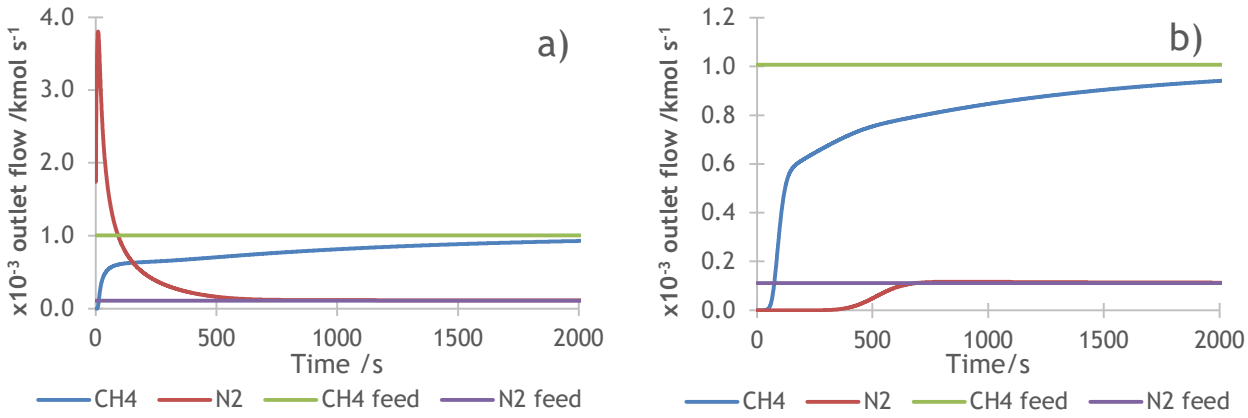

Figure 14 - Mixture breakthrough curve of 100 m^3 h^{-1} stream with 90 %/ 10 % CH_4/N_2, in Mg-Clinoptilolite, at 300 K and 5 bar for: a) initial bed condition $y_{N2} = 1$; b) initial bed condition $y_{He} = 1$.

Overall kinetic selectivity was validated for the mixture case by Equation (2.5, where the mixture of 90 %/10 % CH_4/N_2, at 300 K and 5 bar, presented a greater nitrogen selectivity of 14.

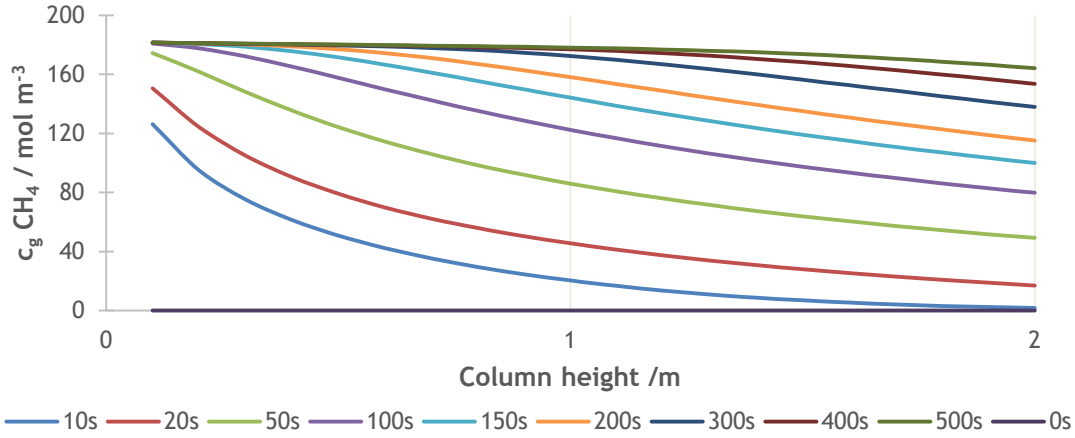

Figure 15 - Gas phase concentration profile of methane in Mg-Clinoptilolite.

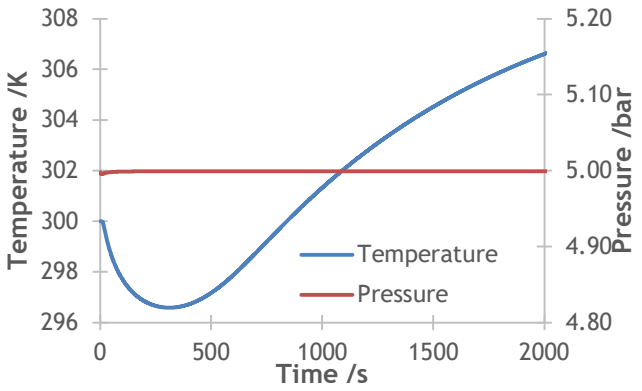

Figure 16 - Temperature and pressure history for the mixture breakthrough simulation in Mg-Clinoptilolite, for initial bed condition $y_{N2} = 1$.

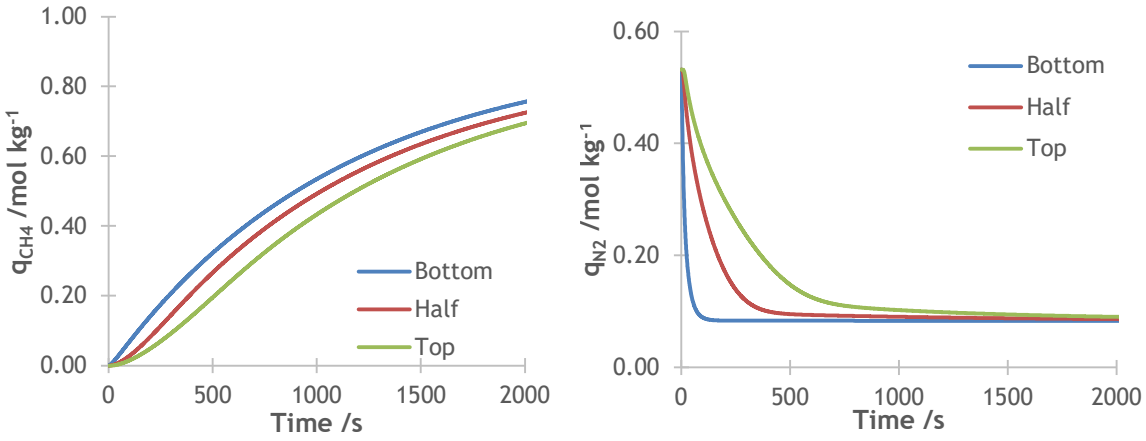

Figure 17 - Solid loading for both components in Mg-Clinoptilolite, at the bottom, half, and top of the bed.

The dynamic behavior of this separation was further analyzed by the study of different feed flow rates and their effect on the mixture breakthrough curve.

Table 6 - Feed flowrate unit conversion.

Feed		***Superficial Velocity (u)***	***Composition***
(m^3 h^{-1})	**(kmol s^{-1})**	**(m s^{-1})**	
10	1.12 x 10^{-4}	0.02	90 %/10 % CH4/N2
50	5.58 x 10^{-4}	0.04	
100	1.12 x 10^{-3}	0.07	
200	2.23 x 10^{-3}	0.14	

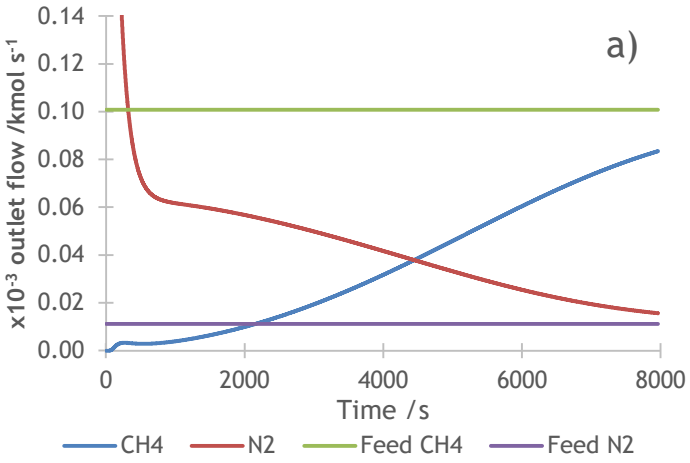

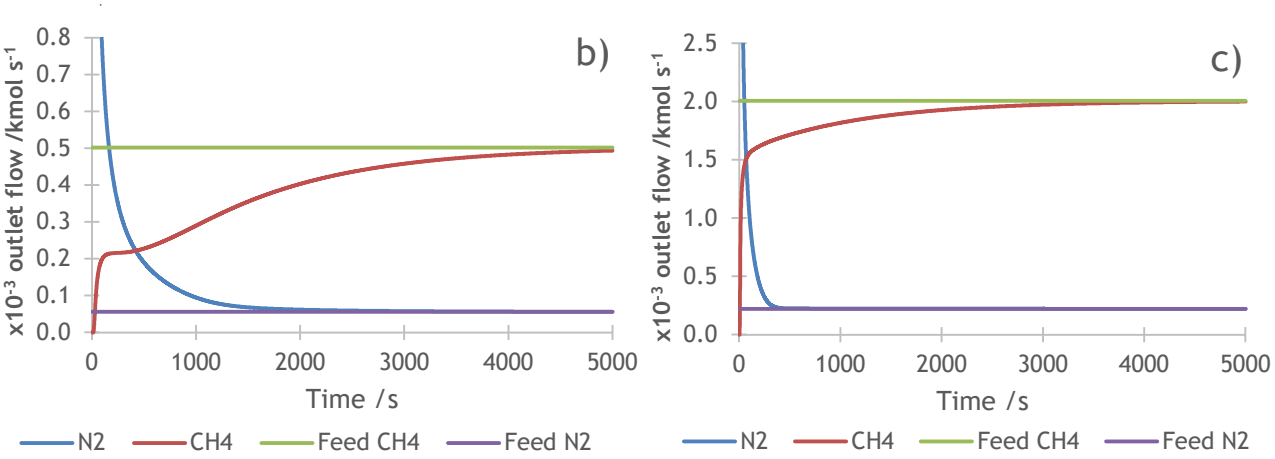

Figure 18 - Feed flowrate effect on the breakthrough for Mg-Clinoptilolite: a) 10 m^3 h^{-1}; b) 50 m^3 h^{-1}; b) 200 m^3 h^{-1}.

Kinetic differences can be noticed for different feed flowrate study, where for the higher flowrate of 200 m^3 h^{-1}, the fed methane leaves the column almost instantaneously. Compared to the other cases for lower flowrates, the breakthrough is extended in time. The higher velocity for the higher flowrate case leads to a decrease of contact time of methane molecule and the adsorbent, which adds to the greater resistance to mass transfer of this component, enables the almost immediate reaching to the feed methane composition at the outlet of the adsorption bed. For the lower flowrate of 10 m^3 h^{-1}, the breakthrough shape demonstrates an approximation of an equilibrium-controlled separation.

4.2 5-step VPSA

Following the breakthrough analysis, the PSA configuration was set to a 5-step cycle, with (I) feed pressurization, (II) high-pressure adsorption, (III) co-current blowdown, (IV) countercurrent blowdown, and (V) low-pressure purge. Figure 19 shows the schematic of the PSA cycle used.

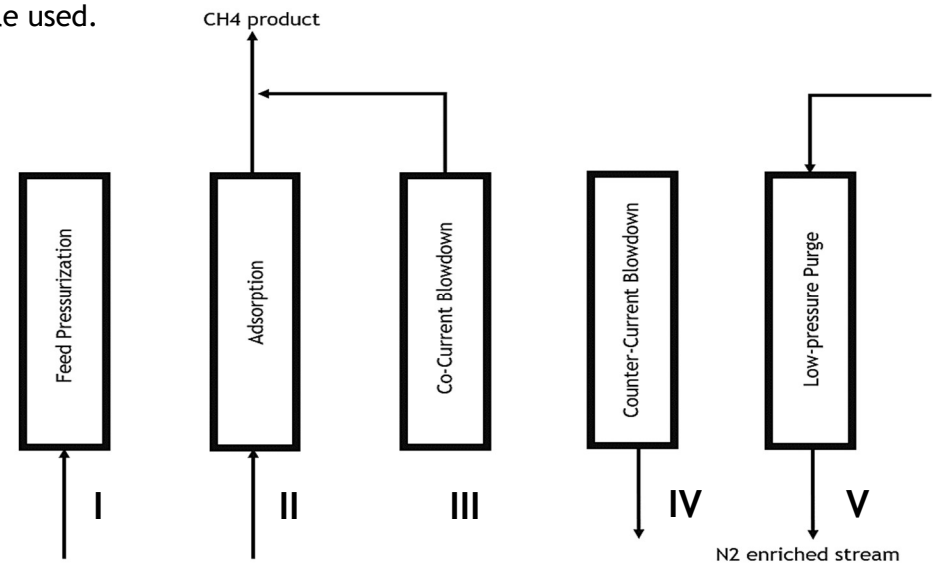

Figure 19 - PSA 5-step configuration scheme.

The simulation performed in *Aspen Adsorption* was based on a single-bed approach. Flowsheet design should be consulted in Appendix D.

PSA is a cyclic process, with at least two interconnected columns, to ensure continuous production. However, in a single-bed approach, only one of the columns is designed. The strategy used for this case relied on fixing the purge composition as the target product specification, which was defined as a 97 % CH_4 and 3 % N_2 stream, for a fixed flowrate.

The starting point for the simulations is expressed in Table 7. Bed dimensions considered here are the standard size used for other projects in the company. Therefore, they were taken into consideration for the calculation. Furthermore, the initial bed condition was assumed to be filled with pure nitrogen, the heavy component.

It should be noted that the results obtained and from the simulations and discussion are based on the cyclic steady state (CSS) behavior since this approach will fail to some extent to predict the transient behavior.

Table 7 – Starting point values of the most relevant parameters for the simulation.

Column height (m)	2
Column diameter (m)	0.7
Feed composition	90 %/10 % CH_4/N_2
Feed flowrate (mol/s)	1.12
High Pressure (bar)	5
Low Pressure (bar)	0.5
Fluid superficial velocity (m/s)	0.07
Pressurization time (s)	30
High Pressure Adsorption time (s)	60
Co Current Blowdown time (s)	10
Counter Current Blowdown time (s)	30
Low Pressure Purge (s)	60

As the regeneration pressure is below 1 bar, this process can be designed as Vacuum Pressure Swing Adsorption (VPSA).

There are some critical PSA performance indicators that serve as the basis of comparison between different sorbents and processes, being them the product purity and recovery. It is important to notice that the product from the co-current blowdown step is combined with the product from the adsorption step, so it should be accounted for the overall methane-rich product calculation.

The calculation method for the performance parameters considered is explained by equations ((4.1) and ((4.2):

$$Product\ Purity = \frac{(CH_4\ from\ step\ II) + (CH_4\ from\ step\ III)}{(Total\ Volume\ of\ Product\ in\ steps\ II\ and\ III)} \tag{4.1}$$

$$Product\ Recovery = \frac{(CH_4\ from\ step\ II) + (CH_4\ from\ step\ III) - (CH_4\ from\ step\ V)}{(\ CH_4\ fed\ in\ steps\ I\ and\ II)} \tag{4.2}$$

From sensitivity analysis, a fair comparison of sorbent performance can be made by using similar cycle conditions for each of the sorbents and comparing one of the process parameters with the other.

4.2.1 Sensitivity analysis for Purified Clinoptilolite

A sensitivity analysis was performed for optimization purposes, where the effect of several operating parameters on PSA were studied. The impact of independent process variables, such as the purge flowrate to feed flowrate ratio, high and low pressures, the column height to diameter ratio (or initial fluid velocity), and the final pressure in the co-current blowdown step were evaluated in terms of purity and recovery.

The steps duration were chosen based on the literature, reproducing the same used for a kinetic separation with clinoptilolites of Jayaraman et al. (2004) work. [28] Further on, the optimization of the steps time was also a matter of study.

The study was first performed only for the Purified Clinoptilolite, and later applied for the Mg-Clinoptilolite adsorbent.

Detailed information about the simulations can be found in Appendix F.

Purge to Feed ratio (*P/F*)

Purge assumed in this system is considered a fraction of the product flow rate obtained from the adsorption step. The *P/F* ratio is defined as the number of moles of CH_4 used in the purge step divided by the adsorption step. The effect on purity and recovery is expressed below.

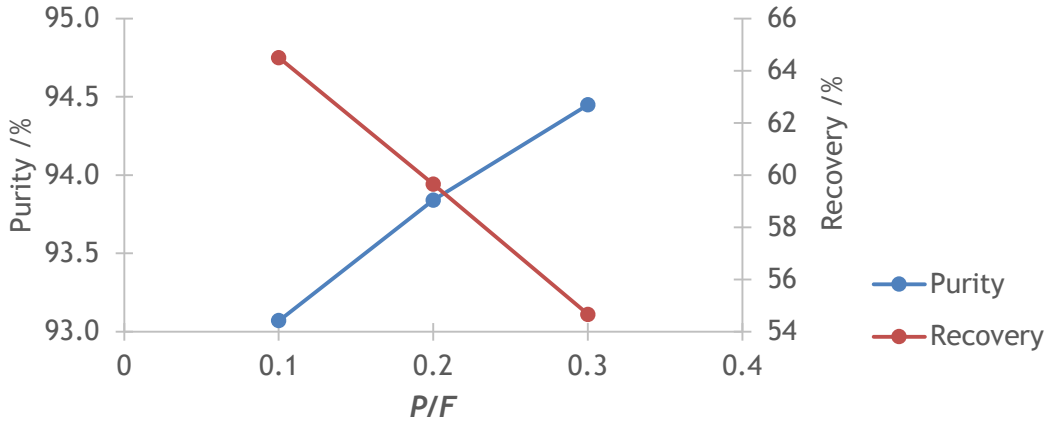

Figure 20 - Purge to feed ratio effect on the purity and recovery of the process for Purified Clinoptilolite.

The opposite behavior of purity and recovery is a common and expected result for any separation process. The decrease in product recovery for higher *P/F* values is explained by the higher amount of product displaced from the adsorption outlet to the purge step. Purge is necessary to sufficiently remove nitrogen adsorbed in the solid phase and ensure high raffinate product purity.

Adsorption operating pressure (high pressure)

Keeping the *P/F* ratio at 0.1 bar to safeguard an adequate recovery, the study for high pressure in the adsorption step was performed.

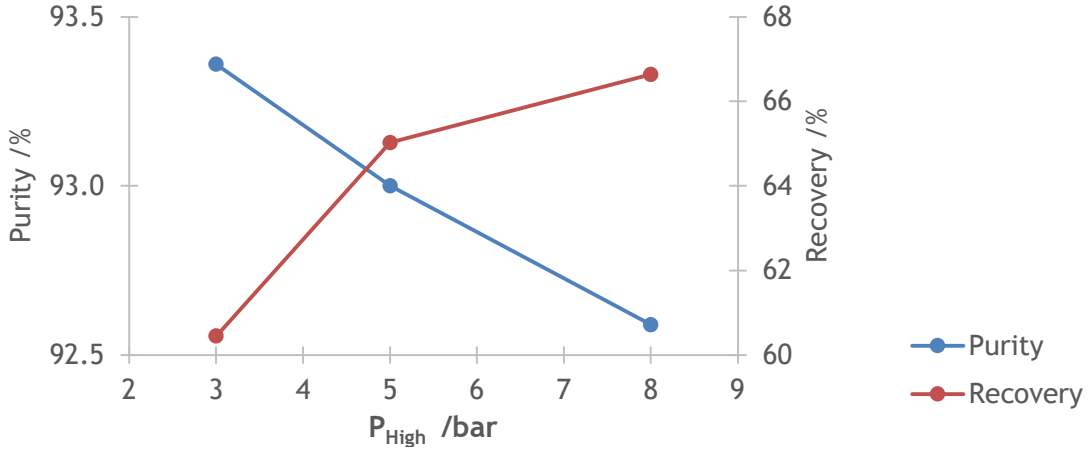

Figure 21 - Adsorption operating pressure effect on the purity and recovery of the process for Purified Clinoptilolite.

The inlet flow rate during the adsorption step is fixed, so only feed pressure variation is considered. Higher pressure will lead to more methane adsorbed capacity in the solid, as expected by the equilibrium isotherm. For superior pressures, the working capacity of the process is higher once there is a significant adsorbent capacity difference between high pressure and low pressure of operation. The observed decrease in purity is related to the pressurization step: to keep the step times fixed, the pressurization flow rate increased to reach the higher operating pressure by valve CV value manipulation. This leads to an increased amount of methane inside the bed, which is the component for which the adsorbent shows equilibrium affinity after the pressurization step.

Due to the longer residence time and higher methane concentration and capacity for increased pressures, nitrogen retained in the solid is replaced by methane molecules, which contaminates the raffinate product, resulting in purity decrease.

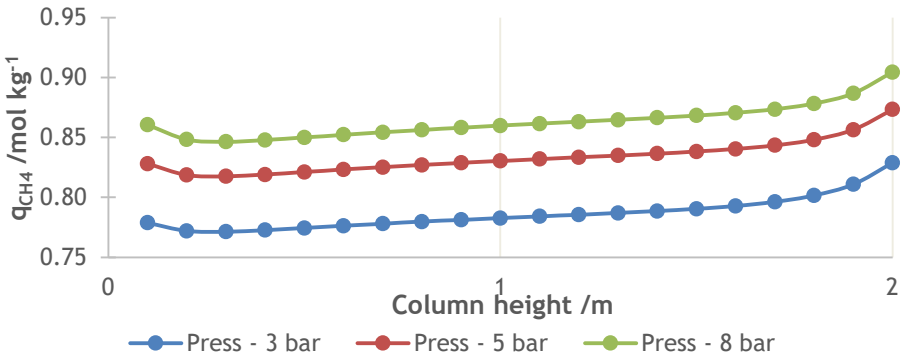

Figure 22 - Methane solid loading at the end of the pressurization step for different operating adsorption pressure in Purified Clinoptilolite.

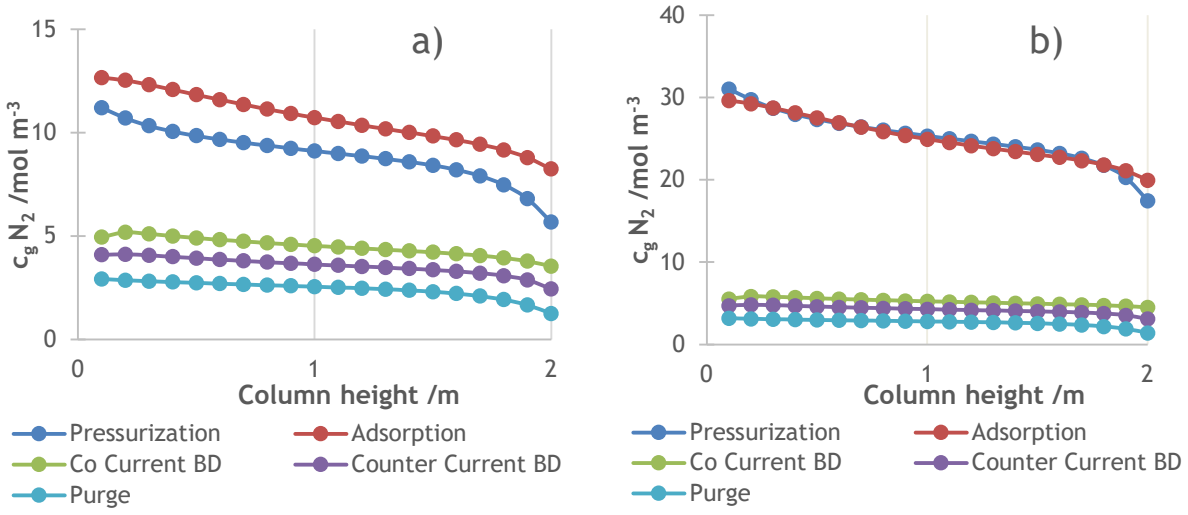

Figure 23 - Gas phase concentration of nitrogen along the bed at the end of each step in Purified Clinoptilolite, for an operating adsorption pressure of: a) 3 bar; b) 8 bar.

Velocity effect (u)

The initial superficial velocity is calculated based on the feed flowrate for the adsorption step and the cross-sectional area of the bed. As the feed flowrate was already set and fixed for this project, as 100 $m^3\ h^{-1}$, changing the superficial velocity is the same as adjusting the column height to diameter ratio (L/D) while keeping a constant bed volume.

An important aspect of having in consideration is that the superficial velocity of the gas mixture must not be higher than the minimum fluidization velocity (U_{mf}), so that the procedure occurs in a fixed bed. The calculation of the U_{mf} was based on the Ergun equation (Equation (3.4), and the value obtained was 0.66 m s^{-1}, indicating the maximum allowable gas velocity for this process under the specified conditions.

Table 8 - L/D variation description.

Feed flowrate ($m^3\ h^{-1}$)	Feed flowrate (mol s^{-1})	Effective volume (m^3)	u (m s^{-1})	u_i/U_{mf}	L/D	L (m)	D (m)
100	1.12	0.31	0.07	0.27	2.86	2.00	0.70
			0.11	0.40	5.00	2.90	0.58
			0.17	0.63	10.00	4.61	0.46

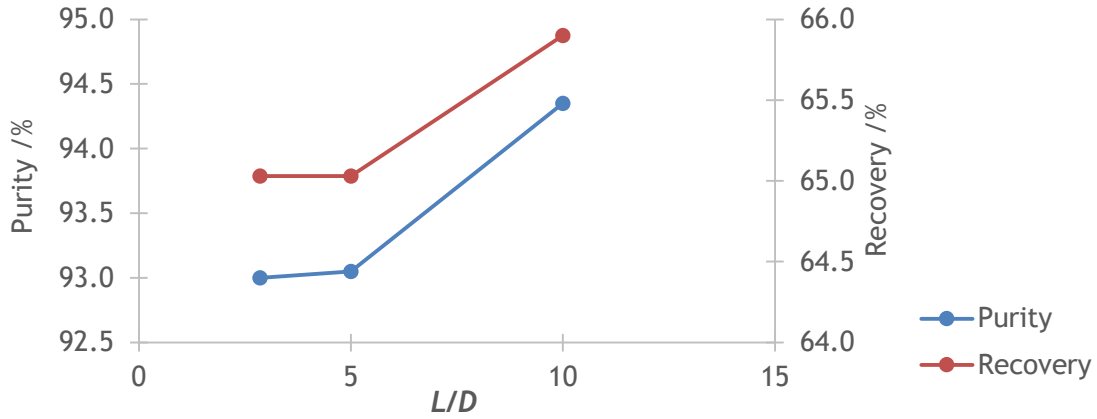

Figure 24 - Bed length to diameter ratio effect on the purity and recovery of the process, in Purified Clinoptilolite.

The main interference of velocity variation is the contact time of the gas mixture components with the adsorbent. When the velocity is higher, this interaction is reduced for the slower diffusing component in the mixture, as well as its concentration in the solid phase, so more methane is collected at the product stream. This leads to an increase in both purity and recovery. A higher L/D ratio is also linked to a closer approximation of the ideal plug flow behaviour inside the bed; on the other hand, it can result in a higher pressure drop along the column that might be alleviated by valve control.

Final pressure of Co-Current Blowdown step

The final product obtained is an averaged quantity from the adsorption step and the co-current blowdown step, being the final pressure in co current depressurization an important parameter to evaluate for purity and recovery enhancement.

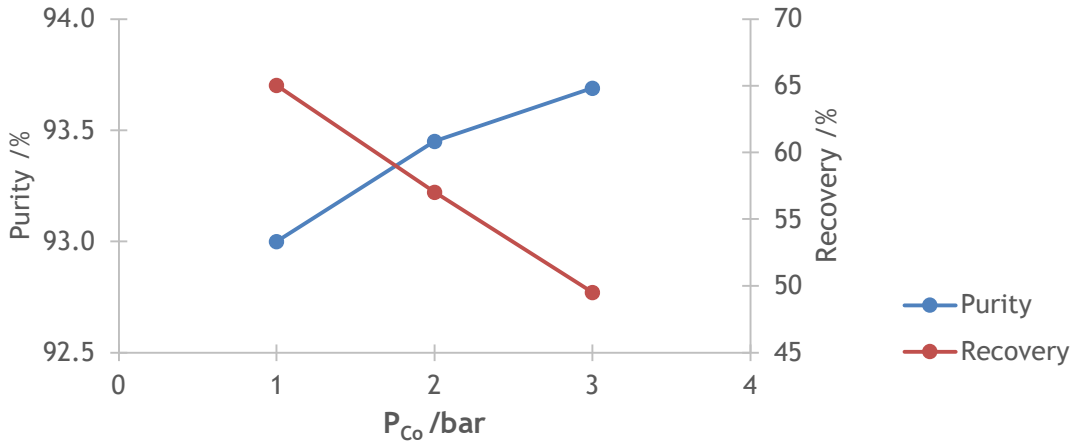

Figure 25 - Final co current blowdown pressure effect on the purity and recovery of the process, in Purified Clinoptilolite.

Recovery is at its highest when the final pressure of co-current blowdown is 1 bar, with a considerable difference in methane recovery from the other studied ending pressures.

The impact of a co-current blowdown in the PSA process is that it enables the gas expansion and recovery of the existing light component within the bed void spaces - porosity.

Low operating pressure

The low pressure of desorption was concluded to be the most relevant parameter to consider to reach the target purity.

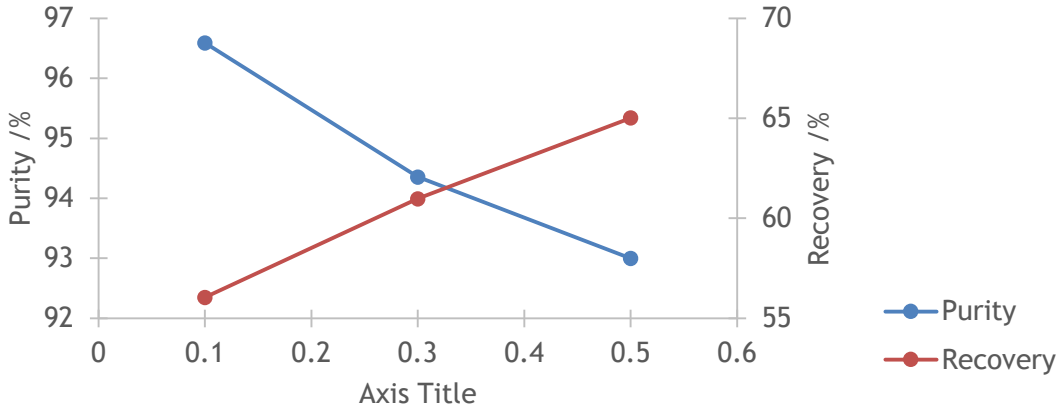

Figure 26 - Counter current blowdown end pressure effect on the purity and recovery of the process, in Purified Clinoptilolite.

Only by lowering the low pressure to conditions of 0.1 bar, the targeted 97 % methane purity was achieved. From the adsorption isotherm, it is possible to recognize that the steeper region of adsorbed quantity is for the low-pressure range (below 1 bar). Even though kinetic limitations control the separation, a significant amount of methane is also being adsorbed during the process, mainly due to its high presence in the feed composition. Hence, very low depressurization pressures are ideally required to assist in the effective removal of the adsorbed components and regeneration of the adsorbent since it moves the operating process to the linear regions of the isotherm.

The best results obtained for Purified Clinoptilolite after the study on the sensitivity analysis can be consulted in Table 9.

Table 9 - Optimized parameters for Purified Clinoptilolite.

Run	u (m s^{-1})	*L/D*	*P/F*	P_{High} (bar)	P_{Co} (bar)	P_{Low} (bar)	L (m)	Purity	Recovery
25	0.07	2.86	0.1	5	1	0.1	2	**96.66 %**	**58.34 %**

Pressure history at cyclic steady state (CSS) is depicted in the graph below, where it can be verified a slight pressure decrease in the adsorption step. This pressure variation in the second step might be related to the product valve configuration.

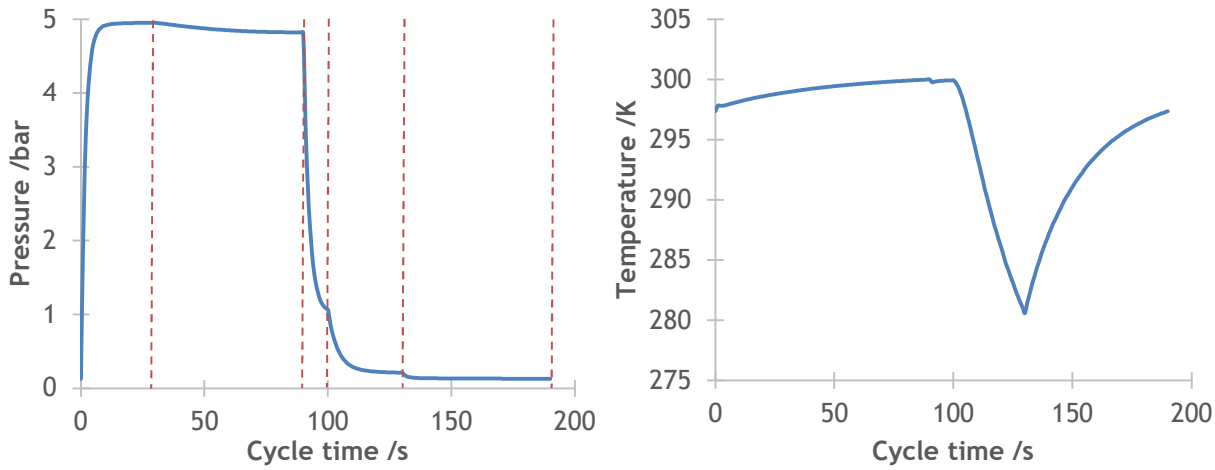

Figure 27 - Pressure and temperature history on the top of the bed at CSS for Purified Clinoptilolite.

Analyzing the temperature history, some adsorption concepts can be verified. The increase in temperature during adsorption step is linked to the exothermic phenomena of adsorption, which proves that molecules are being retained in the adsorbent. The steep temperature drop to 280 K is associated with the regeneration step for vacuum operating conditions. However, by examining the temperature profile along the column, it is possible to conclude that this steep variation is only felt at the top of the bed. So an approximation to isothermal behavior can be verified for the rest of the column length, with a temperature variation of about 2 %.

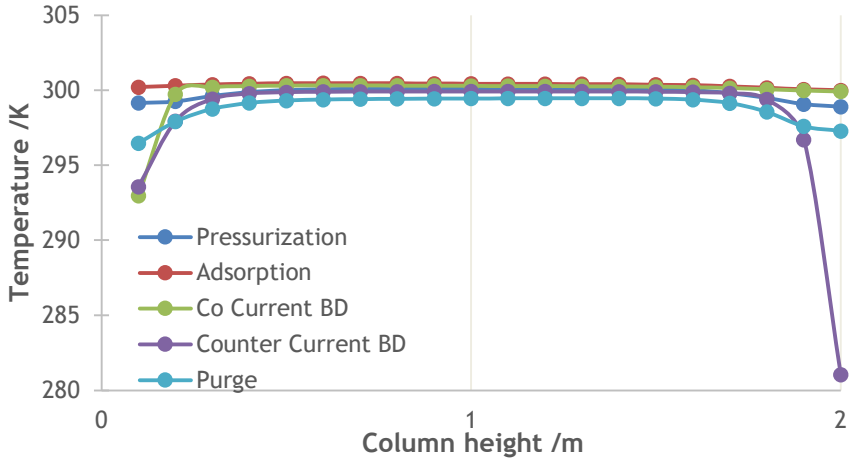

Figure 28 - Temperature profile along the 2 m bed height, for run 25 in Purified Clinoptilolite.

Methane mass transfer resistance in the solid material is clear from the constant gas phase concentration profile represented in Figure 29.

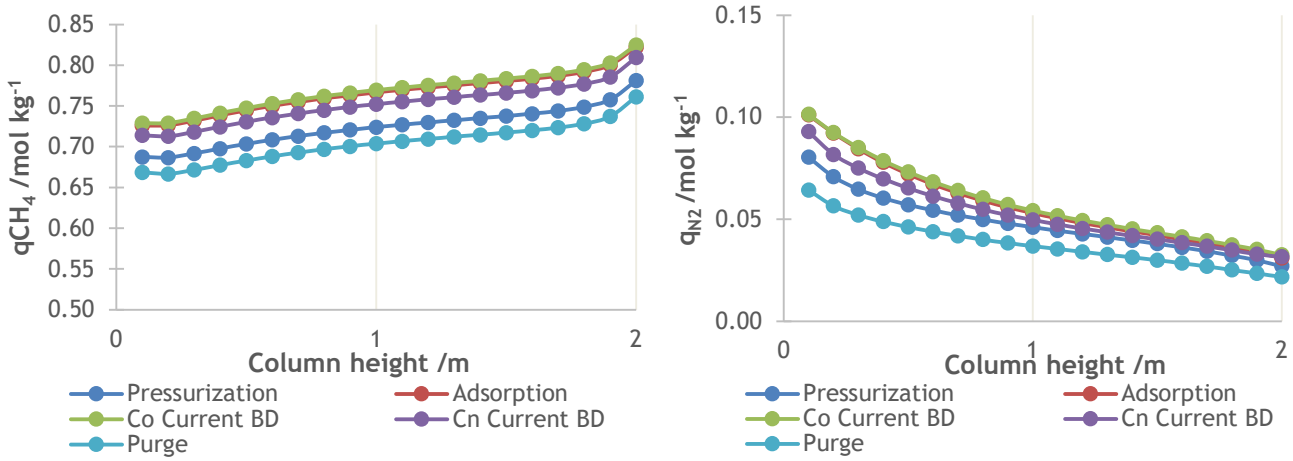

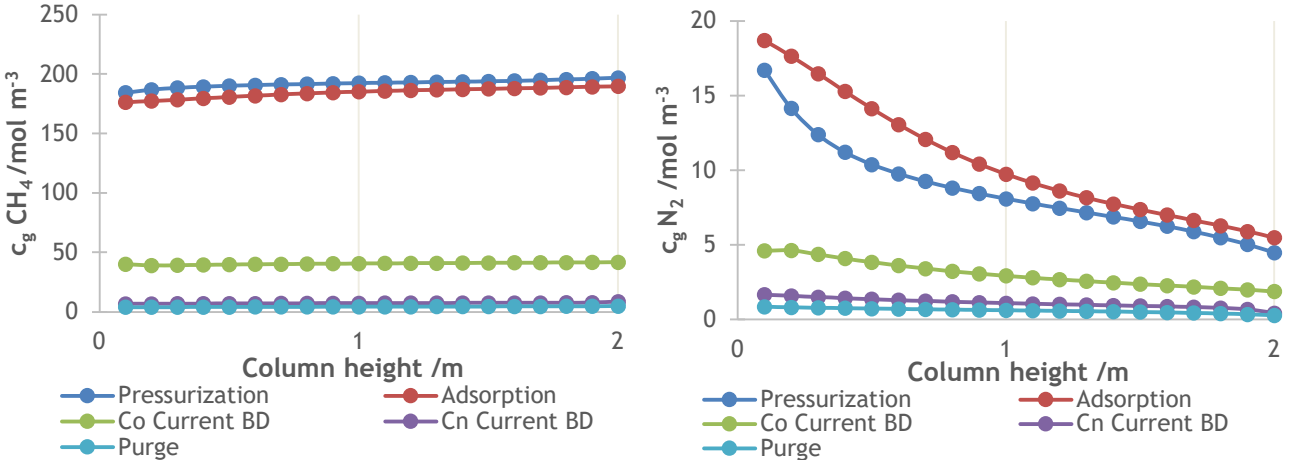

Figure 29 - Solid and gas phase concentration profile of both components in Purified Clinoptilolite, at the end of each step, for run 25.

4.2.2 Optimized parameters applied for Mg-Clinoptilolite

Following the study on the effects of each independent parameter, the optimized conditions were applied for the other adsorbent considered in this study, Mg-Clinoptilolite. As this material presents an even higher nitrogen kinetic selectivity, the results were more promising than those for Purified Clinoptilolite.

Table 10 - Optimized parameters applied in Mg-Clinoptilolite.

Run	u (m s^{-1})	*L/D*	*P/F*	P_{High} (bar)	P_{Co} (bar)	P_{Low} (bar)	L (m)	Purity	Recovery
49	0.07	2.86	0.1	5	1	0.1	2	**98.28 %**	**76.07 %**

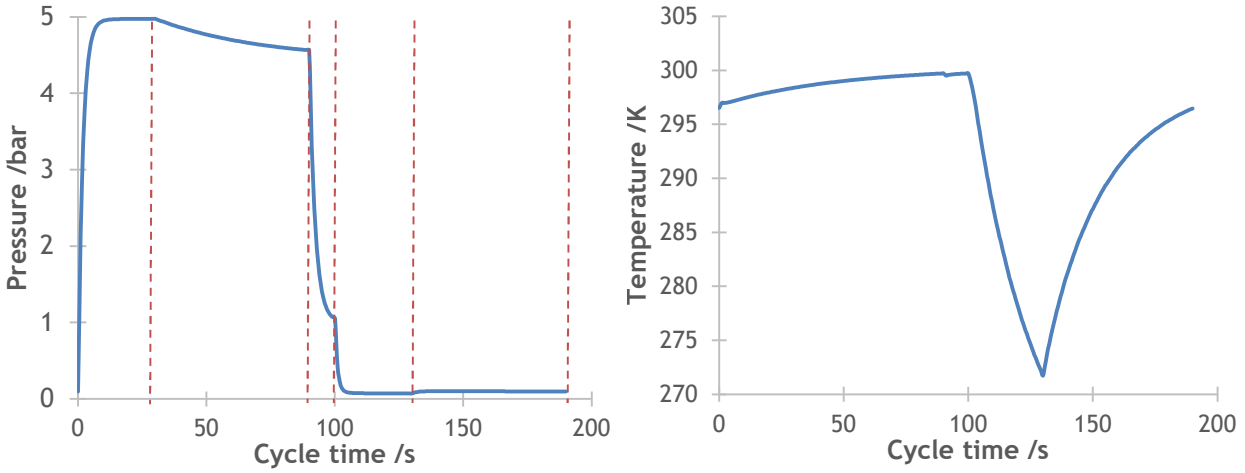

Figure 30 - Temperature and pressure history on the top of the bed for Mg-Clinoptilolite at CSS.

Gas temperature variation on the top of the column during this cycle is higher than for the Purified Clinoptilolite. Yet, the temperature history on the top of the column, presented in Figure 30, does not fairly represent the bed temperature profile, as seen in Figure 31.

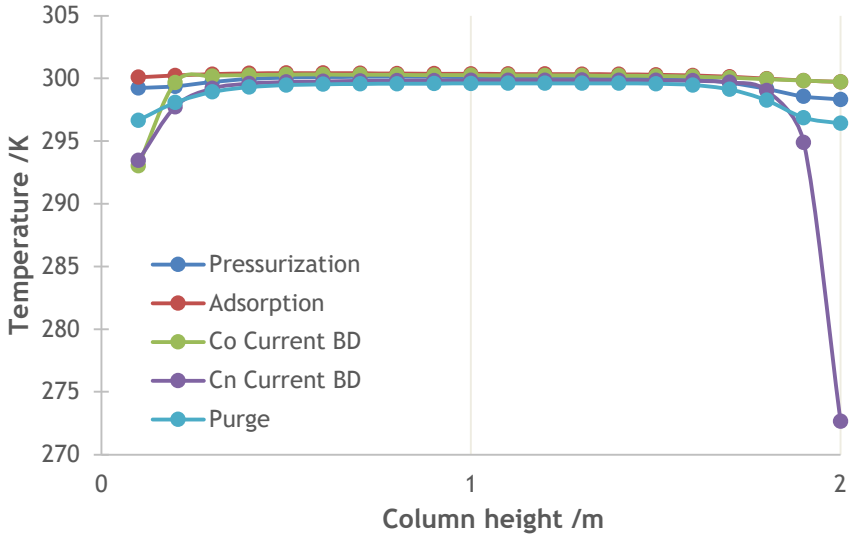

Figure 31 - Temperature profile along column height, for run 49 in Mg-Clinoptilolite.

A more evident difference in the solid phase loading for nitrogen and methane is depicted in Figure 32, where the adsorbed amount of methane is kept constant for each step. At the same time, there is some variation in the solid phase concentration between steps for nitrogen. This is due to the higher mass transfer resistances felt for methane in the solid.

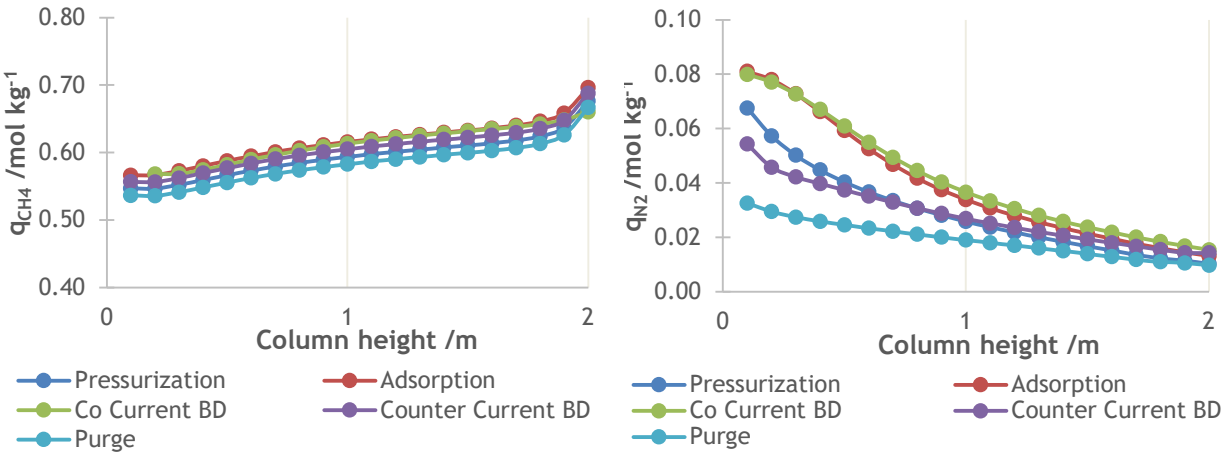

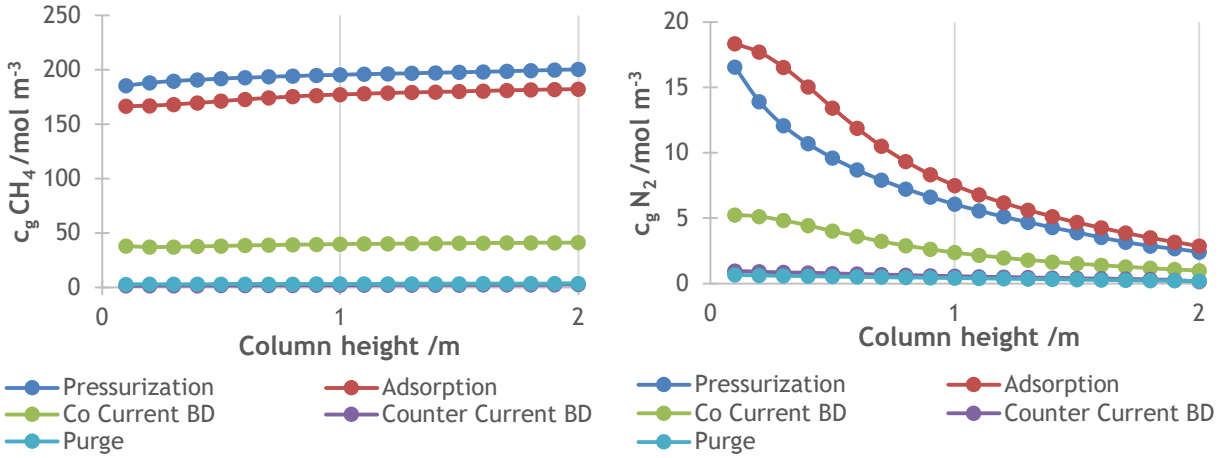

Figure 32 - Solid and gas phase concentration profile of both components in Mg-Clinoptilolite, at the end of each step, for run 49.

Sensitivity study for Mg-Clinoptilolite

Even though the used parameters for this study comparison were obtained from the optimization of the Purified Clinoptilolite, a sensitivity analysis was also performed for the Mg-Clinoptilolite.

Table 11 - Sensitivity study for Mg-Clinoptilolite.

Run	u (m s^{-1})	*L/D*	*P/F*	P_{High} (bar)	P_{Co} (bar)	P_{Low} (bar)	L (m)	Purity	Recovery
32	0.07	2.86	0.1	5	1	0.1	2	98.38 %	75.97 %
33	0.17	10	0.1	5	1	0.1	4.6	97.86 %	76.46 %
34	0.11	5	0.1	5	1	0.1	2.9	98.57 %	66.11 %
35	0.07	2.86	0.2	5	1	0.1	2	98.70 %	74.19 %
36	0.07	2.86	0.3	5	1	0.1	2	98.81 %	66.29 %
37	0.07	2.86	0.1	5	1	0.1	2	98.35 %	76.07 %
39	0.07	2.86	0.1	5	1	0.3	2	92.93 %	82.04 %
40	0.07	2.86	0.1	5	1	0.5	2	93.09 %	87.40 %
41	0.07	2.86	0.1	8	1	0.1	2	**97.87 %**	**84.92 %**
42	0.07	2.86	0.1	3	1	0.1	2	98.03 %	71.11 %
43	0.07	2.86	0.1	5	2	0.1	2	97.93 %	57.76 %
44	0.07	2.86	0.1	5	3	0.1	2	98.30 %	48.13 %

Results for the sensitivity analysis of the Mg-Clinoptilolite adsorbent show that the best purity and recovery relation is for when the high pressure is 8 bar, achieving a product 97.87 % purity and 84.92 % of methane recovery. More information for this simulation can be found in the Appendix G.

4.2.3 Time step optimization

Following the sensitivity analysis performed for the independent parameters of the process for Purified Clinoptilolite, a cycle time and step time optimization was also developed.

Table 12 - Time step variation and its influence in purity and recovery for Purified Clinoptilolite.

Run	Press (s)	Ads (s)	CoBD (s)	CnBD (s)	Purge (s)	Purity	Recovery
25	30	60	10	30	60	96.66 %	58.34 %
22	20	60	10	30	60	96.42 %	48.21 %
26	30	60	10	30	50	96.94 %	52.59 %
27	30	60	10	30	40	96.71 %	62.10 %
28	30	70	10	30	60	97.05 %	56.20 %
29	30	80	10	30	60	97.02 %	55.71 %
30	30	60	10	40	60	97.38 %	50.34 %
47	30	50	10	30	40	**96.76 %**	**66.38 %**

From the obtained results, it was possible to conclude that the optimized cycle time for the separation with Purified Clinoptilolite was 160 s, reaching a methane purity of 96.76 % and recovery of 66.38 %.

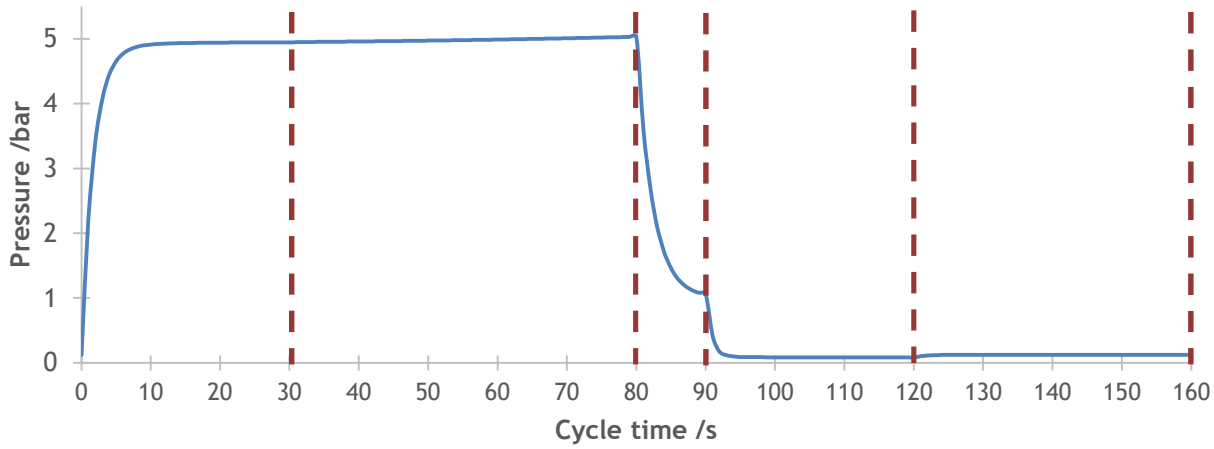

Figure 33 - Pressure history of run 47, for the optimized cycle time in Purified Clinoptilolite.

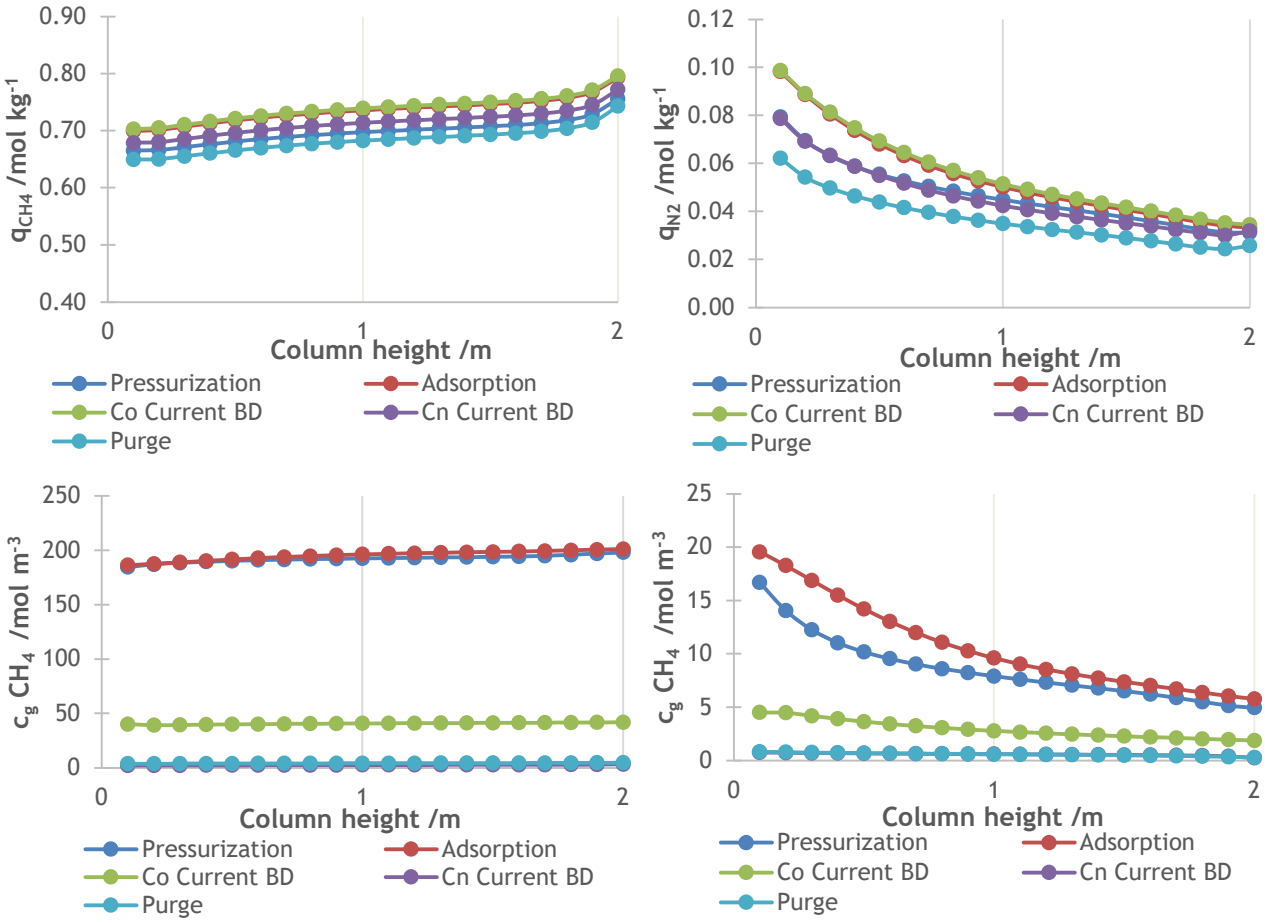

Figure 34 - Solid and gas phase concentration profile of both components In Purified Clinoptilolite, at the end of each step, for run 47.

The same cycle time and step configuration was tested for the other adsorbent, Mg-Clinoptilolite, for the same parameter configuration as the ones considered in Purified Clinoptilolite.

Table 13 - Optimized time step for Mg-Clinoptilolite.

Run	Press (s)	Ads (s)	CoBD (s)	CnBD (s)	Purge (s)	Purity	Recovery
48	30	50	10	30	40	**97.94 %**	**77.89 %**

As the reached product purity was 98 % for Mg-Clinoptilolite, the simulation purge "target" inlet composition was re-adjusted to a 98 %/ 2 % CH_4/N_2 gas mixture. As a result, a much higher methane recovery was obtained, which is a consequence of the lower methane adsorbed amount in this adsorbent.

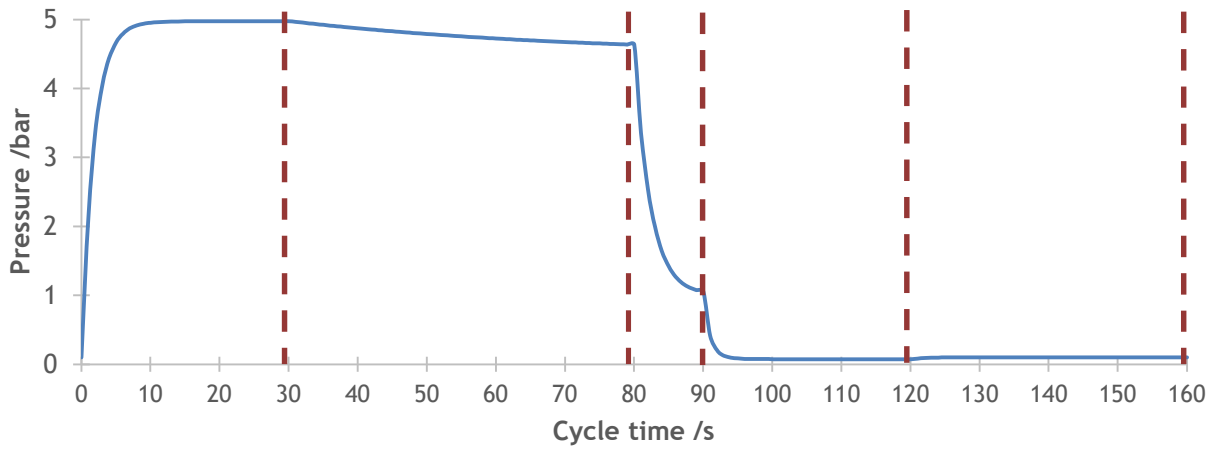

Figure 35 - Pressure history of run 48, for the optimized cycle time in Mg-Clinoptilolite.

Results indicate that the greater diffusivity ratio observed por Mg-Clinoptilolite, together with its lower methane capacity than Purified Clinoptilolite, lends it better performance values for this separation.

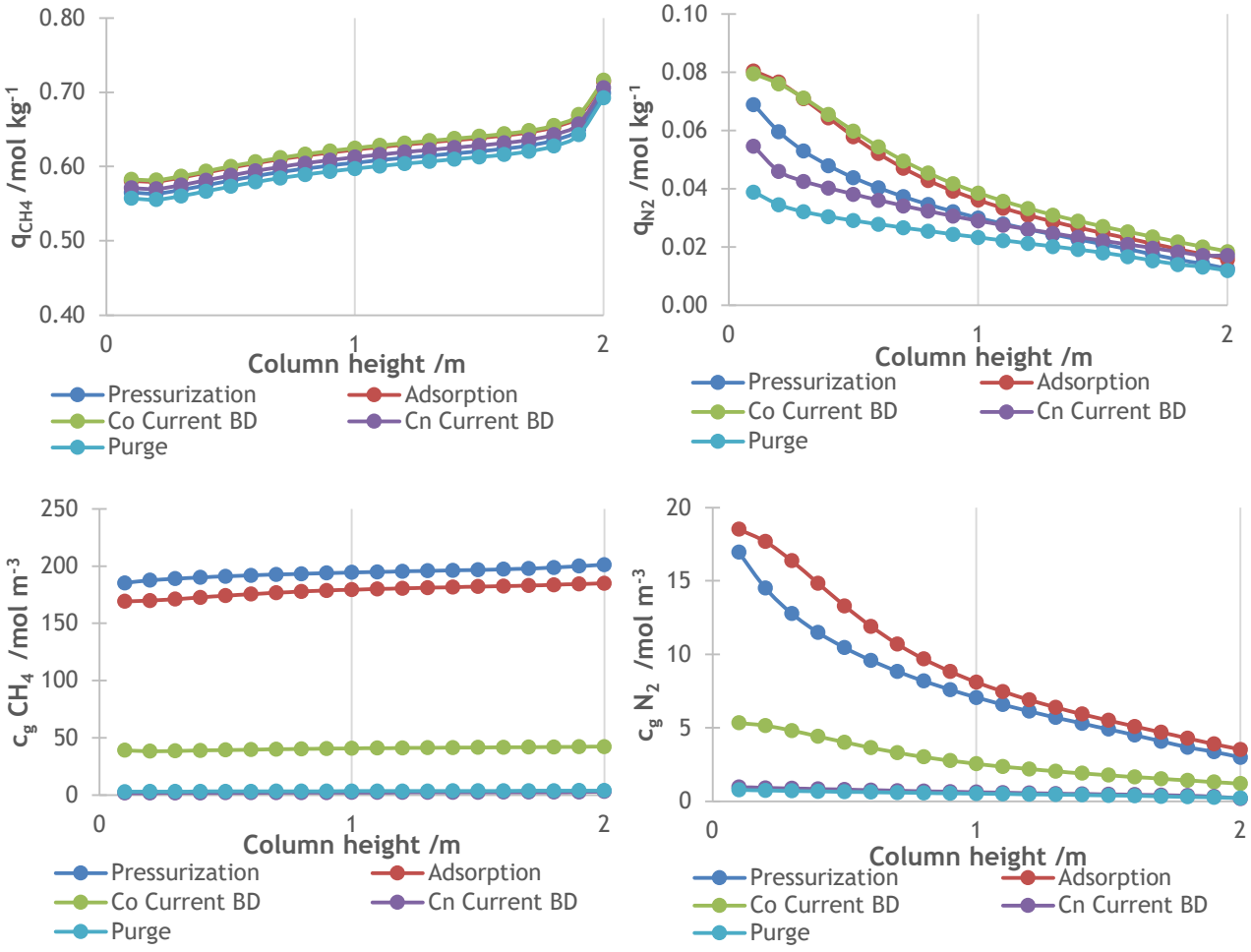

Figure 36 - Solid and gas phase concentration profile of both components In Mg-Clinoptilolite, at the end of each step, for run 48.

4.3 PSA scheduling

Although only one column was simulated, PSA is a multi-bed interactive system, so bed interactions must be carefully controlled.

A 2-bed 5-step PSA was considered for this project, based on the optimized cycle step and process parameters obtained previously.

The cycle steps are defined as (I) Feed Pressurization; (II) Adsorption; (III) Co current Blowdown; (IV) Counter current Blowdown; and (V) Low Pressure Purge. Each square represents 10 s of the cycle.

Bed 1	I	I	I	II	II	II	II	II	III	IV	IV	IV	V	V	V	V
Bed 2	III	IV	IV	IV	V	V	V	V	I	I	I	II	II	II	II	II

Figure 37 - 2 bed scheduling for the 5-step PSA.

The scheduling configuration was assembled considering that the two beds cannot be having a feed step simultaneously, and that the purge step is coupled with the adsorption step of the other column.

4.3.1 PSA Productivity and Energy consumption

There are other relevant PSA performance indicators that must be calculated, such as the system productivity and the energy required for the regeneration of the bed. [28,35]

Productivity was calculated for a 2-bed PSA, so two identical production steps were assumed, to obtain the performance indicator of the PSA system.

$$Productivity\ (mol_{CH4}\ kg_{ads}{}^{-1}\ h^{-1}) = \frac{(CH_4\ from\ step\ II + CH_4\ from\ step\ III - CH_4\ from\ step\ V)}{Total\ Cycle\ Time\ \cdot\ Adsorbent\ Mass} \quad 4.3$$

$$Energy\ (kJ\ mol_{CH4}{}^{-1}) = \frac{\int_0^t \left(\frac{\gamma}{\gamma-1}\right) R\ T \left[\left(\frac{P_{High}}{P_{Low}}\right)^{\frac{\gamma-1}{\gamma}} - 1\right] \frac{1}{\delta}\ \dot{n}(t)\ dt}{(CH_4\ from\ step\ II + CH_4\ from\ step\ III)} \quad 4.4$$

where γ is the isentropic constant (equal to 1.5 for ideal gas [36]), P_{High} and P_{Low} are the starting and ending pressures in the step, respectively, δ is the vacuum pump/compressor efficiency (assumed 85 %), and $\dot{n}(t)$ is the molar flowrate leaving the bed at time t.

Energy consumption was determined for both co-current blowdown (from 5 bar to 1 bar) and counter-current blowdown steps (from 1 bar to 0.1 bar), being the one presented in the Table 14 the total energy required for the depressurization in one cycle. Although equation 4.4 accounts for the fact that pressures may vary with time in a PSA process, in this calculation P_{High} and P_{Low} were considered constant.

Table 14 - VPSA performance indicators.

Run	Adsorbent	Purity	Recovery	Productivity (mol_{CH4} kg_{ads}^{-1} h^{-1})	Energy (kJ mol_{CH4}^{-1})
47	Purified Clinoptilolite	96.76 %	66.38 %	3.37	57.36
48	Mg-Clinoptilolite	97.94 %	77.89 %	3.78	41.95

Productivity values found in literature, for the same adsorbent and similar operation conditions, range 3.56 to 7.59 mol_{CH4} kg_{ads}^{-1} h^{-1} for Purified Clinoptilolite, and 4.69 to 7.13 mol_{CH4} kg_{ads}^{-1} h^{-1} for Mg-Clinoptilolite. [28,37] Therefore, productivity values obtained in this work are under the expected magnitude.

Overall, Mg-Clinoptilolite presented better performance results for the separation of nitrogen from methane.

5 Conclusion

The simulation of a 5-step VPSA to separate a 100 $m^3 h^{-1}$ gas mixture of 90 %/10 % CH_4 and N_2 was performed in this work, using the programme *Aspen Adsorption*. The model was based on a kinetically controlled separation, and the performance of Purified Clinoptilolite and Magnesium Clinoptilolite adsorbents was studied and optimized by enhancing the product purity and recovery to meet the standards for gas grid injection (a gas stream with a methane purity higher than 97 %).

The mathematical model indicates that, at cyclic steady-state conditions, an optimized cycle of 160 s with the five steps of feed pressurization at 5 bar and 300 K, adsorption at 5 bar, co-current blowdown until 1 bar, counter-current blowdown reaching 0.1 bar, and constant low-pressure purge with product stream, can achieve the targeted methane purity in both adsorbents chosen for this investigation. The column dimensions for the optimized results were of 2 m height and 70 cm of diameter, which fits the standard dimensions used by the company for other similar projects.

The adsorbents' choice was based on the nitrogen rejection method, which means that the major component and desired product, methane, can be collected on the top of the column as the light product. This has its advantages since it reduces the work needed to pressurize CH_4 back to pipeline pressure. For the cycle configuration studied in this work, the outlet flow from the co-current blowdown step is also considered a product because there is high methane content in this stream. Doing so, also enhances product recovery. However, this co-current blowdown step releases methane at low pressure of 1 bar, so it is important to note that part of the methane-rich product needs to be repressurized for combining with high-pressure product, leading to additional compression energy consumption. Even though, having a nitrogen selective adsorbent is still more intuitive with the set gas mixture composition, since it is the minor component, and it is the one that needs to be removed.

From data reported for the commercially available adsorbents, cation exchanged clinoptilolite with magnesium presented the higher overall kinetic selectivity amongst the non-patented materials. Furthermore, Purified Clinoptilolite also showed great nitrogen kinetic selective values, and its performance was examined here as well. The main constraint in using clinoptilolite adsorbents is based on the fact that these materials present different cation structures and compositions depending on the mineral source location. However, the process of purification and cation exchange might overcome this struggle, being these procedures well described and can be found in literature.

Although these adsorbents present equilibrium selectivity to methane, this component and nitrogen were reported to show high diffusion constant discrepancy, favorable to the adsorption of nitrogen, which enabled the kinetically controlled separation. Kinetic limitations of methane were explicit by evaluating the mixture breakthrough curves, and resistance in micropore was believed to be the main reason for this.

The strategy followed for the simulation was the design of a single adsorption bed. This has some limitations in what concerns the fair representation of the transient state, since PSA unit works with at least two interconnected columns. For this project, only one of the PSA columns was simulated. Therefore, the purge inlet was fixed with the targeted product purity, which can symbolize a fraction of the product obtained being used. So, this approach will predict cyclic steady state (CSS) behaviour correctly but will have some limitation to predict the transient behavior.

The results obtained for the optimized PSA cycle were a product stream with 96.76 % methane purity and 66.38 % methane recovery when using the Purified Clinoptilolite, and 97.94 % purity with 77.89 % recovery when using Mg-Clinoptilolite. The initial set methane purity goal was achieved; however, product recovery is still far from the 96 % required by the company.

Higher recovery could possibly be accomplished if the waste stream obtained from this simulated system is further compressed and send to another independent PSA unit. This configuration is designed as Dual-PSA. The second PSA unit product should be optimized to match the feed composition of the first PSA. By doing so, methane recovery can be enhanced, as already stated in the literature. [37]

6 Assessment of the work done

6.1 Objectives Achieved

The main objectives achieved with this work were:

1. the selection of an adequate adsorbent material to perform the separation;
2. understanding and familiarization of the *Aspen Adsorption* programme;
3. development of a single-bed design for the separation unit in *Aspen Adsorption*;
4. simulation of a kinetically controlled separation process;
5. the progressive optimization based on the sensitivity analysis that enabled to attained results of methane purity ≥ 97 %.

6.2 Limitations and Future Work

The dependence on the experimental literature data is one of the limitations of this work since the lack of detailed description and information led to some model assumptions and considerations that might not be well defined for the actual process situation. It would be beneficial to have a laboratory scale installation to assess the adsorbent's equilibrium and kinetics, so that results could be more reliable.

Although recovery values did not match the goal demanded by the company (higher than 96 %), its enhancement can be achieved by adding another PSA unit to the system. Future work on this topic must rely on the simulation and optimization of this new PSA unit independently so that it is possible to evaluate the overall system performance.

6.3 Final Assessment

The work done provided an insight into the current options for nitrogen removal from biogas and its challenges. To simulate a kinetically controlled separation by an adsorbent which is thermodynamically selective to methane is not an easy task. This is supported by the not so widely available literature on this topic for the specific case of nitrogen and methane separation. So, this work can be seen as a solid contribution to developing a more efficient kinetically controlled separation of nitrogen and methane.

7 References

[1] P. IEA, *IEA (2020), World Energy Balances: Overview*, 2020. https://www.iea.org/reports/world-energy-balances-overview (accessed Jun. 16, 2021).

[2] J. Langerak, R. Lems, and E. H. M. Dirkse, "Full-Scale Biogas Upgrading," *Air Pollution Prevention and Control*. pp. 525–544, Apr. 19, 2013, doi: https://doi.org/10.1002/9781118523360.ch23.

[3] Rufford, T. E., Smart, S., Watson, G. C. Y., Graham, B. F., Boxall, J., Diniz da Costa, J. C., & May, E. F. (2012). The removal of CO 2 and N 2 from natural gas: A review of conventional and emerging process technologies. *Journal of Petroleum Science and Engineering*, *94–95*, 123–154. https://doi.org/10.1016/j.petrol.2012.06.016.

[4] O. W. Awe, Y. Zhao, A. Nzihou, D. P. Minh, and N. Lyczko, "A Review of Biogas Utilisation, Purification and Upgrading Technologies," *Waste and Biomass Valorization*, vol. 8, no. 2, pp. 267–283, 2017, doi: 10.1007/s12649-016-9826-4.

[5] F. Brandani, P. Pullumbi, and C. Monereau, "Nitrogen rejection from landfill gas using Pressure Swing Adsorption," *Adsorption*, no. February, 2021, doi: 10.1007/s10450-021-00304-0.

[6] Angelidaki, I., Treu, L., Tsapekos, P., Luo, G., Campanaro, S., Wenzel, H., & Kougias, P. G. (2018). Biogas upgrading and utilization: Current status and perspectives. Biotechnology Advances, 36(2), 452–466. https://doi.org/10.1016/j.biotechadv.2018.01.011.

[7] IEA, "Outlook for biogas and biomethane. Prospects for organic growth. World Energy Outlook Special Report.," p. 93, 2020.

[8] S. U. Nandanwar, D. R. Corbin, and M. B. Shiflett, "A Review of Porous Adsorbents for the Separation of Nitrogen from Natural Gas," *Ind. Eng. Chem. Res.*, vol. 59, no. 30, pp. 13355–13369, Jul. 2020, doi: 10.1021/acs.iecr.0c02730.

[9] J. A. C. Silva, A. Ferreira, P. A. P. Mendes, A. F. Cunha, K. Gleichmann, and A. E. Rodrigues, "Adsorption Equilibrium and Dynamics of Fixed Bed Adsorption of CH4/N2 in Binderless Beads of 5A Zeolite," *Ind. Eng. Chem. Res.*, vol. 54, no. 24, pp. 6390–6399, 2015, doi: 10.1021/acs.iecr.5b01608.

[10] S. Effendy, C. Xu, and S. Farooq, "Optimization of a pressure swing adsorption process for nitrogen rejection from natural gas," *Ind. Eng. Chem. Res.*, vol. 56, no. 18, pp. 5417–5431, 2017, doi: 10.1021/acs.iecr.7b00513.

[11] C. A. Grande, "Advances in Pressure Swing Adsorption for Gas Separation," *ISRN Chem. Eng.*, vol. 2012, pp. 1–13, 2012, doi: 10.5402/2012/982934.

[12] K. R. Wood, Y. A. Liu, and Y. Yu, "Design, Simulation and Optimization of Adsorptive and Chromatographic Separations," *Des. Simul. Optim. Adsorpt. Chromatogr. Sep.*, 2018, doi: 10.1002/9783527815029.

[13] R. P. Marathe, K. Mantri, M. P. Srinivasan, and S. Farooq, "Effect of ion exchange and dehydration temperature on the adsorption and diffusion of gases in ETS-4," *Ind. Eng. Chem. Res.*, vol. 43, no. 17, pp. 5281–5290, 2004, doi: 10.1021/ie049818+.

[14] X. Wu, B. Yuan, Z. Bao, and S. Deng, "Adsorption of carbon dioxide, methane and nitrogen on an ultramicroporous copper metal–organic framework," *J. Colloid Interface Sci.*, vol. 430, pp. 78–84, 2014, doi: https://doi.org/10.1016/j.jcis.2014.05.021.

[15] R. Yang, *Gas Separation by Adsorption Processes*, vol. 43, no. 4. 1988.

[16] A. M. M. Mendes, "Adsorção com modulação da pressão: Aplicação à separação do Oxigénio do Ar.", Ph.D Thesis, University of Porto, 1993.

[17] C. W. Skarstrom, "Method and apparatus for fractionating gaseous mixtures by adsorption", patent nr 2944627, July 1960.

[18] S. J. Bhadra, "Methane-Nitrogen Separation By Pressure Swing Adsorption Methane-Nitrogen Separation By Pressure Swing Adsorption," p. 149, 2007.

[19] A. D. Ebner, A. Mehrotra, and J. A. Ritter, "Graphical approach for complex PSA cycle scheduling," *Adsorption*, vol. 15, no. 4, pp. 406–421, 2009, doi: 10.1007/s10450-009-9188-3.

[20] D. D. Do, *Fundamentals of Diffusion and Adsorption in Porous Media*, vol. 2. 1998.

[21] S. Cavenati, C. A. Grande, and A. E. Rodrigues, "Separation of methane and nitrogen by adsorption on carbon molecular sieve," *Sep. Sci. Technol.*, vol. 40, no. 13, pp. 2721–2743, 2005, doi: 10.1080/01496390500287846.

[22] S. Effendy, C. Xu, and S. Farooq, "Optimization of a Pressure Swing Adsorption Process for Nitrogen Rejection from Natural Gas," *Ind. Eng. Chem. Res.*, vol. 56, no. 18, pp. 5417–5431, May 2017, doi: 10.1021/acs.iecr.7b00513.

[23] G. Xiao, Z. Li, T. L. Saleman, and E. F. May, "Adsorption equilibria and kinetics of CH4 and N2 on commercial zeolites and carbons," *Adsorption*, vol. 23, no. 1, pp. 131–147, 2017, doi: 10.1007/s10450-016-9840-7.

[24] M. W. Ackley and R. T. Yang, "Diffusion in ion-exchanged clinoptilolites," *AIChE J.*, vol. 37, no. 11, pp. 1645–1656, Nov. 1991, doi: https://doi.org/10.1002/aic.690371107.

[25] D. Kennedy, M. Khanafer, and F. H. Tezel, "The effect of Ag+ cations on the micropore properties of clinoptilolite and related adsorption separation of CH4 and N2 gases," *Microporous Mesoporous Mater.*, vol. 281, Mar. 2019, doi: 10.1016/j.micromeso.2019.03.007.

[26] D. A. Kennedy, M. Mujcin, E. Trudeau, and F. H. Tezel, "Pure and Binary Adsorption Equilibria of Methane and Nitrogen on Activated Carbons, Desiccants, and Zeolites at Different Pressures," *J. Chem. Eng. Data*, vol. 61, no. 9, pp. 3163–3176, 2016, doi: 10.1021/acs.jced.6b00245.

[27] D. A. Kennedy and F. H. Tezel, "Cation exchange modification of clinoptilolite – Screening analysis for potential equilibrium and kinetic adsorption separations involving methane, nitrogen, and carbon dioxide," *Microporous Mesoporous Mater.*, vol. 262, no. December 2017, pp. 235–250, 2018, doi: 10.1016/j.micromeso.2017.11.054.

[28] A. Jayaraman, A. J. Hernandez-Maldonado, R. T. Yang, D. Chinn, C. L. Munson, and D. H. Mohr, "Clinoptilolites for nitrogen/methane separation," *Chem. Eng. Sci.*, vol. 59, no. 12, pp. 2407–2417, 2004, doi: https://doi.org/10.1016/j.ces.2003.10.030.

[29] R. Weh, G. Xiao, M. A. Islam, and E. F. May, "Nitrogen Rejection by Dual Reflux Pressure Swing Adsorption Using Engelhard Titanosilicate Type 4," *Ind. Eng. Chem. Res.*, vol. 59, no. 52, pp. 22573–22581, 2020, doi: 10.1021/acs.iecr.0c03768.

[30] Yoon, J. W., Chang, H., Lee, S. J., Hwang, Y. K., Hong, D. Y., Lee, S. K., Lee, J. S., Jang, S., Yoon, T. U., Kwac, K., Jung, Y., Pillai, R. S., Faucher, F., Vimont, A., Daturi, M., Férey, G., Serre, C., Maurin, G., Bae, Y. S., & Chang, J. S. (2017). Selective nitrogen capture by porous hybrid materials containing accessible transition metal ion sites. *Nature Materials*, *16*(5), 526–531. https://doi.org/10.1038/nmat4825.

[31] Pillai, R. S., Yoon, J. W., Lee, S. J., Hwang, Y. K., Bae, Y. S., Chang, J. S., & Maurin, G. (2017). N2 Capture Performances of the Hybrid Porous MIL-101(Cr): From Prediction toward Experimental Testing. *Journal of Physical Chemistry C*, *121*(40), 22130–22138. https://doi.org/10.1021/acs.jpcc.7b07029.

[32] M. W. Ackleyt and R. T. Yang, "Adsorption Characteristics of High-Exchange Clinoptilolites," pp. 2523–2530, 1991.

[33] J. A. Ritter and R. T. Yang, "Equilibrium Adsorption of Multicomponent Gas Mixtures at Elevated Pressures," *Ind. Eng. Chem. Res.*, vol. 26, no. 8, pp. 1679–1686, 1987, doi: 10.1021/ie00068a032.

[34] A. Findikakis, "Heat Capacity Analysis Report," no. November, 2004, [Online]. Available: http://www.osti.gov/energycitations/product.biblio.jsp?osti_id=838658.

[35] L. Erden, A. D. Ebner, and J. A. Ritter, "Separation of Landfill Gas CH4 from N2 Using Pressure Vacuum Swing Adsorption Cycles with Heavy Reflux," *Energy and Fuels*, vol. 32, no. 3, pp. 3488–3498, 2018, doi: 10.1021/acs.energyfuels.7b03534.

[36] B. Wu, X. Zhang, Y. Xu, D. Bao, and S. Zhang, "Assessment of the energy consumption of the biogas upgrading process with pressure swing adsorption using novel adsorbents," *J. Clean. Prod.*, vol. 101, pp. 251–261, 2015, doi: 10.1016/j.jclepro.2015.03.082.

[37] A. Jayaraman and R. Yang, "Tailored Clinoptilolites for Nitrogen/Methane Separation," *Ind. Eng. Chem. Res. - IND ENG CHEM RES*, vol. 44, Feb. 2005, doi: 10.1021/ie0492855.

Annex A Pipeline Specifications by country

Pipeline specifications are not the same for every country. A brief comparison is described below.

Table A 1 - List of pipeline specification for each country

	The Netherlands [1]	Sweden [1]	Switzerland [1]	United States Oregon [2]
Methane	> 84 %	95 - 99 %	> 96 %	
Ethane + Propane	< 2 %			
Nitrogen	< 14 %	< 5 %		< 2.75 %
Oxygen	< 0.5 %		< 0.5 %	
Carbon Dioxide	0 mg m^3		< 6 %	2 %
Inorganic Sulphur	< 5 mg m^3	< 23 mg m^3	< 30 mg m^3	
Organic Sulphur	< 10 mg m^3			
Higher hydrocarbons	< 25 mg m^3			
Ammonia	< 3 mg m^3			
Wobbe Index	43.46 - 44.41 MJ m^3	44.7 - 46.4 MJ m^3	47.9 - 56.5 MJ m^3	47.6 - 51.6 MJ m^3

[1] ALTENER PROJECT: Regulation Draft of Biogas Commercialization in Gas Grid – BIOCOMM Technical requirements report, BIOCOMM Project: 4.1030/C/02-082/2002, A Report by Svenskt Gasteknisk Center (SGC), Sweden

[2] World, B., Biomethane Market Intelligence Report. 2

Annex B Biogas composition

Biogas composition vary from source to source. The table below shows the typical biogas composition of sources such as sewage sludge, manure, agro-industrial bio-waste and also from the landfill sites.

Table B 1 – Typical biogas composition by source.

	Sewage sludge, manure, agro-industrial bio-waste	Lanfill sites
Methane	55 - 70 %	35 - 65 %
Carbon Dioxide	30 - 45 %	15 - 40%
Nitrogen	0 - 15 %	5 - 40 %
Oxygen	0 - 3 %	0 - 5 %
Water	1 - 5 %	1 - 5 %
Hydrogen		0 - 3 %
Carbon Monoxide		0 - 3 %

[1] O. W. Awe, Y. Zhao, A. Nzihou, D. P. Minh, and N. Lyczko, “A Review of Biogas Utilisation, Purification and Upgrading Technologies,” Waste and Biomass Valorization, vol. 8, no. 2, pp. 267–283, 2017, doi: 10.1007/s12649-016-9826-4.

Annex C Physical properties of methane and nitrogen

The similar physical characteristics of methane and nitrogen molecules are presented in Table C 1.

Table C 1 - Physical properties of methane and nitrogen.

	CH4	N2
Kinetic Diameter (Å)	3.80	3.64
Normal boiling point (K)	111.7	77.3
Critical temperature (K)	190.55	126.2
Critical pressure (kPa)	4600	3400
ΔHvap (kJ/mol)	8.17	5.58
Polarisability (Å ^{3})	2.448	1.71
Quadrapole moment (DÅ)	0.02	1.54

[1] T. E. Rufford et al., "The removal of CO 2 and N 2 from natural gas: A review of conventional and emerging process technologies," J. Pet. Sci. Eng., vol. 94–95, pp. 123–154, 2012, doi: 10.1016/j.petrol.2012.06.016.

Annex D Adsorbent description

The detailed preparation of adsorbents can be consulted in Jayaraman et al. (2004):

"The raw clinoptilolite was crushed to 140 mesh, heated in deionized water (80 mL deionized water for 1 g of clinoptilolite) to remove soluble salts and dispersed in methyl iodide solution to remove heavy impurities. The purified clinoptilolite was employed in subsequent ion exchanges. Ion exchanges were carried out with 0:2 M salt solutions in an autoclave at 134 ◦C and 3 atm pressure for 24 h. Five times the theoretical cation exchange capacity is used for monovalent cations and 10 times the cation exchange capacity is used for divalent cations. After ion exchange, the samples were washed repeatedly with deionized water to remove the excess salt. Ion-exchanged clinoptilolites were calcined at 100◦C for 24 h before adsorption studies."

The clinoptilolite samples obtained in the literature were examined using neutron activation analysis, to get to the composition of the present cations in the structure. Results are summarized in the table.

Table D 1 - Chemical composition of Purified Clinoptilolite and Mg-Clinoptilolite.

Sample	***Al***	***Mg***	***K***	***Na***	***Ca***	***Na/Mg***	***Si/Al***	***% ion exchange***
Purified Clinoptilolite	6	0.4	1.627	2.006	0.835	5.018	5	-
Magnesium clinoptilolite	6	1.762	1.148	0.592	0.46	0.336	5	58.736

[1] A. Jayaraman, A. J. Hernandez-Maldonado, R. T. Yang, D. Chinn, C. L. Munson, and D. H. Mohr, "Clinoptilolites for nitrogen/methane separation," *Chem. Eng. Sci.*, vol. 59, no. 12, pp. 2407–2417, 2004, doi: https://doi.org/10.1016/j.ces.2003.10.030

Appendix A Biogas upgrading technologies

Table AA 1 – Conventional biogas upgrading technologies comparison.

Technology	Cryogenic distillation	Membrane				Adsorption	Absorption	
		Rubbery polymer	Glassy polymer	Inorganic molecular sieve	Mixed matrix		Lean oil	Liquid ammonia
Separation parameter	volatility	partial pressure; molecular size; diffusivity				kinetic diameter; van der Walls forces	solubility	
Industry maturity	very high	high				high for nitrogen purification	low	
Selective component	CH4	CH4	N2	N2	Both	adsorbent dependent	CH4	N2
Advantages	large production	easily scalable, safe and energy efficient for nitrogen selective processes				low energy and capital investment costs	high CH4 recovery	reduced equipment size and small amount of solvent
Drawbacks	ennergy and cost intensive	low selectivity				low selectivity	energy intensive; large solvent circulation rate	energy intensive; low selectivity

[1] Li, Z. (2018). Separation of Nitrogen from Natural Gas: Conventional and Emerging Technologies. 10–21. https://api.research-repository.uwa.edu.au/portalfiles/portal/32927788/THESIS_DOCTOR_OF_PHILOSOPHY_LI_Zhikao_2018.pdf

Appendix B Reported PSA configurations for kinetically controlled separations

Table AB 1 – Cyclic configurations for kinetically controlled PSA systems.

Continuous feed cycle configuration	Cycle step sequence	Adsorbent	T (K)	P_H (bar)	P_L (bar)	y_feed (CH_4/N_2)	CH_4 Purity (%)	CH_4 Recovery (%)	Ref.
4-bed 5-step	F-CoD-CnD1-CnD2-FP	Purified Clinoptilolite	295	7.0	0.4	85/15	95.4	73.1	[1]
2-cycle 2-bed 5-step	F-CoD-CnD-LR-FP/ F-CoD-CnD-LR-FP	Purified Clinoptilolite	295	7.0	0.4	80/20	96.0	95.5	[2]
4-bed 5-step	F-CoD-CnD1-CnD2-FP	Mg-Clinoptilolite	295	7.0	0.4	85/15	93.3	41.6	[1]
2-cycle 2-bed 5-step	F-CoD-CnD-LR-FP/ F-CoD-CnD-LR-FP	Mg/Na clinoptilolite	295	7.0	0.4	80/20	96.0	93.7	[2]
2-bed 4-step	F-CnD-LR-FP	Ba-ETS-4	300	9.0	0.5	90/10	98.2	90.0	[3]
2-bed 6-step	FP-HPA-DPE-CnD-CnEv-PPE	CMS-T	amb	11.5	0.3	85/15	95.0	94.0	[4]

F Feed/Adsorption; CoD – Co current Desorption; CnD – Counter current Desorption; FP – Feed Pressurization; LR – Light Reflux; HPA – High Pressure Adsorption; DPE/PPE – Pressure Equalization; CnEV – Counter current Evacuation.

[1] A. Jayaraman, A. J. Hernandez-Maldonado, R. T. Yang, D. Chinn, C. L. Munson, and D. H. Mohr, "Clinoptilolites for nitrogen/methane separation," *Chem. Eng. Sci.*, vol. 59, no. 12, pp. 2407–2417, 2004, doi: https://doi.org/10.1016/j.ces.2003.10.030

[2] A. Jayaraman and R. Yang, "Tailored Clinoptilolites for Nitrogen/Methane Separation," *Ind. Eng. Chem. Res. - IND ENG CHEM RES*, vol. 44, Feb. 2005, doi: 10.1021/ie0492855.

[3] S. J. Bhadra and S. Farooq, "Separation of methane-nitrogen mixture by pressure swing adsorption for natural gas upgrading," *Ind. Eng. Chem. Res.*, vol. 50, no. 24, pp. 14030–14045, 2011, doi: 10.1021/ie201237x.

[4] S. Effendy, C. Xu, and S. Farooq, "Optimization of a pressure swing adsorption process for nitrogen rejection from natural gas," *Ind. Eng. Chem. Res.*, vol. 56, no. 18, pp. 5417–5431, 2017, doi: 10.1021/acs.iecr.7b00513.

Appendix C Promising adsorbents for N_2/ CH_4 separation

Table AC 1 - Screening of the suitable adsorbents for nitrogen and methane separation.

Equilibrium-based separation				
Type	***Name***	***a_eq (N2/CH4)***	***S (N_2/CH_4)***	***Suppliers***
Titanosilicate	Sr-ETS-4 (588K)	13.44		BASF
Clinoptilolite	Mg/Na (50/50) clinoptilolite	4.31		
MOFs	MIL 100 Cr (543K)	4	10	Strem Chemicals (at small scale customized production)
Clinoptilolite	Ag (0.2M) clinoptilolite	3.51	28.81	
Titanosilicate	Ba-ETS-4 (673K)	3.36		BASF
Titanosilicate	Sr-ETS-4 (543K)	2.1		BASF
MOFs	MIL 101 Cr (543K)		17.59	Strem Chemicals
Kinetic-based separation				
Type	***Name***	***D (N2/CH4)***	***β (N2/CH4)***	
Titanosilicate	Ba-ETS-4 (673K)	3733.33	205.3	BASF
Titanosilicate	Ba-ETS-4 (543K)	2692.31	18.68	BASF
Titanosilicate	Ba-ETS-4 (623K)	2650	28.83	BASF
Titanosilicate	Ba-ETS-4 (723K)	1105.26	48.21	BASF
Titanosilicate	Sr-ETS-4 (463K)	373.33	6.57	BASF
Clinoptilolite	Mg-Clinoptilolite	300	18.84	Steelhead Speciality Minerals

Carbon Molecular Sieves	CMS 3K	214.16	6.4	Takeda Corporation
Titanosilicate	Sr-ETS-4 (503K)	213.33	6.43	BASF
Carbon Molecular Sieves	CMS 3K	118.88	4.24	Takeda Corporation
Carbon Molecular Sieves	CMS 3K	118.88	4.24	Takeda Corporation
Clinoptilolite	Mg/Na (50/50) clinoptilolite	72.22	17	
Clinoptilolite	Purified Clinoptilolite	55	5.81	Steelhead Speciality Minerals
Clinoptilolite	Raw clinoptilolite	38.84	2.62	Ash Meadows Zeolite LLC
Titanosilicate	Sr-ETS-4 (543K)	31.54	11.79	BASF
Carbon Molecular Sieves	CMS 3K 172	20.04	2.03	Takeda Corporation
Titanosilicate	Sr-ETS-4 (583K)	19	4.79	BASF
Titanosilicate	Sr-ETS-4 (588K)	2.58	21.59	BASF

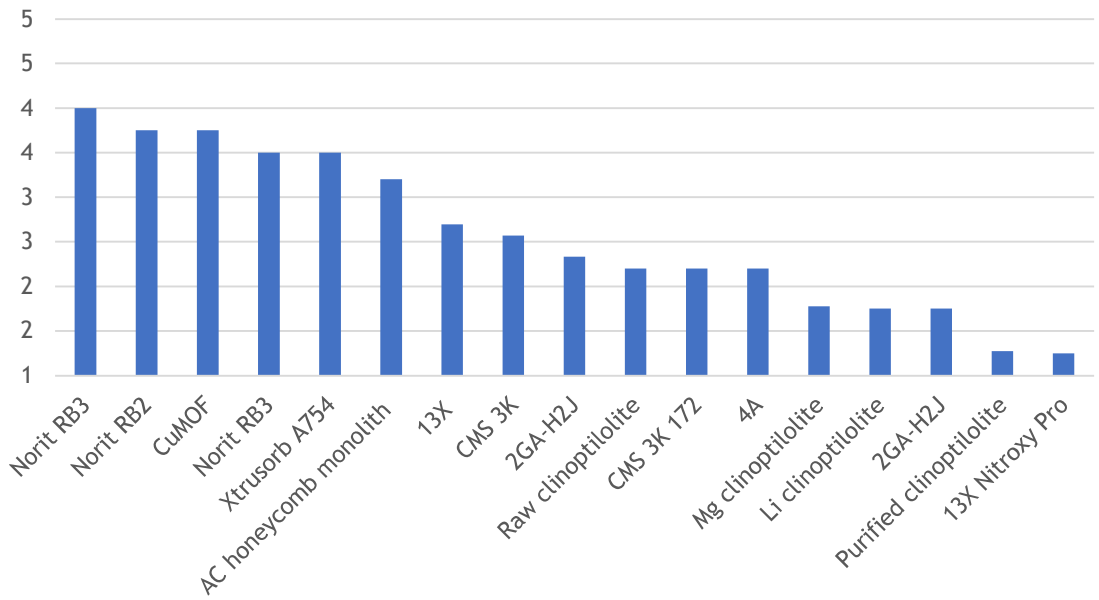

Figure AC 1 - Ideal selectivity (α_{ideal}) CH_4/N_2.

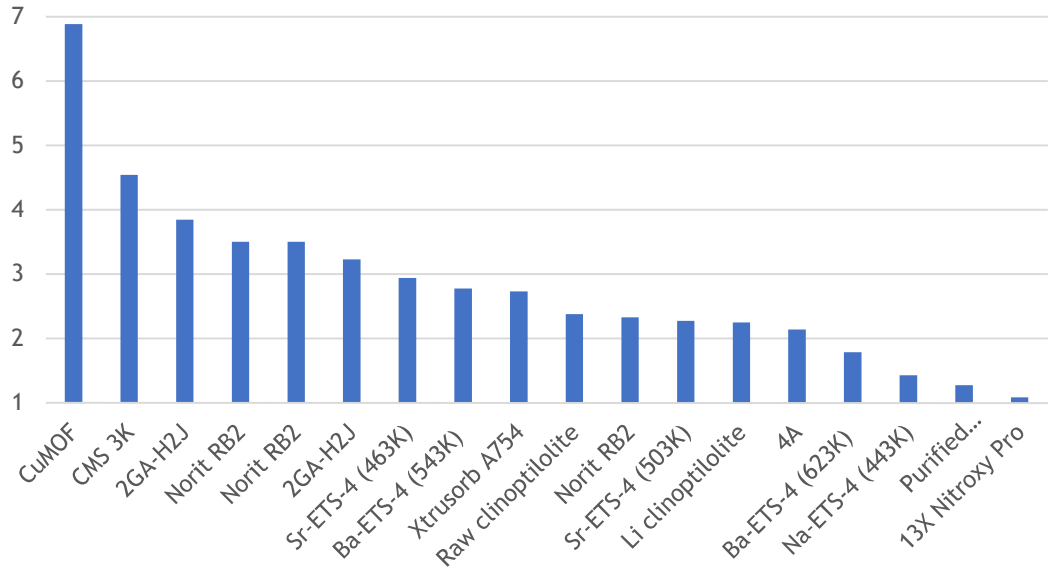

Figure AC 3 - Equilibrium selectivity (α_{eq}) CH_4/N_2.

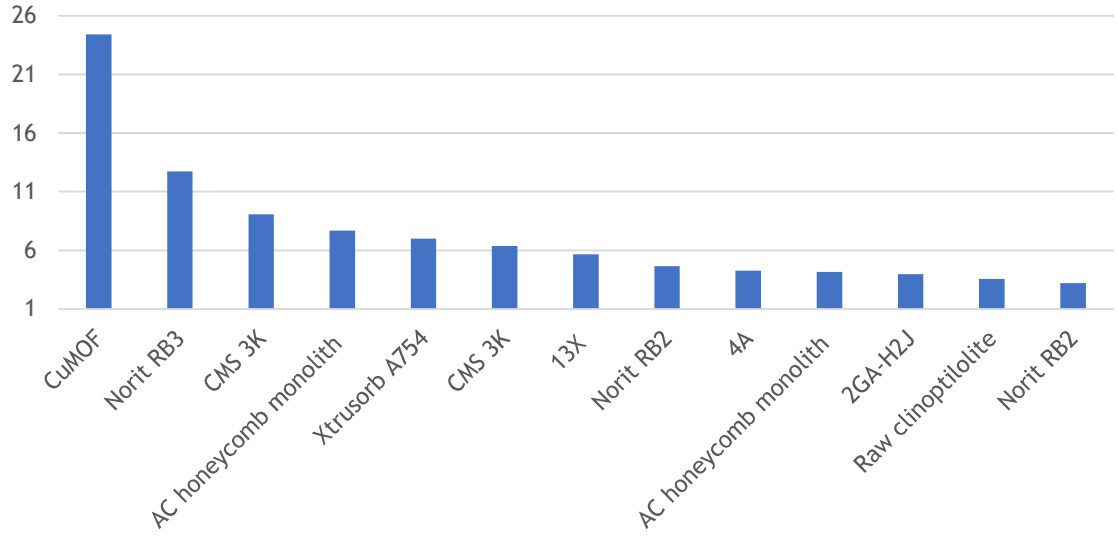

Figure AC 2 - Adsorbent separation factor (S) CH_4/N_2.

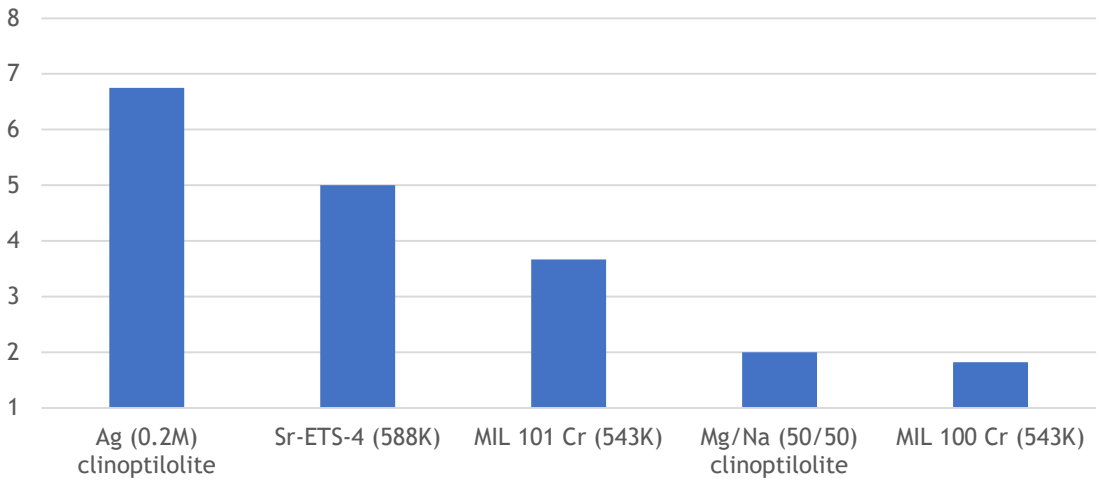

Figure AC 4 - Ideal selectivity (α_{ideal}) N_2/CH_4.

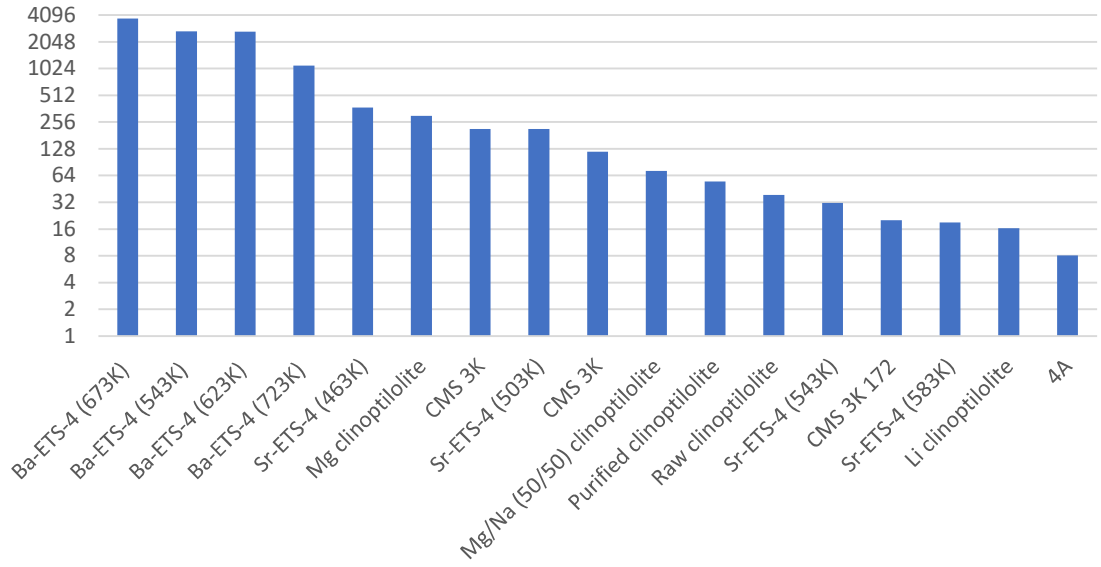

Figure AC 6 - Pure kinetic selectivity (D) N_2/CH_4.

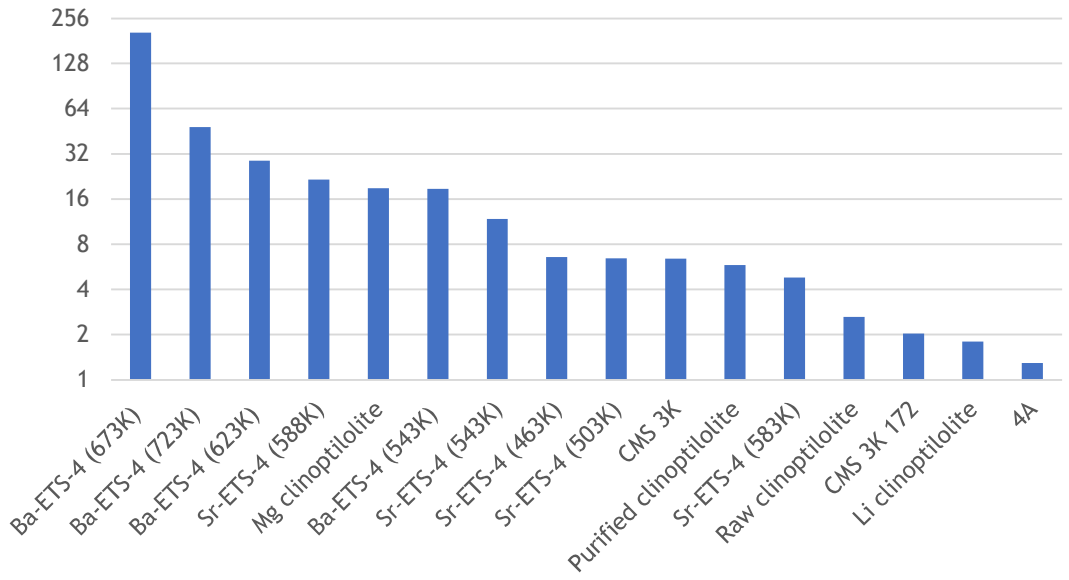

Figure AC 7 - Overall kinetic selectivity (β) N_2/CH_4.

[1] Brandani, F., Pullumbi, P., & Monereau, C. (2021). Nitrogen rejection from landfill gas using Pressure Swing Adsorption. Adsorption, February. https://doi.org/10.1007/s10450-021-00304-0

[2] Cavenati, S., Grande, C. A., & Rodrigues, A. E. (2005). Separation of methane and nitrogen by adsorption on carbon molecular sieve. Separation Science and Technology, 40(13), 2721–2743. https://doi.org/10.1080/01496390500287846

[3] Cavenati, S., Grande, C. A., Rodrigues, A. E., Kiener, C., & Müller, U. (2008). Metal Organic Framework Adsorbent for Biogas Upgrading. Industrial & Engineering Chemistry Research, 47(16), 6333–6335. https://doi.org/10.1021/ie8005269

[4] Do, D. D. (1998). Fundamentals of Diffusion and Adsorption in Porous Media (Vol. 2). https://doi.org/10.1142/9781860943829_0007

[5] Effendy, S., Xu, C., & Farooq, S. (2017). Optimization of a Pressure Swing Adsorption Process for Nitrogen Rejection from Natural Gas. Industrial & Engineering Chemistry Research, 56(18), 5417–5431. https://doi.org/10.1021/acs.iecr.7b00513

[6] Finsy, V., Ma, L., Alaerts, L., De Vos, D., Baron, G., & Denayer, J. (2009). Separation of CO2/CH4 mixtures with the MIL-53(Al) metal–organic framework. Microporous and Mesoporous Materials, 120, 221–227. https://doi.org/10.1016/j.micromeso.2008.11.007

[7] FRANKIEWICZ, T. C., & DONNELLY, R. G. (1983). Methane/Nitrogen Gas Separation over the Zeolite Clinoptilolite by the Selective Adsorption of Nitrogen. In Industrial Gas Separations (Vol. 223, pp. 11–213). AMERICAN CHEMICAL SOCIETY. https://doi.org/doi:10.1021/bk-1983-0223.ch011

[8] Grande, C. A., Cavenati, S., Da Silva, F. A., & Rodrigues, A. E. (2005). Carbon Molecular Sieves for Hydrocarbon Separations by Adsorption. Industrial & Engineering Chemistry Research, 44(18), 7218–7227. https://doi.org/10.1021/ie050376r

[9] Javani, R., Maghsoudi, H., Darvishi Gilan, S., & Majidpour, M. (2020). Study on adsorption performance of different adsorbents in nitrogen/methane separation. Separation Science and Technology (Philadelphia). https://doi.org/10.1080/01496395.2020.1842889

[10] Jayaraman, A., Hernandez-Maldonado, A. J., Yang, R. T., Chinn, D., Munson, C. L., & Mohr, D. H. (2004). Clinoptilolites for nitrogen/methane separation. Chemical Engineering Science, 59(12), 2407–2417. https://doi.org/https://doi.org/10.1016/j.ces.2003.10.030

[11] Kennedy, D. A., Mujcin, M., Trudeau, E., & Tezel, F. H. (2016). Pure and Binary Adsorption Equilibria of Methane and Nitrogen on Activated Carbons, Desiccants, and Zeolites at Different Pressures. Journal of Chemical and Engineering Data, 61(9), 3163–3176. https://doi.org/10.1021/acs.jced.6b00245

[12] Kennedy, D., Khanafer, M., & Tezel, F. H. (2019). The effect of Ag+ cations on the micropore properties of clinoptilolite and related adsorption separation of CH4 and N2 gases. Microporous and Mesoporous Materials, 281. https://doi.org/10.1016/j.micromeso.2019.03.007

[13] Majumdar, B., Bhadra, S. J., Marathe, R. P., & Farooq, S. (2011). Adsorption and diffusion of methane and nitrogen in barium exchanged ETS-4. Industrial and Engineering Chemistry Research, 50(5), 3021–3034. https://doi.org/10.1021/ie1014124

[14] Marathe, R. P., Mantri, K., Srinivasan, M. P., & Farooq, S. (2004). Effect of ion exchange and dehydration temperature on the adsorption and diffusion of gases in ETS-4. Industrial and Engineering Chemistry Research, 43(17), 5281–5290. https://doi.org/10.1021/ie049818+

[15] Nandanwar, S. U., Corbin, D. R., & Shiflett, M. B. (2020). A Review of Porous Adsorbents for the Separation of Nitrogen from Natural Gas. Industrial & Engineering Chemistry Research, 59(30), 13355–13369. https://doi.org/10.1021/acs.iecr.0c02730

[16] Pillai, R. S., Yoon, J. W., Lee, S. J., Hwang, Y. K., Bae, Y. S., Chang, J. S., & Maurin, G. (2017). N2 Capture Performances of the Hybrid Porous MIL-101(Cr): From Prediction toward Experimental Testing. Journal of Physical Chemistry C, 121(40), 22130–22138. https://doi.org/10.1021/acs.jpcc.7b07029

[17] Rufford, T. E., Smart, S., Watson, G. C. Y., Graham, B. F., Boxall, J., Diniz da Costa, J. C., & May, E. F. (2012). The removal of CO 2 and N 2 from natural gas: A review of conventional and emerging process technologies. Journal of Petroleum Science and Engineering, 94–95, 123–154. https://doi.org/10.1016/j.petrol.2012.06.016

[18] Tzabar, N., Holland, H. J., Vermeer, C. H., & Ter Brake, H. J. M. (2015). Modeling the adsorption of mixed gases based on pure gas adsorption properties. IOP Conference Series: Materials Science and Engineering, 101(1). https://doi.org/10.1088/1757-899X/101/1/012169

[19] Uguina, M. A., Delgado, J. A., Águeda, V. I., & García-Sanz, A. (2008). Microwave synthesis of Sr-ETS-4 and evaluation of its molecular sieving properties in the nitrogen/methane separation. In Studies in Surface Science and Catalysis (Vol. 174, Issue SUPPL. PART A). Elsevier B.V. https://doi.org/10.1016/S0167-2991(08)80269-8

[20] Weh, R., Xiao, G., Islam, M. A., & May, E. F. (2020). Nitrogen Rejection by Dual Reflux Pressure Swing Adsorption Using Engelhard Titanosilicate Type 4. Industrial and Engineering Chemistry Research, 59(52), 22573–22581. https://doi.org/10.1021/acs.iecr.0c03768

[21] Xiao, G., Li, Z., Saleman, T. L., & May, E. F. (2017). Adsorption equilibria and kinetics of CH4 and N2 on commercial zeolites and carbons. Adsorption, 23(1), 131–147. https://doi.org/10.1007/s10450-016-9840-7

[22] Yoon, J. W., Chang, H., Lee, S. J., Hwang, Y. K., Hong, D. Y., Lee, S. K., Lee, J. S., Jang, S., Yoon, T. U., Kwac, K., Jung, Y., Pillai, R. S., Faucher, F., Vimont, A., Daturi, M., Férey, G., Serre, C., Maurin, G., Bae, Y. S., & Chang, J. S. (2017). Selective nitrogen capture by porous hybrid materials containing accessible transition metal ion sites. Nature Materials, 16(5), 526–531. https://doi.org/10.1038/nmat4825

Appendix D Aspen Adsorption configuration description

D1 Compressibility model

As gas flows through the pressure gradients in a packed bed, it changes volume. This volume change affects the gas velocity and temperature, which in turn influences the pressure drop. Therefore, it is crucial to select the correct thermodynamic model of the gas phase so that our calculations generate correct volumetric flow rates. Peng-Robinson model was the one considered for this case.

D2 Aspen Adsorption Flowsheet

The flowsheet is constituted by one Adsorbent bed (*Bed*), two Feed/inlet boundary terminators (*Feed and Purge*), three Product/outlet boundary terminators (*Product, Co* and *Waste*), two gas tank voids (*TD1* and *TD2*), five gas valves (*VF, VP, VCo, VWaste* and *VPurge*), and finally one Cycle Organizer.

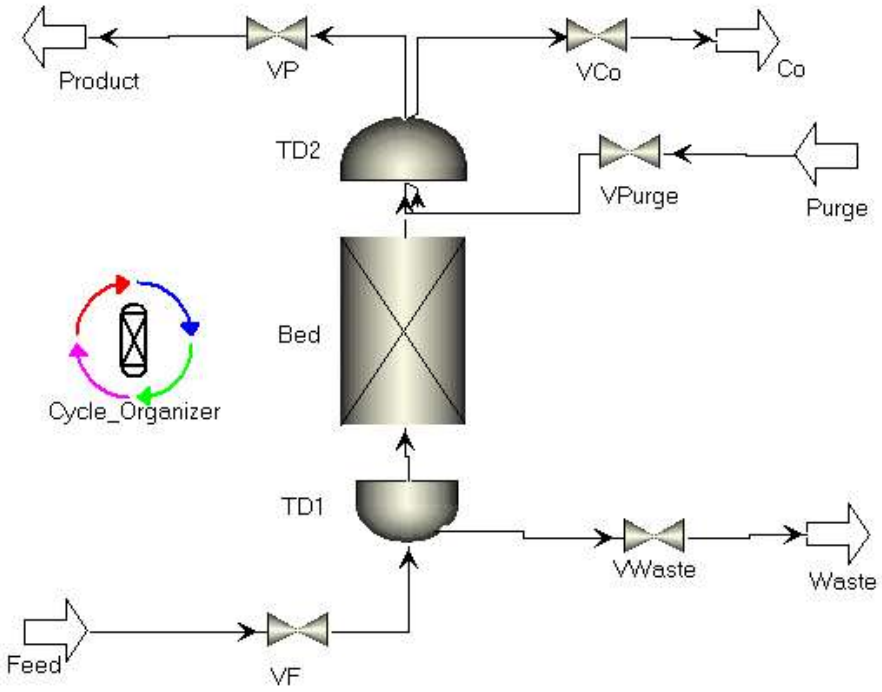

Figure AD 1 - Aspen Adsorption Flowsheet.

D3 Gas valves

The gas valve model simulates a simple linear valve. The valve active specification can present the following value options: 0 – the valve is closed; 1 – valve is fully opened; 2 valve's flow rate will have a linear relationship with pressure drop; 3 - valve with a fixed flow rate.

- **Valve CV calculation**

In *Aspen Adsorption*, valves operate under the assumption that the molar flow rate is linearly related to pressure drop across the valve:

$F = Cv \cdot \Delta P$

The first approximation to the valve *Cv* value should be made to approximate the PSA simulation to a real system, by the following equation:

$$Cv = \frac{100\,V}{R\,T\,\Delta t}\ln\left(\frac{P_{high}^{start} - P_{low}^{start}}{P_{high}^{end} - P_{low}^{end}}\right)$$

[1] Wood, K. R., Liu, Y. A., & Yu, Y. (2018). Design, Simulation and Optimization of Adsorptive and Chromatographic Separations. *Design, Simulation and Optimization of Adsorptive and Chromatographic Separations*. https://doi.org/10.1002/9783527815029

[2] Aspen Technology, Aspen Adsim 2004.1, Adsorption Reference Guide

Appendix E Aspen Adsorption Input

Isotherm Parameter (IP)

IP1 = $q_{sat} \cdot b_0$ (kmol kg^{-1} bar^{-1})

IP2 = $\frac{-(\Delta H)}{R}$ (K)

IP3 = b_0 (bar^{-1})

IP4 = $\frac{-(\Delta H)}{R}$ (K)

Axial mass dispersion (E_z)

Axial mass dispersion was calculated based on the Einstein statistical theory of diffusion - random walk model:

$$E_z = \frac{u_i d_p}{2}$$

where u_i is the interstitial velocity and d_p is the adsorbent particle diameter.

Thermal conductivity (K_g and K_s)

Gas

$$Pe_{ax,h} = \frac{u\, d_p}{\frac{K_g}{\rho_f\, C_{p_f}}} \sim 1 - 2$$

Solid

$$Pe_{ax,h} = \frac{u\, d_p}{\frac{K_s}{\rho_s\, C_{p_s}}} \sim 1 - 2$$

where u is the superficial velocity, ρ_f is the fluid density and C_{p_f} is the fluid specific heat capacity, ρ_s is the adsorbent density and C_{p_s} is the adsorbent specific heat capacity.

Heat transfer coefficient (HTC)

The adsorbent particles were considered of spheric shape. For the fixed bed case, heat transfer coefficient in the film can be calculated by:

$$Nu_{min} = 2 = \frac{HTC\, d_p}{K_g}$$

[1] *Slides Engenharia das Reacções III Reaction Engineering III Integrated Master in Chemical Engineering Department of Chemical Engineering Faculty of Engineering University of Porto 2020/21, Luis Miguel Madeira*

Appendix F Aspen Adsorption simulation description

The valve adjustment of the simulation performed designed run 25 is here clarified.

Table AF 1 - Gas valve organization for run 25.

	Press	**Ads**	**CoBD**	**CnBD**	**Purge**
	30s	60s	10s	30s	60s
VF	**VF.AS = 2**	**VF.AS = 3**	**VF.AS = 0**	**VF.AS = 0**	**VF.AS = 0**
	VF.CV = 1×10^{-2} kmol/s/bar	**VF.F = 1.12×10^{-3} kmol/s**	**0**	**0**	**0**
VP	**VP.AS = 0**	**VP.AS = 2**	**VP.AS = 0**	**VP.AS = 0**	**VP.AS = 0**
	0	**VP.CV = 1.5×10^{-4} kmol/s/bar**	**0**	**0**	**0**
VCo	**VCo.AS = 0**	**VCo.AS = 0**	**VCo.AS = 2**	**VCo.AS = 0**	**VCo.AS = 0**
	0	**0**	**VCo.CV = 6.57×10^{-3} kmol/s/bar**	**0**	**0**
VWaste	**VWaste.AS = 0**	**VWaste.AS = 0**	**VWaste.AS = 0**	**VWaste.AS = 2**	**VWaste.AS = 2**
	0	**0**	**0**	**VWaste.CV = 3×10^{-2} kmol/s/bar**	**VWaste.CV = 9.5×10^{-3} kmol/s/bar**
VPurge	**Vpurge.AS = 0**	**Vpurge.AS = 0**	**Vpurge.AS = 0**	**Vpurge.AS = 0**	**Vpurge.AS = 3**
	0	**0**	**0**	**0**	**Vpurge.F = 1.12×10^{-4} kmol/s**

This template was replicated for all the simulation runs, and more detailed description of the valve configuration and CV values can be found in the tables.

Table AF 3 - Purified Clinoptilolite simulation runs description.

Run	*u* (m s^{-1})	*L/D*	*P/F*	P_High (bar)	P_Co (bar)	P_Low (bar)	L (m)	VF.CV (Press)	VP.CV (Ads)	VCo.CV (CoBD)	VW.CV (CnBD)	VW.CV (Purge)	Purity	Recovery
2	0.07	2.86	0.1	5	1	0.5	2	3.00E-03	2.80E-04	6.57E-03	1.00E-04	9.50E-03	93.07 %	64.50 %
3	0.07	2.86	0.2	5	1	0.5	2	3.00E-03	2.80E-04	6.57E-03	1.00E-04	9.50E-03	93.84 %	59.65 %
4	0.07	2.86	0.3	5	1	0.5	2	3.00E-03	2.80E-04	6.57E-03	1.00E-04	9.50E-03	94.45 %	54.66 %
5	0.07	2.86	0.1	8	1	0.5	2	1.00E-02	1.42E-04	6.57E-03	1.00E-04	9.50E-03	92.59 %	66.64 %
6	0.07	2.86	0.1	3	1	0.5	2	1.00E-02	3.86E-04	6.57E-03	1.00E-04	9.50E-03	93.36 %	60.45 %
7	0.07	2.86	0.1	5	1	0.5	2	1.00E-02	2.80E-04	6.57E-03	1.00E-04	9.50E-03	93.00 %	65.03 %
8	0.11	5	0.1	5	1	0.5	2.9	1.00E-02	2.80E-04	6.57E-03	1.00E-04	9.50E-03	93.05 %	65.03 %
9	0.17	10	0.1	5	1	0.5	4.6	1.00E-02	2.80E-04	6.57E-03	1.00E-04	9.50E-03	94.35 %	65.90 %
10	0.07	2.86	0.1	5	3	0.5	2	1.00E-02	2.80E-04	3.80E-04	1.00E-04	9.50E-03	93.69 %	49.52 %
11	0.07	2.86	0.1	5	2	0.5	2	1.00E-02	2.80E-04	9.90E-04	1.00E-04	9.50E-03	93.45 %	57.02 %
13	0.07	2.86	0.1	5	1	0.1	2	1.00E-02	2.80E-04	6.57E-03	1.63E-03	9.50E-03	96.59 %	56.06 %
15	0.07	2.86	0.1	5	1	0.3	2	1.00E-02	2.80E-04	6.57E-03	1.63E-03	9.50E-03	94.36 %	60.98 %
14	0.07	2.86	0.1	5	1	0.1	2	5.00E-03	2.80E-04	6.57E-03	1.63E-03	9.50E-03	96.74 %	55.82 %
16	0.07	2.86	0.1	5	1	0.1	2	3.00E-03	2.80E-04	6.57E-03	1.63E-03	9.50E-03	96.64 %	57.02 %
17	0.07	5	0.1	5	1	0.1	3.5	3.00E-03	2.80E-04	6.57E-03	1.63E-03	9.50E-03	96.20 %	51.84 %
19	0.07	2.86	0.1	5	1	0.1	2	3.00E-03	1.00E-04	6.57E-03	1.63E-03	9.50E-03	96.68 %	50.84 %
20	0.07	2.86	0.1	5	1	0.1	2	3.00E-03	5.00E-04	6.57E-03	1.63E-03	9.50E-03	96.83 %	55.73 %
25	0.07	2.86	0.1	5	1	0.1	2	1.00E-02	1.50E-04	6.57E-03	3.00E-02	9.50E-03	96.66 %	58.34 %
51	0.07	2.86	0.1	8	1	0.1	2	1.00E-02	1.00E-04	6.57E-03	3.00E-02	9.50E-03	96.17 %	72.62 %

Table AF 4 - Mg-Clinoptilolite simulations runs description.

Run	*u* (m s^{-1})	*L/D*	*P/F*	P_High (bar)	P_Co (bar)	P_Low (bar)	L (m)	VF.CV (Press)	VP.CV (Ads)	VCo.CV (CoBD)	VW.CV (CnBD)	VW.CV (Purge)	Purity	Recovery
31	0.07	2.86	0.1	5	1	0.1	2	1.00E-02	1.50E-04	6.57E-03	3.00E-02	9.50E-03	**98.38 %**	**77.31 %**
32	0.07	2.86	0.1	5	1	0.1	2	1.00E-02	2.80E-04	6.57E-03	3.00E-02	9.50E-03	**98.38 %**	**75.97 %**
33	0.17	10	0.1	5	1	0.1	4.6	1.00E-02	2.80E-04	6.57E-03	3.00E-02	9.50E-03	**97.86 %**	**76.46 %**
34	0.11	5	0.1	5	1	0.1	2.9	1.00E-02	2.80E-04	6.57E-03	3.00E-02	9.50E-03	**98.57 %**	**66.11 %**
35	0.07	2.86	0.2	5	1	0.1	2	1.00E-02	2.50E-04	6.57E-03	3.00E-02	9.50E-03	**98.70 %**	**74.19 %**
36	0.07	2.86	0.3	5	1	0.1	2	1.00E-02	2.50E-04	6.57E-03	3.00E-02	9.50E-03	**98.81 %**	**66.29 %**
37	0.07	2.86	0.1	5	1	0.1	2	1.00E-02	2.50E-04	6.57E-03	3.00E-02	9.50E-03	**98.35 %**	**76.07 %**
38	0.07	2.86	0.1	5	1	0.1	2	3.00E-03	2.50E-04	6.57E-03	3.00E-02	9.50E-03	**98.57 %**	**75.14 %**
39	0.07	2.86	0.1	5	1	0.3	2	1.00E-02	2.50E-04	6.57E-03	3.00E-02	9.50E-03	**92.93 %**	**82.04 %**
40	0.07	2.86	0.1	5	1	0.5	2	1.00E-02	2.50E-04	6.57E-03	3.00E-02	9.50E-03	**93.09 %**	**87.40 %**
41	0.07	2.86	0.1	8	1	0.1	2	1.00E-02	1.42E-04	6.57E-03	3.00E-02	9.50E-03	**97.87 %**	**84.92 %**
42	0.07	2.86	0.1	3	1	0.1	2	1.00E-02	3.86E-04	6.57E-03	5.00E-04	9.50E-03	**98.03 %**	**71.11 %**
43	0.07	2.86	0.1	5	2	0.1	2	1.00E-02	2.50E-04	9.90E-04	5.00E-04	9.50E-03	**97.93 %**	**57.76 %**
44	0.07	2.86	0.1	5	3	0.1	2	1.00E-02	2.80E-04	3.80E-04	1.00E-04	9.50E-03	**98.30 %**	**48.13 %**
46	0.07	2.86	0.1	8	1	0.5	2	1.00E-02	1.42E-04	6.57E-03	5.00E-04	9.50E-03	**92.50 %**	**93.08 %**
49	0.07	2.86	0.1	5	1	0.1	2	1.00E-02	2.50E-04	6.57E-03	3.00E-02	9.50E-03	**98.28 %**	**76.07 %**
50	0.07	2.86	0.1	8	1	0.1	2	1.00E-02	1.42E-04	6.57E-03	3.00E-02	9.50E-03	**97.14 %**	**84.33 %**

Appendix G Results of Run 41

The simulation configuration is detailed in the following table.

Table AG 1 - Configuration of run 41.

RUN 41 – L/D = 2.86 - L = 2m – P/F = 0.1 – P_H = 8 bar - P_Co = 1 bar – P_Low = 0.1 bar				
Press	Ads	CoBD	CnBD	Purge
30s	60s	10s	30s	60s
VF.CV = 1E-2 kmol/s/bar	VF.F = 1.12E-3 kmol/s	VF=0	VF = 0	VF = 0
VP = 0	VP.CV = 1.42E-4 kmol/s/bar	VP = 0	VP = 0	VP = 0
Vco = 0	Vco = 0	Vco.CV = 6.57E-3 kmol/s/bar	Vco = 0	Vco = 0
Vwaste = 0	Vwaste = 0	Vwaste = 0	Vwaste.CV = 3E-2 kmol/s/bar	Vwaste.CV = 9.5E-3 kmol/s/bar
Vpurge = 0	Vpurge = 0	Vpurge = 0	Vpurge = 0	Vpurge.F = 1.12E-4 kmol/s

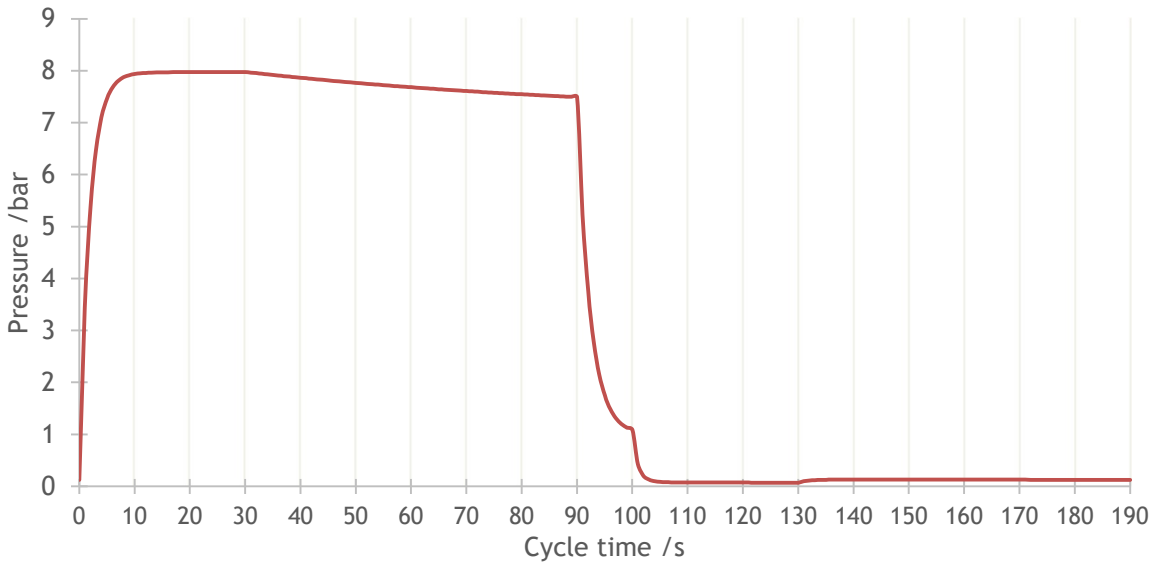

Figure AG 1 - Pressure history of run 41.

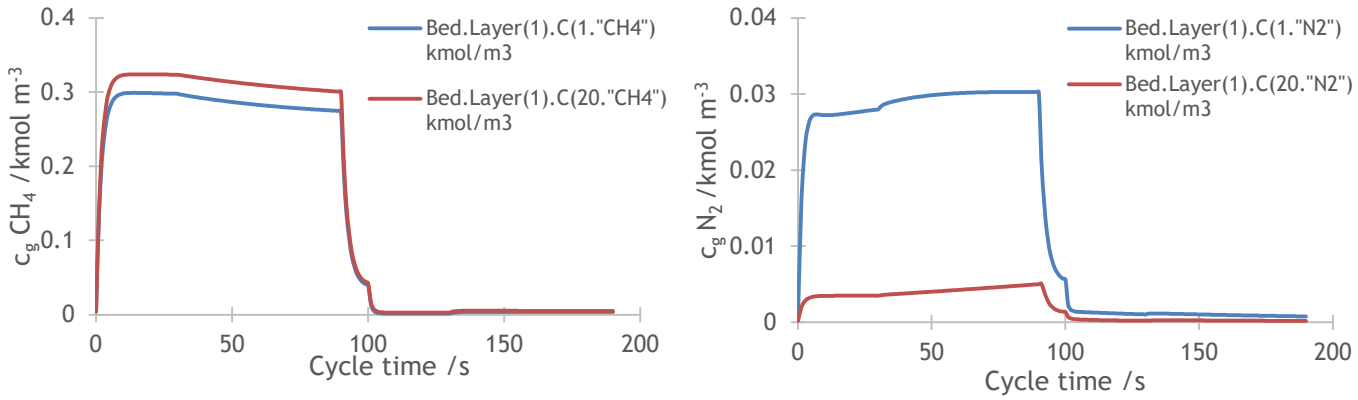

Figure AG 2 - Gas phase concentration.

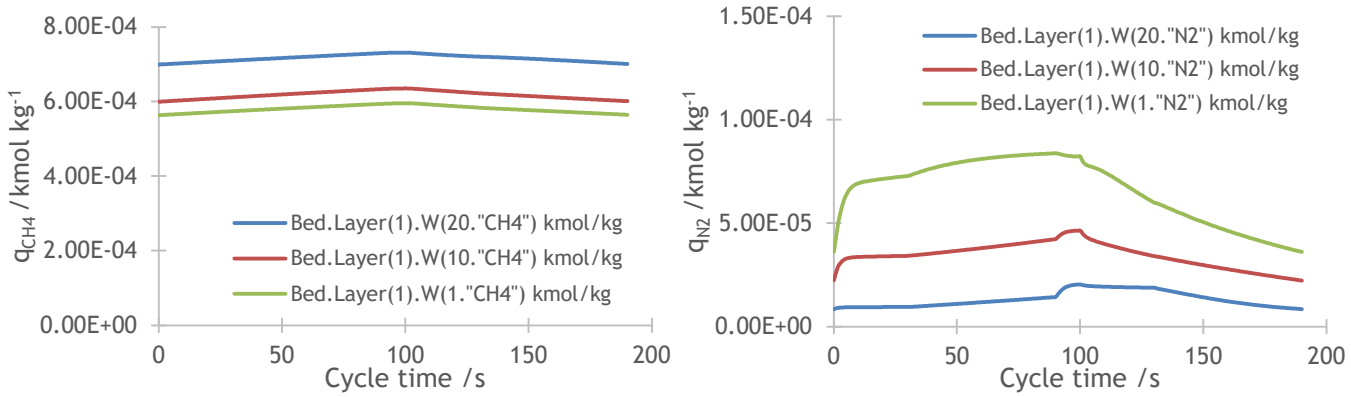

Figure AG 3 - Solid phase concentration.

Productivity and energy consumption in regeneration steps were also calculated, for a 2-bed PSA unit.

Table AG 2 - Performance indicators for Run 41.

Run	Purity (%)	Recovery (%)	Productivity (mol_{CH4} kg_{ads}^{-1} h^{-1})	Energy (kJ mol_{CH4}^{-1})
41	97.87	84.92	5.76	58.31

Appendix H Material balance validation

Aspen Adsorption results were validated through a material balance validation of a cycle, for each component. All integration calculations done were based on the trapezoidal rule, directly applied to the data extracted from the programme.

$$\int_0^{t_{press}} F_{in_{press}} \cdot y_i \, dt + \int_0^{t_{ads}} F_{in_{ads}} \cdot y_i \, dt + \int_0^{t_{purge}} F_{in_{purge}} \cdot y_i \, dt$$

$$= \int_0^{t_{ads}} F_{out_{ads}} \cdot y_i \, dt + \int_0^{t_{co}} F_{out_{co}} \cdot y_i \, dt + \int_0^{t_{cn}} F_{out_{cn}} \cdot y_i \, dt + \int_0^{t_{purge}} F_{out_{purge}} \cdot y_i \, dt$$

A material balance validation was performed for the run 48, and the results can be checked below.

CH4		
Inlet		
Feed Press+ Ads	1.15E-01	kmol/s
Purge	1.09E-04	kmol/s
Outlet		
Co	4.89E-02	kmol/s
Cn (waste)	1.43E-02	kmol/s
Purge (waste)	1.17E-02	kmol/s
Error Material balance	**4%**	

N2		
Inlet		
Feed Press+ Ads	1.28E-02	kmol/s
Purge	3.36E-06	kmol/s
Outlet		
Co	1.21E-03	kmol/s
Cn (waste)	6.94E-03	kmol/s
Purge (waste)	3.71E-03	kmol/s
Error Material balance	**0.095%**	

The errors calculated might be associated with tank void accumulation during the cycle steps.